Search for Ultra-High Energy Photons from Centaurus A with the Pierre Auger Observatory

von

Lukas Middendorf

Masterarbeit in Physik

vorgelegt der
Fakultät für Mathematik, Informatik und Naturwissenschaften
der
Rheinisch-Westfälischen Technischen Hochschule Aachen

im Januar des Jahres 2012

angefertigt am

III. Physikalischen Institut A

Erstgutachter und Betreuer

Prof. Dr. Thomas Hebbeker
III. Physikalisches Institut A
RWTH Aachen

Zweitgutachter

Prof. Dr. Christopher Wiebusch
III. Physikalisches Institut B
RWTH Aachen

Contents

1. Introduction **7**

2. Cosmic rays **9**
2.1. Nature and Origin . . . 9
2.1.1. Energy spectrum . . . 9
2.1.2. Production mechanisms . . . 11
2.1.3. Source candidates . . . 11
2.1.4. Propagation . . . 14
2.1.5. Ultra-high energy photon production . . . 14
2.2. Cosmic ray induced air showers . . . 16
2.2.1. Detection principles . . . 18

3. The Pierre Auger Observatory **19**
3.1. The Surface Detector . . . 20
3.2. The Fluorescence Detector . . . 20
3.3. Enhancements . . . 22
3.4. Hybrid event reconstruction . . . 23
3.4.1. $\overline{\text{Off}}\underline{\text{line}}$ . . . 24

4. Photon induced air showers **25**
4.0.1. CORSIKA . . . 25
4.0.2. Simulation parameters . . . 26
4.1. Attributes of photon induced air showers . . . 27
4.1.1. Invisible energy . . . 31
4.2. Landau-Pomeranchuk-Migdal effect . . . 31
4.3. Preshower effect . . . 33
4.4. Current limits on photon flux and photon fraction at ultra-high energies . 35

5. Photon point source search **39**
5.1. Idea . . . 39
5.2. Used data set . . . 40
5.2.1. Stereo event handling . . . 41
5.2.2. Maximum angular error cut . . . 42
5.2.3. Used cuts . . . 44
5.3. Centaurus A as a photon source candidate . . . 45
5.4. Selection of signal region and background region . . . 45
5.4.1. Correlation between $X_{\max}$ and zenith angle . . . 46
5.4.2. Choice of declination . . . 48
5.4.3. Choice of right ascension . . . 49
5.5. Correction of the simulated zenith angle distribution . . . 52
5.6. Photon energy scale correction . . . 55
5.7. Photon candidate discrimination through $X_{\max}$-Cuts . . . 57
5.8. Kolmogorov-Smirnov test in energy bins . . . 59
5.9. Significance of counting experiments with uptime estimation . . . 62

5.9.1. Standard deviation of signal . . . 63
5.9.2. Likelihood ratio method . . . 64
5.9.3. Verification of the formulae . . . 66
5.10. Determination of the number of photon candidate events . . . 69
5.10.1. Significance . . . 69
5.11. Limits on the photon count at ultra-high energies from Centaurus A . . . 70
5.12. Limits on the photon fraction at ultra-high energies from Centaurus A . . 71
5.12.1. Correction for different detector acceptance . . . 72
5.13. Discussion of results . . . 75

6. Summary and Outlook **79**

Bibliography **81**

A. Steering cards **87**
A.1. CORSIKA steering cards . . . 87
A.2. ADST cut files . . . 88
A.2.1. fd.cuts . . . 88
A.2.2. sd.cuts . . . 89
A.3. Offline steering cards for simulation . . . 89
A.3.1. ModuleSequence.xml . . . 89
A.3.2. bootstrap.xml . . . 91

B. Miscellaneous **95**
B.1. Calculations . . . 95
B.1.1. Likelihood . . . 95
B.1.2. Statistical uncertainty of efficiency for weighted counts . . . 95
B.2. Comparison of simulations and data . . . 96
B.3. Coordinate systems . . . 102

1. Introduction

The earth is constantly hit by cosmic ray particles. This fact was first discovered in 1912 by Victor Hess. Since then, the knowledge about these particles has been broadened. When these particles with energies up to and above 10^{20} eV enter the atmosphere, they initiate cascades of high energetic particles moving towards the ground, called extensive air showers. These can be detected either by particles reaching the ground, or by fluorescence light which is emitted by nitrogen atoms because of the excitation by secondary particles of the air shower. The arrival direction, energy and particle type of the primary particle can be reconstructed. One of the experiments for the detection of extensive air showers with energies from 10^{18} eV up to the highest energies is the Pierre Auger Observatory in Argentina. It combines both detection methods.

So far, the exact source of the cosmic rays is unknown. However, there are some theories and models of particle acceleration in astrophysical sources. Also some theories predict exotic particles remaining from the big bang, which on decay might produce ultra-high energy cosmic rays. Charged particles are deflected by the galactic or extragalactic magnetic fields. Due to this, the directional information of the charged particles can not be used to identify their sources.

The cosmic rays also consist of photons. Up to energies of 10^{15} eV they are observed with Imaging Atmospheric Cherenkov Telescopes. Photons of higher energy have not been observed yet. There are already limits on the photon fraction (fraction of photons off all arriving cosmic rays) between some percents and some ten percents (depending on the energy) in the energy range observable by the Pierre Auger Observatory . The already published analyses do not take directional information into account. There is one directed photon search analysis, which gives limits on the photon fraction in different regions of the sky. These are in the order of 10 percent for most of the visible sky.

The analysis presented in this thesis aims to search for ultra-high energy photon point sources by using hybrid data from the Pierre Auger Observatory, or to set similar limits on their flux.

In chapter 2 a short overview over cosmic rays and extensive air showers is given. In chapter 3 the Pierre Auger Observatory is presented. In chapter 4 some important characteristics of photon induced air showers are discussed and demonstrated using air shower simulations. Also some existing limits on their flux are presented. Finally, in chapter 5 a method to search for ultra-high energy photon point sources is described and tested on the source candidate Centaurus A.

2. Cosmic rays

It was first discovered in 1912 by Victor Hess [1], that the earth is constantly hit by particles called cosmic rays (CR). Since then, the knowledge about these particles has been broadened. The kinetic energies of the particles stretch from a few MeV to at least $3 \cdot 10^{20}$ eV [2]. In this energy range, the flux spans more than 20 orders of magnitude. Like the spectrum also the composition is thoroughly studied. The charged cosmic rays mainly consist of charged nuclei, here the main part comprises protons and helium [3], and some electrons. The neutral part of the cosmic rays consists of photons, neutrinos and neutrons.

Because of the large differences in energy and flux between the particles, it is not possible to measure all particles with a single detector. At lowest energies, where the flux is high, satellite and balloon based detectors are used to measure the particles directly. At higher energies above 10^{15} eV the flux is too low to collect high enough statistics (or even measure single events) with direct measurements. Here larger detectors are used to observe cosmic ray induced air showers from the ground. Through this the effective detector area can be greatly increased, at the cost of only being able to indirectly determine the energy of the detected particle and losing information about the type of the particle.

2.1. Nature and Origin

2.1.1. Energy spectrum

The flux of cosmic rays spans from $\sim 10^3\,\mathrm{m^{-2}s^{-1}}$ at some GeV to $\sim 1\,\mathrm{km^{-2}}$ per century at 10^{20} eV.

The measured energy spectrum of cosmic rays generally follows a power law

$$\frac{\mathrm{d}N}{\mathrm{d}E} \propto E^{-\gamma} \quad . \tag{2.1}$$

However, the power law is not perfect, but broken into segments with slightly changing spectral indexes. The spectral index is approximately $\gamma = 2.7$ up to energies of $E \approx 4 \cdot 10^{15}$ eV. Beyond this point, called the "Knee", the spectral index is $\gamma \approx 3.2$. Another feature in the energy spectrum can be found at $E \approx 3 \cdot 10^{18}$ eV, called the "Ankle", where the spectral index drops to $\gamma \approx 2.7$ again. At energies above $\approx 5 \cdot 10^{19}$ eV the spectrum drops even more rapidly [4]. The spectrum is shown in figure 2.1, further information can be found in [5]. The "Knee" and "Ankle" can be explained by the transition from galactic to extragalactic cosmic rays, but also by propagation-effects or as features in single sources. The final drop off is prominently described by the GZK[1]-effect (see 2.1.4), but might also be caused by the sources of cosmic rays themselves.

[1] Greisen-Zatsepin-Kuzmin

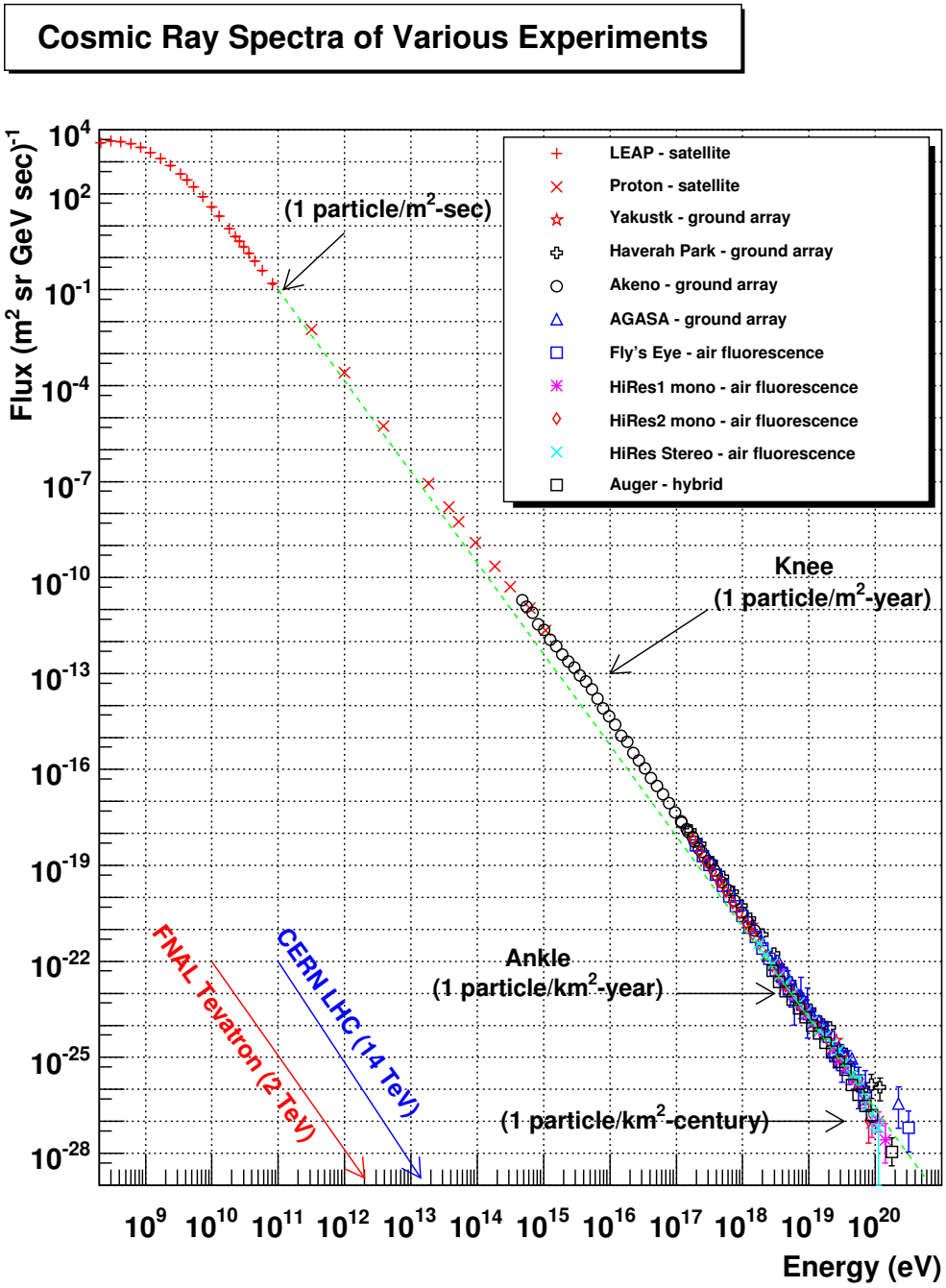

Figure 2.1.: Cosmic ray flux as measured by various experiments against the energy. The places in the spectrum where the spectral index changes (Knee and Ankle) are marked. A power law with a spectral index of ≈ 2.85 is shown in green to make the changes more visible. Original and references in [6].

2.1.2. Production mechanisms

The origin of the UHECRs[2] is still unknown. However, there are two main groups of theories explaining the creation of cosmic rays. The first one is through a decay of ultra-heavy exotic particles originating from the big bang. These models (called "top-down") generally predict a rather high photon flux and are more and more excluded by limits on the fraction of primary photons off all arriving cosmic rays [7]. The other possibility is to accelerate low energy particles ("bottom-up") to the observed energies.

The first proposed acceleration method is called Fermi acceleration, which is the scattering of particles in the magnetic field of moving interstellar clouds [8]. During a head-on "collision" with the cloud, the particle is accelerated with an energy gain

$$\delta E \propto \beta^2 \quad , \tag{2.2}$$

where β is the velocity of the molecular cloud. This "second order Fermi acceleration"[3] produces a power law energy spectrum. However, this acceleration has the problems of producing a much too high spectral index and subsequently of not being powerful enough to accelerate the particles sufficiently to explain the highest observed energies.

A more effective acceleration mechanism is the particle acceleration in astrophysical shock waves like in supernovae, called "shock acceleration". Here again the particles are scattered in turbulent magnetic fields. They gain energy in every pass through the shock wave [9]. Here the energy gain is

$$\delta E \propto \beta \quad , \tag{2.3}$$

where β is the velocity of the shock wave, which is the reason why it is called "first order Fermi acceleration". From this acceleration mechanism a power law energy spectrum with a spectral index $\gamma \approx 2$ follows [10], which is ideal to explain the observed energy spectrum.

However, not any source can accelerate particles up to and above $10^{20}\,\mathrm{eV}$. Acceleration is only possible until the magnetic fields are no longer strong enough to contain the particles. From this a maximum possible energy $E_{\max}$ can be estimated with the particle charge Z, the velocity β of the shock wave, the magnetic field strength B and the size L of the source region [11]:

$$\frac{E_{\max}}{10^{15}\,\mathrm{eV}} \approx \frac{1}{2} \cdot \beta \cdot Z \cdot \frac{B}{\mu\mathrm{G}} \cdot \frac{L}{\mathrm{pc}} \tag{2.4}$$

This can be visualized in the so called "Hillas plot" in figure 2.2. Size and magnetic field strength of possible cosmic ray particle accelerators are compared. Diagonal lines indicate constant $E_{\max}$.

2.1.3. Source candidates

Although no astrophysical objects have been identified up to now, there are various possible sources of UHECR, as can be seen in figure 2.2. Specific acceleration models for various astrophysical objects have been developed (see [12] for more details). The most promising are gamma ray bursts (GRB), active galactic nuclei (AGN), young magnetized neutron stars called pulsars, and the lobes of giant radio galaxies.

[2] ultra-high energy cosmic rays
[3] because of β^2

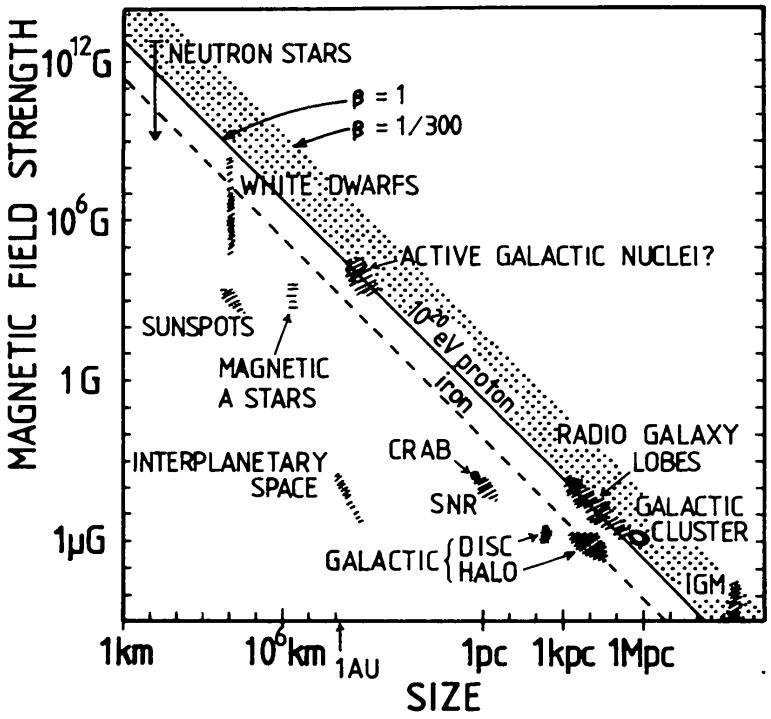

Figure 2.2.: The original "Hillas plot" from [11]. Size and magnetic field strength of possible cosmic ray particle accelerators are shown. Objects below the diagonal line can not accelerate protons to 10^{20} eV.

Centaurus A

The most prominent single source candidate on our sky is the radio galaxy Centaurus A (NGC 5128), which contains the nearest AGN with a distance[4] of 3-4 Mpc [13]. A supermassive black hole with a mass of $(5.5 \pm 3.0) \cdot 10^7$ sun masses is located in the center of the elliptical galaxy [14]. It is fed with matter from an accretion disk and produces two relativistic jets of particles perpendicular to the accretion disk. The relativistic jets are embedded in radio lobes. The jets and the inner radio lobes can be observed with X-rays and radio waves. An X-Ray image is shown in figure 2.3. The central structure with an angular size of about $20' \times 20'$ is embedded into faint giant radio lobes with a size of roughly $9° \times 4°$ ([15] and [16]). The giant radio lobes are nearly orientated in north-south-direction.

When the jets from the AGN interact with matter, first order Fermi acceleration can happen and accelerate particles to ultra-high energies. In some theories Centaurus A is proposed as the only extragalactic source for UHECR [18] because distance and propagation effects (section 2.1.4) prevent a significant flux from other extragalactic sources. By the H.E.S.S. experiment, γ rays with an energy up to 10^{13} eV have been measured from the core region of Centaurus A [19]. VHE[5] γ rays from the giant radio lobes have not yet been observed.

[4] due to absorption of light no exact distance measurement could be done
[5] Very High Energy: $E \lesssim 10^{15}$ eV

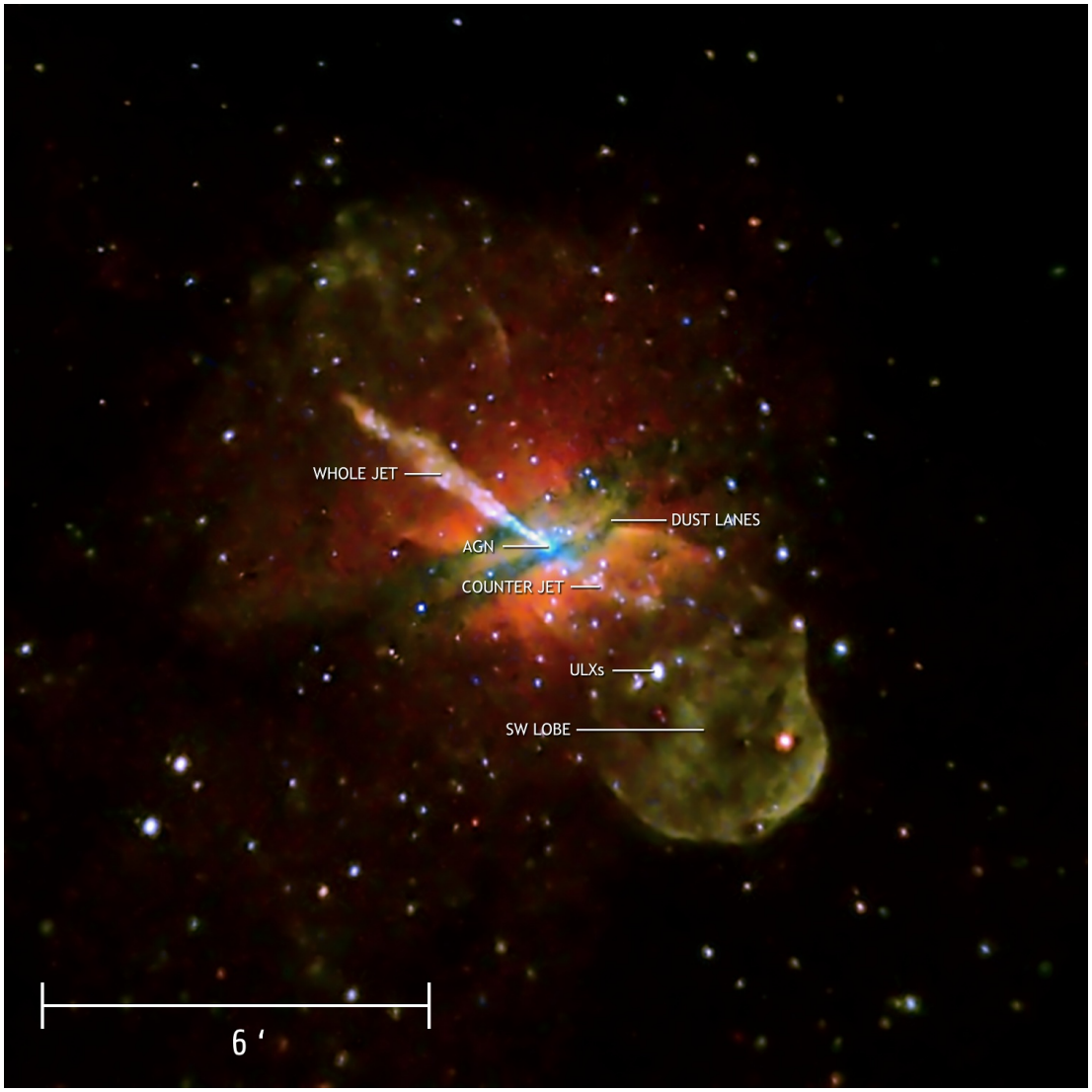

Figure 2.3.: Centaurus A as observed from Chandra with X-rays [17]. Marked are the central black hole as the active galactic nucleus (AGN), both *jets* originating from the AGN, *dust lanes* in the plane of the galaxy, one of the two bright inner radio *lobes* and an Ultraluminous X-ray source ($ULXs$) in the galaxy.

2.1.4. Propagation

While moving towards earth, the charged cosmic ray particles are deflected in the galactic and intergalactic magnetic fields. This deflection of a particle with charge Z and energy E in a magnetic field with strength B can be described with the Larmor radius (also called gyroradius) [5]:

$$r = 1.08\,\mathrm{pc} \cdot \frac{E/\mathrm{PeV}}{Z \cdot B/\mu\mathrm{G}} \tag{2.5}$$

Through this deflection in non-homogeneous magnetic fields, the directional information of the particles is lost. Even if there are very distinct sources of the cosmic rays, through the magnetic fields the flux on earth becomes nearly completely isotropic below some $10^{19}\,\mathrm{eV}$ [20]. To identify the sources of single cosmic rays, only the neutral particles photon, neutrino and neutron are usable.

Not only the directional information, but also the energy and type information of a particle can be lost on propagation. Unstable particles like neutrons can decay ($n \to p + e^- + \bar{\nu}_e$). Adiabatic energy loss occurs through the Hubble expansion. Also interactions with low energy background photons[6] can happen. For protons the pion production with $\sim 10^{-3}\,\mathrm{eV}$ photons of the cosmic microwave background ($T \approx 2.7\,\mathrm{K}$)

$$p + \gamma_{\mathrm{CMB}} \to \Delta^+(1232) \to n + \pi^+ \tag{2.6}$$

$$\to p + \pi^0 \tag{2.7}$$

is called the GZK[7] effect ([21] and [22]). A cutoff in the energy spectrum of UHECR is expected at the energies where the production of the $\Delta^+(1232)$ becomes possible. Even at energies below, direct e^+e^- pair production

$$p + \gamma_{\mathrm{CMB}} \to p + e^+ + e^- \tag{2.8}$$

can happen and leads to energy loss [23]. For a high energy photon γ the pair production with a low energy background photon γ_{B} can happen:

$$\gamma + \gamma_{\mathrm{B}} \to e^+ + e^- \tag{2.9}$$

Through this the photon is destroyed. The attenuation lengths resulting from these processes are shown in figure 2.4. For UHE photons above $10^{17.5}\,\mathrm{eV}$ it is in the order of $10\,\mathrm{Mpc}$.

The main energy loss effect for electrons is synchrotron radiation in magnetic fields.

2.1.5. Ultra-high energy photon production

The proposed main source of UHE photons is the decay of neutral pions ($\pi^0 \to \gamma + \gamma$) which have been produced in an initial process from hadronic particles at energies above $10^{18}\,\mathrm{eV}$. These pions can be produced in the GZK-process [25], which leads to a diffuse photon flux. The energies of the resulting "GZK photons" are roughly a factor of ~ 10 below the nucleon energy [24]. An other possible source of pions is the galactic center, where interactions of UHE protons not only with the cosmic microwave background but also with star light becomes possible [26]. Centaurus A as the most prominent source candidate for ultra-high energy cosmic rays is also a likely source for UHE photons [27].

[6] star light or cosmic microwave background (CMB)
[7] Greisen-Zatsepin-Kuzmin

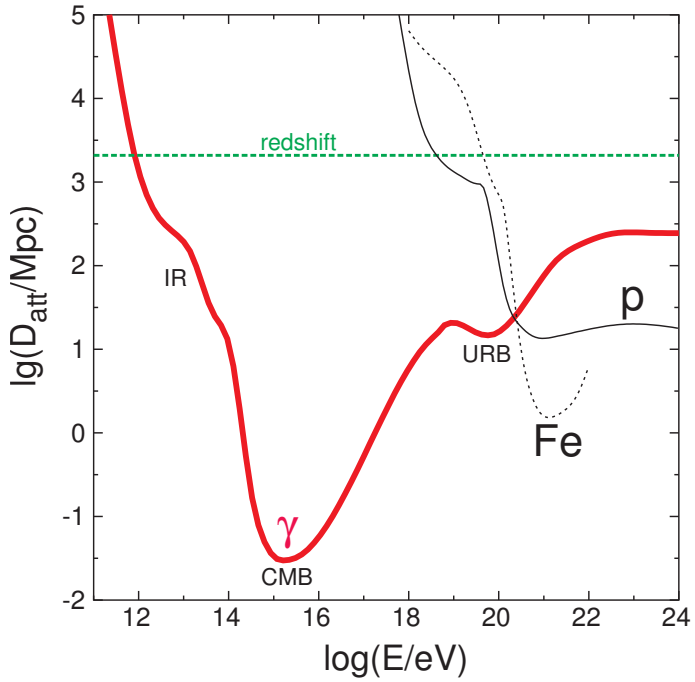

Figure 2.4.: Attenuation length for photons (thick line) at various energies due to interaction with infra red (IR), cosmic microwave background (CMB) and universal radio background (URB) photons. Attenuation length for protons (thin line) and iron (dotted line) is given as comparison. The dashed line ("redshift") corresponds to the adiabatic energy loss due to Hubble expansion. Original and references can be found in [24].

Most exotic heavy particles from top-down models of cosmic ray production also produce UHE photons when they decay.

A more detailed view can be found in [28].

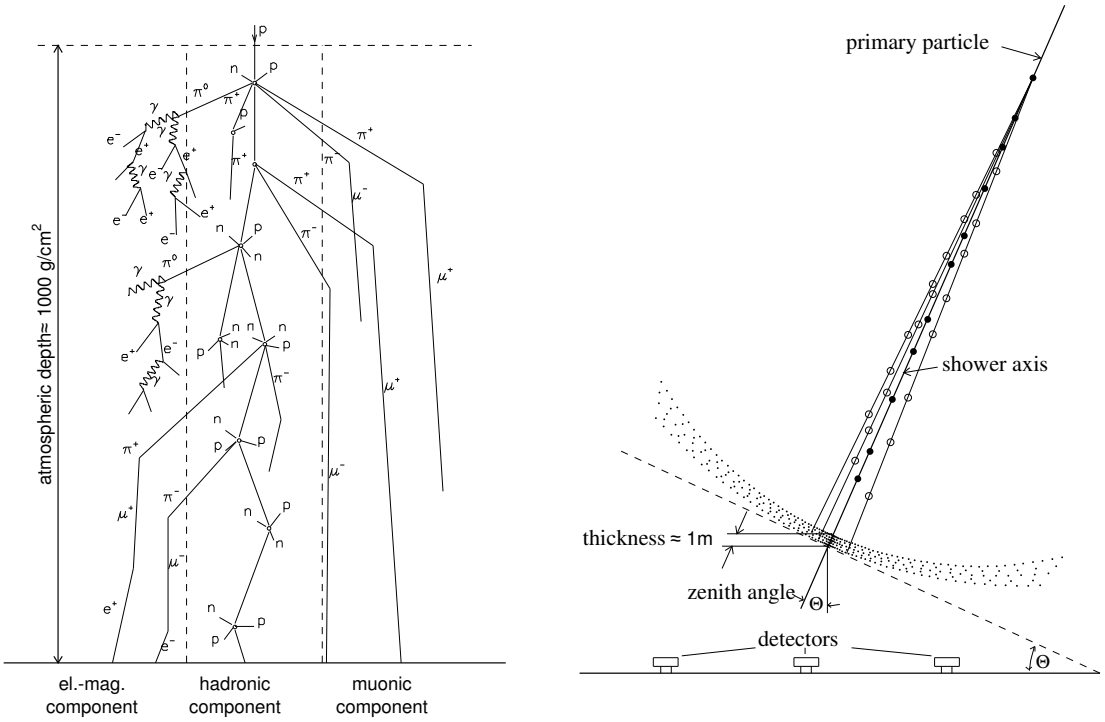

Figure 2.5.: Left: The different components of an extensive air shower in schematic view. The different components are not spatially separated in the real air shower.
Right: Sketch of the geometry of an extensive air shower (not to scale). Original in [30].

2.2. Cosmic ray induced air showers

In 1938 the existence of cosmic ray induced extensive air showers was discovered by Pierre Auger [29]. The primary particles of cosmic rays interact with the atmosphere. These first interactions mostly occur at a height of 20-30 km. The exact height depends on energy and type of the primary particle, but undergoes statistical fluctuations. These interactions mostly happen with nuclei of nitrogen or oxygen. The secondary particles being produced in this interaction undergo further interactions with the nuclei of the air. In the course of the further interactions, a cascade called extensive air shower (EAS) is formed. The particles move forwards on a slightly curved disk with a thickness in the order of a few meters (see figure 2.5). The lateral extension on the ground can reach a few kilometers. The exact dimensions depend on the type of the primary particle and its energy. Different primary particles and energies can be distinguished through the form of the longitudinal profile, the form of the lateral profile, the thickness of the shower front or the curvature radius of the shower front.

The longitudinal development of EAS is measured in slant depth X, which is an integral over the traversed air density and is measured in units of $\mathrm{g\,cm^{-2}}$:

$$X(x) = \int_{\infty}^{x} \rho(x')\,\mathrm{d}x' \tag{2.10}$$

with the height x and the air density ρ.

A shower can be divided into different components (see figure 2.5). The three main components are hadronic, electromagnetic (e^-, e^+ and γ) and muonic. Neutrinos can

be seen as a fourth component.

Hadronic component

Inelastic scattering with an atmospheric nucleus produces a multitude of hadronic secondary particles. The resulting hadronic cascade is normally initiated by a hadronic primary, but can also be generated by a photonuclear interaction of a photon primary. Photonuclear interactions of photons from the electromagnetic component also contribute to the hadronic component (demonstrated in section 4.1). The major part of the hadronic particles consists of pions, kaons, protons and neutrons which can further interact with the air, or decay. The products of a decay can contribute to the other components.

The longitudinal development of the number of secondary particles in the shower can be parametrized by the Gaisser-Hillas-Formula [31]:

$$N(X) = N_{\max}\left(\frac{X - X_1}{X_{\max} - X_1}\right)^{\frac{X_{\max}-X_1}{\lambda}} \exp\left(-\frac{X - X_1}{\lambda}\right) \tag{2.11}$$

Here $N_{\max}$ is the maximum number of secondary particles, $X_{\max}$ is the slant depth of the shower maximum, X_1 is the slant depth of the first interaction and λ is the effective mean free path between consequent hadronic interactions of the secondary particles in air (measured as a slant depth).

Electromagnetic component

The electromagnetic component consists of photons, electrons and positrons. Photons can be produced by the decay of neutral pions from the hadronic component. This is done over the whole development of the hadronic shower. Primary photons, electrons or positrons can also directly initiate an electromagnetic shower without a significant hadronic component. To a much lower extent also the decay of muons to electrons can contribute to the electromagnetic component. The main processes in an electromagnetic shower are e^+e^- pair production by photons and bremsstrahlung by electrons or positrons. The electromagnetic component is also responsible for the production of fluorescence light of excited nitrogen molecules in the air [32].

Muonic component

Muons are produced by the decay of the charged mesons $K^\pm$ and $\pi^\pm$ (together with the corresponding neutrinos) in the hadronic component. Due to their limited interactions and scattering in the atmosphere, muons often outlive the hadronic and electromagnetic components and their trajectories often point back to their place of production in the atmosphere. So they carry information about the very first interactions in the shower down to the ground. For photon primaries, with their reduced hadronic component, the amount of muons in the shower is significantly reduced compared to hadronic primaries. This can be used for the identification of primary photons with surface detectors. The muonic component is mostly "invisible" as it does not contribute significantly to the production of fluorescence light.

Neutrino component

Neutrinos are produced in EAS whenever muons are produced or decay. They withdraw energy from the active shower and are invisible to air shower measurements. This fact has to be corrected for.

2.2.1. Detection principles

There are various methods to detect extensive air showers. These methods can be divided into measurements of the longitudinal development of the shower and measurements of the lateral distribution of shower particles.

Particle detection at ground level

Measurements of the particles reaching the ground, using an array of detector stations, is a method to measure the lateral distribution of the shower particles. The main contribution here is through muons, which can easily reach the ground at high energies. The detector stations can be implemented using scintillators or Cherenkov radiators. Both kinds detect the light produced by crossing particles. The arrival direction and energy of the primary cosmic ray particle can be reconstructed through a measurement of the produced amount of light and the timing of the signal in different detector stations. Other parameters, like the radius of curvature of the shower front or the particle content, can be derived and used for primary particle identification.

Fluorescence light detection

The second important approach to gain information about EAS is to measure fluorescence light. It is radiated isotropically in the UV range of the light spectrum by excited nitrogen molecules. With so called "fluorescence telescopes" the longitudinal shower profile is measured. From this calorimetric measurement of the deposited energy, the energy of the primary particle can be estimated. When looking directly into the shower along the shower axis, also a significant amount of Cherenkov radiation from the electromagnetic component can be observed. Through the additional light, showers initiated by much lower energy particles can be observed compared to fluorescence light alone. This is used for IACTs[8] to measure VHE γ rays.

Other techniques

Also other types of electromagnetic waves are emitted by an EAS, like radio waves or microwaves. These can be measured from the ground to gain insight into the shower development, too. With underground neutrino detectors a part of the neutrino component of EAS or primary neutrinos directly can be measured.

[8]Imaging Air Cherenkov Telescope

3. The Pierre Auger Observatory

The Pierre Auger Observatory is an experiment to measure ultra-high energy cosmic ray induced extensive air showers. It is located near Malargüe in the province of Mendoza in Argentina. The detector is sensitive to showers initiated by particles with energies between 10^{18} eV and 10^{21} eV.

The experiment follows a hybrid design. It consists of two complementary detector parts to simultaneously measure the longitudinal and lateral shower profiles. Through this the systematic and statistical uncertainties on air shower analyses can be significantly reduced compared to measurements with only a single detector type. The lateral profile of the particles arriving at ground level is measured through 1600 Surface Detector (SD) stations, which are located on a grid with 1.5 km spacing, filling an area of roughly 3000 km^2. The longitudinal shower profile is detected by four fluorescence telescope buildings overlooking the detector array, which constitute the Fluorescence Detector (FD). Some additional detector enhancements are located in the area, too. The whole complex is shown in figure 3.1.

Through the hybrid design, advantages of both detection principles — the higher duty cycle of SD and the lower systematic energy uncertainty of FD — can be combined through cross calibration with EAS observed by both detector parts[1]. With a shower reconstruction which uses information from both detector types a lower uncertainty on the energy measurement can be reached.

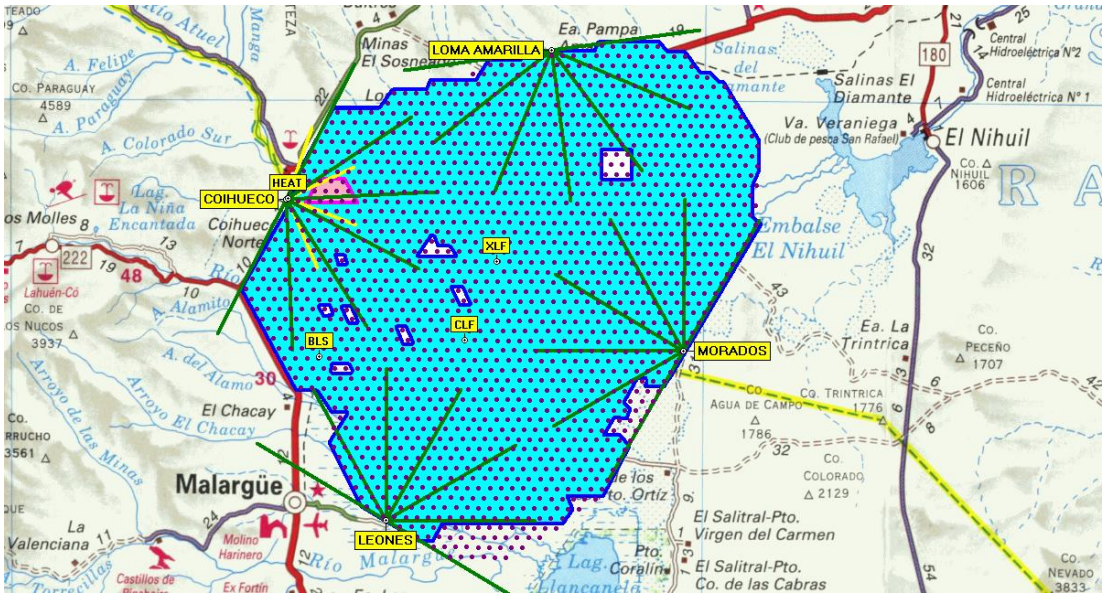

Figure 3.1.: The southern site of the Pierre Auger Observatory as of 2009 [33]. SD stations are shown as purple dots (the shaded area is deployed), the fields of view of the fluorescence telescopes are shown as green and yellow lines.

[1] called "golden hybrid" events

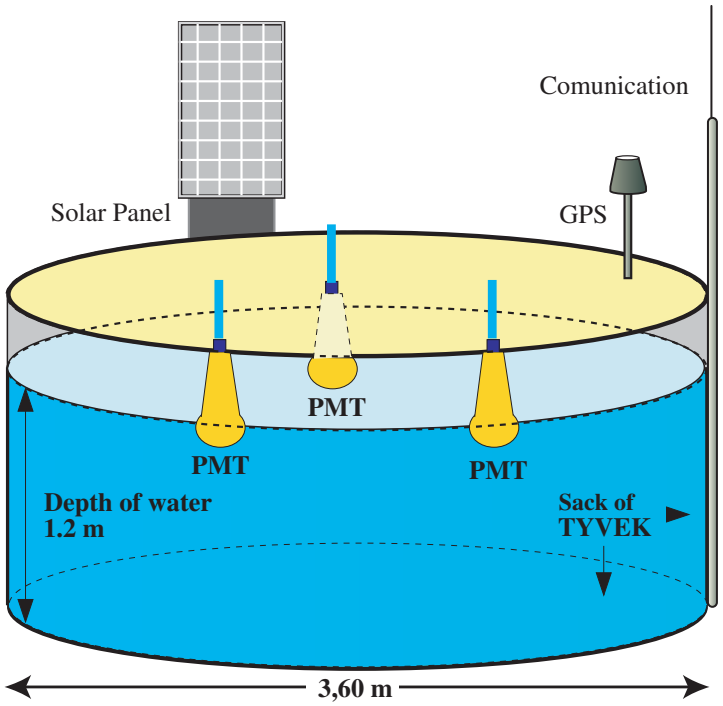

Figure 3.2.: Scheme of an SD station [34]. The station is filled with 10 tons of pure water as a Cherenkov radiator and has three PMTs to detect the produced light. Power is generated by a solar panel and stored in a battery for night-time operation. A GPS module is used to obtain exact time information.

3.1. The Surface Detector

The surface detector consists of over 1600 water-Cherenkov stations (see figure 3.2). They are located on a triangular grid with 1.5 km spacing, filling an area of roughly 3000 km^2. Particles from EAS arriving at the ground (mainly muons) are detected. The lateral profile of the EAS as well as the exact times of the arrival of the shower front at different stations can be measured. Through this the place where the shower core hits earth as well as the arrival direction can be calculated. Through the lateral particle distribution an estimator for the energy of the primary particle can be obtained.

3.2. The Fluorescence Detector

The fluorescence detector of the Pierre Auger Observatory [35] consists of 24 Schmidt cameras located in 4 telescope buildings[2] (see figure 3.3). Each telescope consists of a segmented 10 square meter mirror with a camera consisting of 440 PMTs in its focal point. To enter the telescope building, the light has to cross a UV-passing filter[3] and a corrector ring as an approximation of a Schmidt plate. The schematic of one telescope bay can be seen in figure 3.4. Each telescope has a field of view (FoV) of $30° \times 30°$ in azimuth and altitude. Each telescope site, consisting of six telescopes, has a FoV of 180° in azimuth. All sites together overlook the complete SD array and cover the complete azimuthal range. The fluorescence detector measures the fluorescence light, which is emitted during the shower cascade. Because the fluorescence light is proportional to

[2]Los Leones, Los Morados, Loma Amarilla and Coihueco
[3]Nitrogen fluorescence light can mostly pass, but background light is reduced.

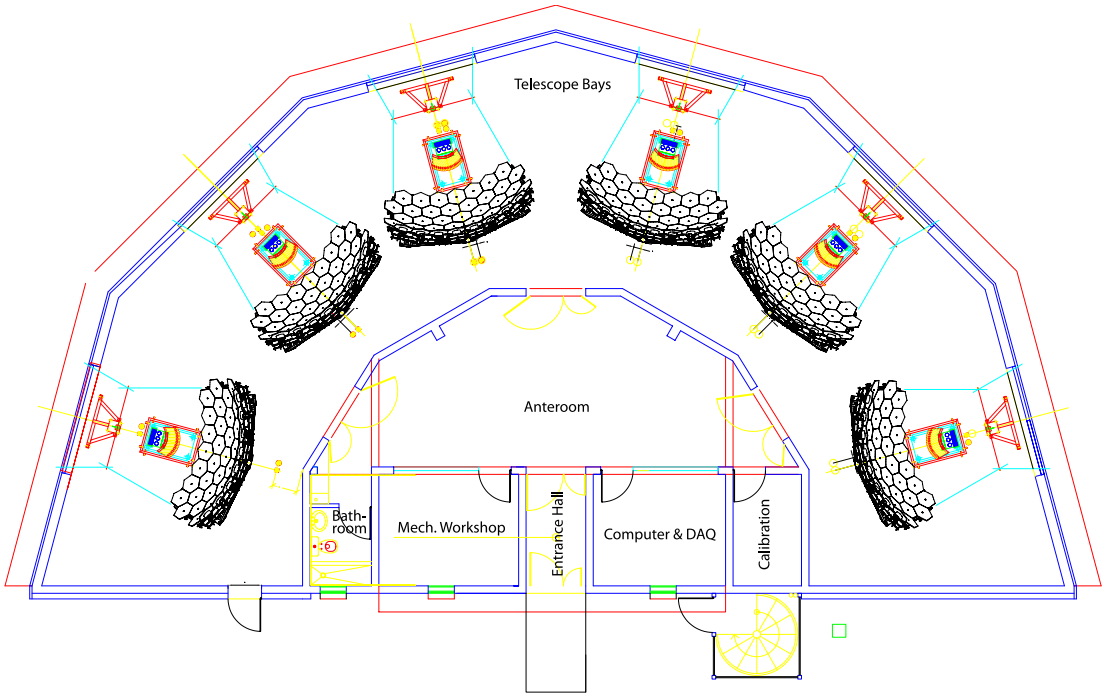

Figure 3.3.: Schematic of one building of the fluorescence detector [35]. Six fluorescence telescopes are placed around some auxiliary rooms.

the number of particles and the length of their tracks, the number of particles in every visible stage of the shower can be measured. To give a rough number, about 4 photons are produced per electron per meter [36]. In contrast to the SD, which can measure non-stop, the FD can measure only during clear and moonless nights, which leads to a significantly reduced duty cycle of about 10–15 %.

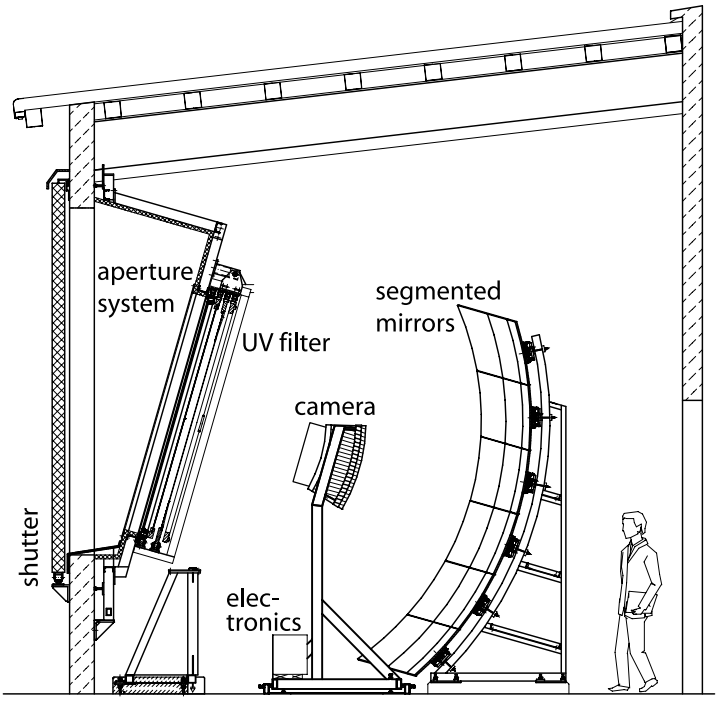

Figure 3.4.: Schematic view of one fluorescence telescope bay [35]. Fluorescence light enters through the shutter and aperture (here also the corrector ring is located) and is projected onto the camera by the segmented mirror. Human for size comparison.

3.3. Enhancements

In addition to the two main detector types, FD and SD, used at Auger Observatory, there are three additional detector components which have been installed in the last few years.

HEAT ("High-Elevation Auger Telescopes") [37] consists of three additional telescopes near the Coihueco telescope site. These telescopes are tiltable 30° upwards and extend the Coihueco field of view up to 60° in elevation. This allows to observe showers at lower energies down to 10^{17} eV. Generally, these have an $X_{\max}$ above the standard FD field of view.

AMIGA ("Auger Muons and Infill for the Ground Array") [38] is a second enhancement. One part of it is the infill, which consists of 61 additional SD stations between the original stations to reduce the grid spacing to 750 m in one part of the array. It is planned to add 24 additional stations to form a 433 m grid. The infill is supposed to reduce the lowest possible energy which is detectable with the surface detector to 10^{17} eV. The second part of AMIGA consists of scintillator muon detectors, which are buried near existing SD stations. Here the pure muon signal at the SD stations is measured, because of the shielding provided by the earth, which only muons can pass. These muon detectors are a new component for the overall hybrid design of the observatory and can bring a new understanding of extensive air showers.

AERA ("Auger Engineering Radio Array") [39] is the third enhancement of the Pierre Auger Observatory. It currently consists of 21 radio-detection stations, 160 stations on 20 km^2 are planed. AERA will be used to study the mechanisms responsible for radio emission in the VHF band (10-100 MHz) of extensive air showers.

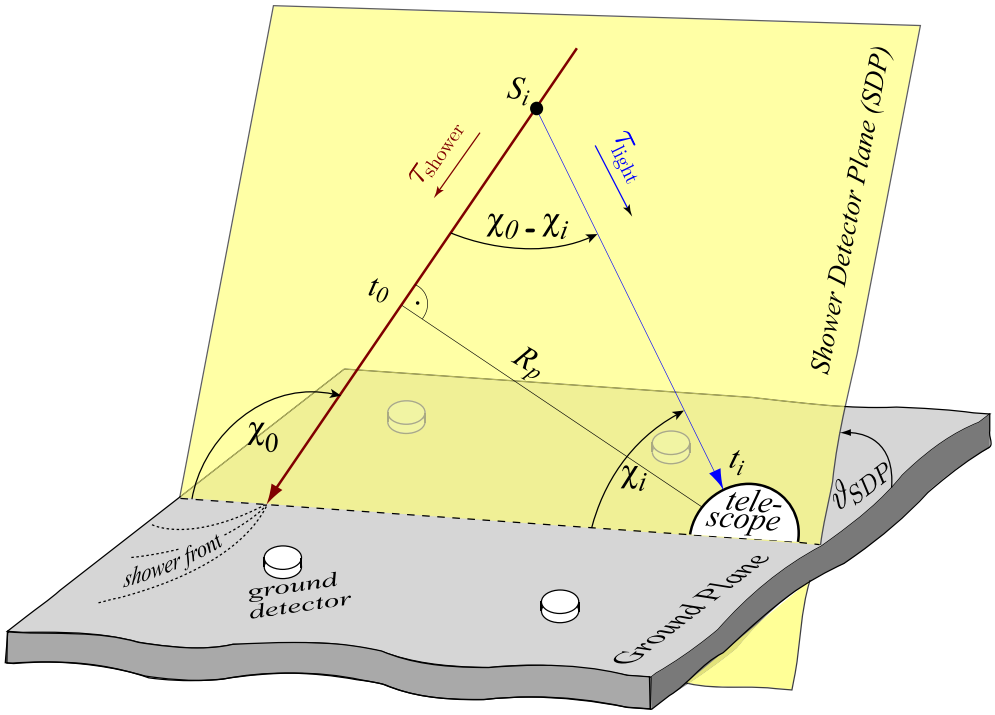

Figure 3.5.: Sketch of the shower geometry used in reconstruction [43]. The shower particles move along the shower axis with speed of light and emit fluorescence light in the course. With the trace of the observed light on the detector, the Shower Detector Plane can be determined. With the arrival times t_i of the light emitted at different places S_i on the shower axis together with their viewing angles χ_i, a time fit can be done to determine the still unknown quantities χ_0 and R_p.

There are additional test setups of various attempts to detect EAS with microwave radiation [40], which would add yet another complementary detection principle to the hybrid design.

3.4. Hybrid event reconstruction

To be used for physics analysis, event reconstruction has to be run on the raw data, which consists mainly of ADC[4] traces and timing information. Here estimators for physically useful quantities — like energy of the primary particle, arrival direction or $X_{\max}$ — are determined. In general, the event reconstruction can be separately achieved for the surface detector and fluorescence detector. However, the FD reconstruction ("mono") is often replaced by a "hybrid reconstruction", for which mainly FD data is used. Additionally, the time of impact on the ground and the location of the shower core from SD data is used. Through this the uncertainties on the event reconstruction can be dramatically reduced [41]. The resolution of the arrival direction is about 0.5°–1°, the energy resolution is in the order of 10 % and the $X_{\max}$ resolution is about $20\,\mathrm{g\,cm^{-2}}$ [42]. In the standard reconstruction, "Stereo events" observed by more than one telescope site are reconstructed separately for every site. The observed quantities have to be combined by later analyses.

[4] analog to digital converter

In the hybrid reconstruction the Shower Detector Plane (SDP) is determined first. This is the plane that contains both the shower axis and the FD site observing the shower (see figure 3.5). Afterwards the positioning of the shower axis in the SDP has to be determined. With the position of the shower core on the ground given by the SD data, mainly the angle χ_0 of the shower axis in the SDP is calculated. The active region of the shower S_i travels with the speed of light. Fluorescence light from the active region also travels towards the telescope with the speed of light and arrives there at the time t_i. Together with the angle χ_i corresponding to every pixel in the camera, the most likely values for χ_0 and R_p can be determined in a timing fit by a χ^2 minimization. These geometrical quantities can be converted to more convenient coordinates like azimuth and zenith of the arrival direction. For more details see [43].

After the geometry is fixed, an energy deposit profile as a function of the slant depth X is calculated from the observed fluorescence light, taking atmospheric effects (absorption and scattering) into account. Also the amount of detected Cherenkov radiation is determined and corrected for. To this profile a Gaisser-Hillas-Function (equation 2.11) is fitted, which yields the primary energy and the shower maximum $X_{\max}$. To derive $X_{\max}$ and E within reasonable uncertainties, the shower maximum $X_{\max}$ has to be observed, that means it has to lie in the field of view. For very close or very low energy showers it might be above the FoV, for showers with very high $X_{\max}$ it might be below the ground level and therefore generally unobservable.

In the energy determination a correction for invisible energy from neutrinos and muons ([44], [45]) is applied. This invisible energy correction depends on the type of primary, because of different fractions of muons and neutrinos for different primaries. Therefore, a systematic uncertainty for other types of primaries is introduced.

3.4.1. $\overline{\text{Off}}\underline{\text{line}}$

The $\overline{\text{Off}}\underline{\text{line}}$ toolkit [46] is the standard software for detector simulation and data reconstruction of the Pierre Auger Observatory. The above mentioned hybrid reconstruction, as well as SD reconstruction is implemented here. Also input files from different simulation tools for extensive air showers can be read and the production of fluorescence light as well as the detector response can be simulated. Data from the detector simulations can be reconstructed like real data for cross checking. Reconstructed data is often provided in the form of ADSTs[5].

[5] Advanced Data Summary Tree

4. Photon induced air showers

There are some characteristic differences between photon induced air showers and those induced by hadronic primaries. The most visible is a generally higher slant depth of the shower maximum $X_{\max}$ for photon induced showers. There are some specific effects which influence the development of photon induced air showers but not hadron induced air showers. These effects are the preshower effect (section 4.3) and the LPM[1] effect (section 4.2).

The preshower effect is also called geomagnetic cascading and is the e^+e^- pair production in the magnetic field of the earth above the atmosphere. It is direction dependent and becomes significant at photon energies above roughly 40 MeV. After multiple photons are produced in bremsstrahlung processes of the charged particles, a multitude of lower energetic particles (the highest energies are mostly in the order of a few EeV) enters the atmosphere and the resulting air shower is therefore a superposition of multiple lower energy showers.

The LPM effect reduces the cross section of e^+e^- pair production for photons in the coulomb field of nuclei. The interactions at multiple nuclei interfere destructively, which leads to a reduction of the cross section. The suppression increases with air density and photon energy. It leads to observable effects in photon induced air showers at energies of above 10^{18} eV. Through the LPM effect, the fluctuations of the shower profile in single showers and also between different showers are increased.

The differences and effects for photon induced air showers are shown in this chapter in more detail. Air shower simulations with CORSIKA for the Auger detector site (without detector simulation) are used for this. Photons and protons are used as primary particles for the simulations.

4.0.1. CORSIKA

CORSIKA [47] is a software tool to simulate the development of extensive air showers. It uses Monte-Carlo methods[2] to simulate single interactions and tracks the various particles in the developing shower through the atmosphere. Different models for hadronic interactions can be used. CORSIKA outputs the numbers and energies of different particle types throughout the longitudinal development and the lateral distribution of particles at ground level. Also a Gaisser-Hillas function is fitted to the longitudinal output from which the vertical depth of the shower maximum can be obtained. By dividing a vertical depth by the cosine of the zenith angle of the shower axis, the corresponding slant depth can be calculated[3].

To reduce the computation time and disk space usage, a technique named "thinning" [49]

[1] Landau-Pomeranchuk-Migdal

[2] Pseudo-random numbers are used to determine the outcome of interactions according to their probabilities.

[3] as long as the atmosphere can be approximated as being flat, which is possible for zenith angles up to 70° [48]

is used. Below a certain energy threshold only a part of the secondary particles are taken as representative and tracked further. These particles are given a higher weight. In this way fluctuations in the shower are artificially increased, but otherwise it would not be possible to simulate showers at energies above 10^{16} eV.

All studies in this chapter are done using showers simulated with a modified CORSIKA version 6.970. While doing the photon studies, some problems with CORSIKA had to be solved and in the course of that some modifications to CORSIKA were introduced.

The first problem to solve was the fact that the height of the first interaction was not written to the output file for photon induced showers with the PRESHOWER option enabled. In the case that no preshower actually happens, the photon should be handled as if the preshower option was not present[4]. This problem was solved by Dieter Heck[5] and the change is also included in CORSIKA versions 6.980 and higher.

A second problem was that in some photon induced showers the photon just disappeared in the first interaction with all energy being deposited in the atmosphere. This was identified by Dieter Heck as a programming error. All backwards flying particles in CORSIKA are supposed to no longer be tracked but counted as energy deposit. This test was erroneously inverted for ω-mesons so that all forwards flying particles were discarded. This was especially noticeable when an ω-meson was produced in the first interaction. The error was fixed by D. Heck for my simulations and will also be fixed in future CORSIKA versions after 6.990.

A third modification to the CORSIKA code was introduced by myself. The height of the first interaction given by CORSIKA does normally not take the LPM effect (see section 4.2) into account. It is not trivial to change CORSIKA to do it right, because at the time the correct height of the first interaction is known, the header of the output file, which should contain the height of the first interaction, is already written and can no longer be modified. So instead the height of the first interaction is written to a special data field at the end of the shower output, just for this analysis.

A last problem was that some showers ($\approx 0.5\,\%$) did never finish simulation. All simulations either finished within 8 hours (typically 1-4 hours) or not at all within one week. This was reproducible using the same seeds for the random number generators. It was not limited to either photons or protons alone and also did not seem to strongly depend on the energy of the primary particle. Only the QGSJET-II interaction model was tested. This bug was identified by Dieter Heck to happen at the production of very low energetic muons at the end of a shower cascade. Because of this, the missing showers should not impose a bias on any observable distribution [50]. Therefore, the bug fix mainly makes running the simulations more reliable and convenient. The small number of not finished showers is ignored for this analysis. This bug is solved in CORSIKA versions 6.981 and later, but was identified only after the simulations used in this chapter were already done.

4.0.2. Simulation parameters

The simulations are done using QGSJET-II-03 ([51] and [52]) and FLUKA 2008.3d ([53], [54]) as hadronic interaction models and EGS4 ([55]) as electromagnetic interaction model. All showers with photons as primary particle are simulated with the PRESHOWER option enabled. All events are simulated with a continuous energy (E)

[4] at least with regard to the height of the first interaction

[5] `http://www-ik.fzk.de/~heck`

distribution with a spectral index of $\gamma = 1$. That means a constant number of events is located in every energy bin with bin borders equally spaced in logarithm of the energy. The zenith angle θ is distributed as $\cos\theta \sin\theta$, which is correct for a flat detector. The thinning usually used for Auger simulations[6] is used, which means a thinning of 10^{-6} with an energy dependent maximum weight of $E \cdot 10^{-6}$ (evaluated at lower energy bin border). The geomagnetic field and height of the ground level are set to the values of the Pierre Auger Observatory[7]. For further simulation parameters see the steering card in appendix A.1.

The simulations are done for energies between $10^{17.5}\,\mathrm{eV}$ and $10^{20}\,\mathrm{eV}$ using photons and protons as primary particles. Energy bins with a width of 0.1 in $\log_{10} E$ are used. After applying all modifications to CORSIKA, there are approximately[8] 300 usable showers per energy bin and primary. The CORSIKA output is used directly. Because CORSIKA stops simulation at ground level (which corresponds to a vertical depth of $870\,\mathrm{g\,cm^{-2}}$ for the Auger detector site near Malargüe), the obtained value for the shower maximum $X_{\max}$ is only reliable up to the vertical depth of the ground level. At every step of the analysis where the shower maximum is important, only showers reaching their maximum before hitting the ground are used. This reduces the overall count of photons from 7482 to 5803 and the overall count of protons from 7486 to 7424. This means the cut almost only affects photon induced showers. A similar data cut is used on the FD data of the Pierre Auger Observatory and would be used on the reconstructed simulations if a detector simulation was done.

CORSIKA stores the height of the first interaction. What is physically meaningful is the atmospheric depth of it. The atmospheric depth can be calculated from the height using a parameterization [49, sec 2.4] for which the parameters are also stored in the CORSIKA output. COAST[9] is used to read the raw CORSIKA output files.

4.1. Attributes of photon induced air showers

The main observable used to identify photon induced air showers in the further analysis is the slant depth of the shower maximum $X_{\max}$. As can be seen in figure 4.1, photon induced air showers in general have a higher $X_{\max}$ than proton induced air showers. Both can be distinguished from each other on a statistical basis but not event by event. There is some overlap in the $X_{\max}$ distributions of photons and protons of the same energy, but the distributions are clearly different. The separation of both distributions becomes better for higher energies. Photon induced showers for which the preshower effect (section 4.3) happened can be barely discriminated from proton induced showers.

This difference in the depth of the shower maximum does not originate from a difference in the depth of the first interaction (figure 4.2). From figure 4.3 it can be concluded that this is mainly caused by the cut $X_{\max,\mathrm{vertical}} < 870\,\mathrm{g\,cm^{-2}}$. Especially at energies above $10^{19}\,\mathrm{eV}$ photons often show a rather high X_1 because of the LPM effect. Showers with a high X_1 often also have a high $X_{\max}$ and are therefore thrown out by the cut. The length of the shower development from the first interaction to the shower maximum is shown in figure 4.4. If the position of the first interaction was measurable, photons and protons would be much more separable. The difference in the $X_{\max}$ for photon and proton induced showers stems mainly from the length of the shower development. An

[6] see [56], e.g.
[7] 1452 m absolute altitude for ground level
[8] some are missing because the simulations never finished
[9] COrsika dAta accesS Tools, `http://www-ik.fzk.de/~rulrich/coast.html`

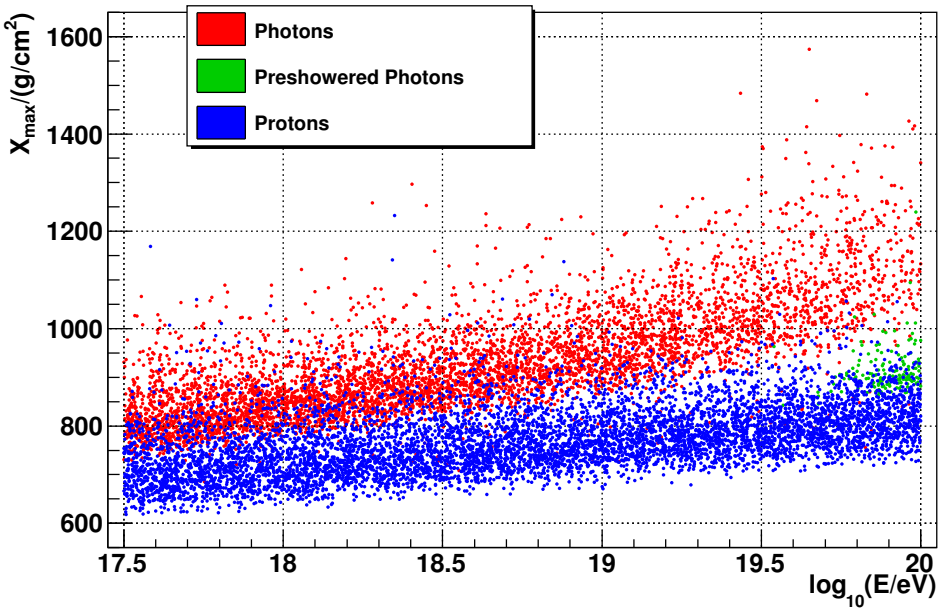

Figure 4.1.: $X_{\max}$ over logarithmic energy for photon and proton induced shower simulations. Photon induced showers affected by the preshower effect are shown in green. Only showers with $X_{\max}$ above the ground are included.

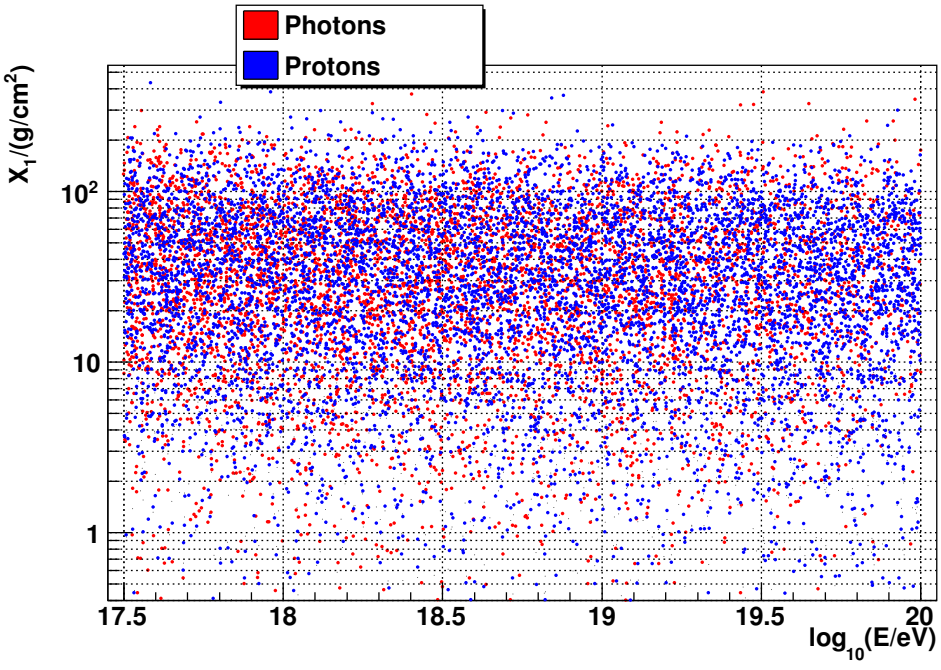

Figure 4.2.: Slant depth of first interaction X_1 over logarithmic energy for photon and proton induced shower simulations. Photon induced showers affected by the preshower effect are not shown. Only showers with $X_{\max}$ above the ground are included.

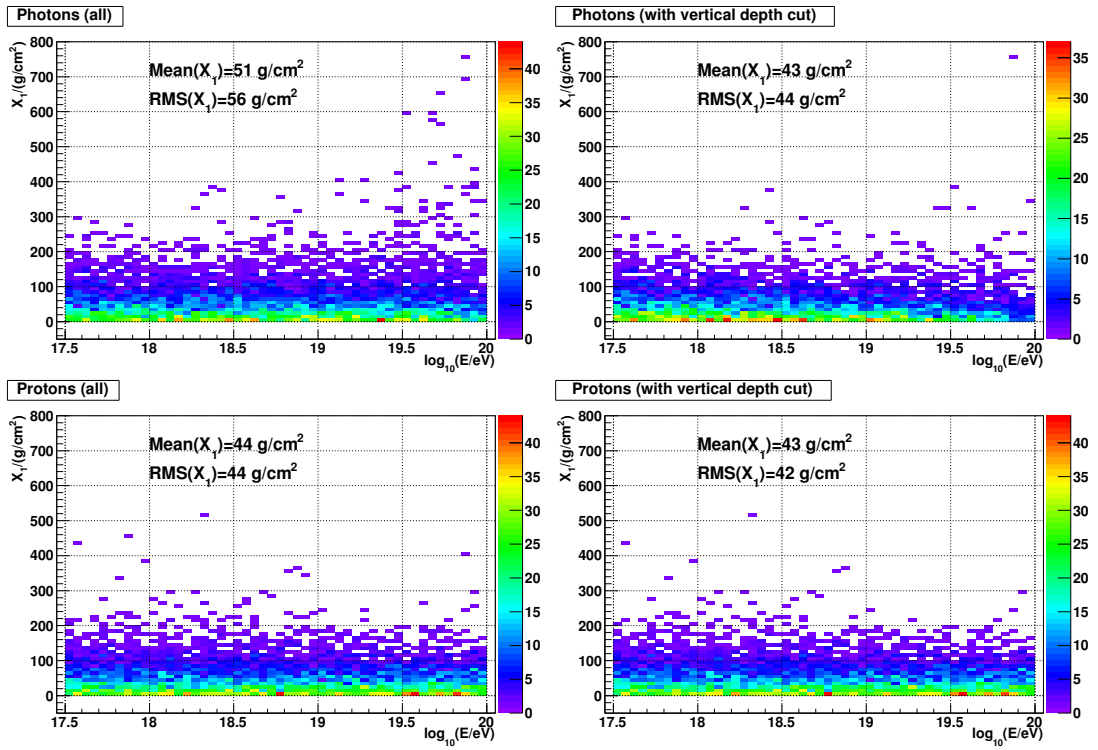

Figure 4.3.: Slant depth of the first interaction for photons and protons. Photons show a higher X_1, especially at higher energies (left). After the cut for showers that do not reach their maximum before they reach the ground (right) almost all photon induced showers with high X_1 are removed.

additional broadening of the distributions is caused by fluctuations of X_1. The length of the shower development is influenced by the number of particles produced in the first interaction. For photon primaries the main process is pair production, in which the energy is distributed onto two particles. In the hadronic interaction of hadron induced air showers, the energy is distributed onto a much greater number of particles in the first interaction, which leads to a faster overall shower development. Also the LPM effect (section 4.2) can prolong the shower development for photon primaries.

Although some photonuclear interactions happen in the electromagnetic cascades of the photon induced air showers, the fraction of hadrons and subsequently also of muons is much lower for photon induced showers than for proton induced showers. This can be seen in figures 4.5 and 4.6. Also the hadronic and muonic fractions are nearly independent of the energy for photons, while there is a clear energy dependence for protons. For some photon induced showers there are very high hadronic and muonic fractions. It is likely that in these showers a photonuclear interaction happened in one of the first interactions and a large fraction of the shower energy is transferred into a hadronic cascade. These showers are very similar to proton induced showers.

The different muonic content of the shower affects the Surface Detector measurements which mostly measure muons. There are other differences in the lateral particle distribution, which become relevant when Surface Detector data is used for photon identification (see [28]), but which are not shown here.

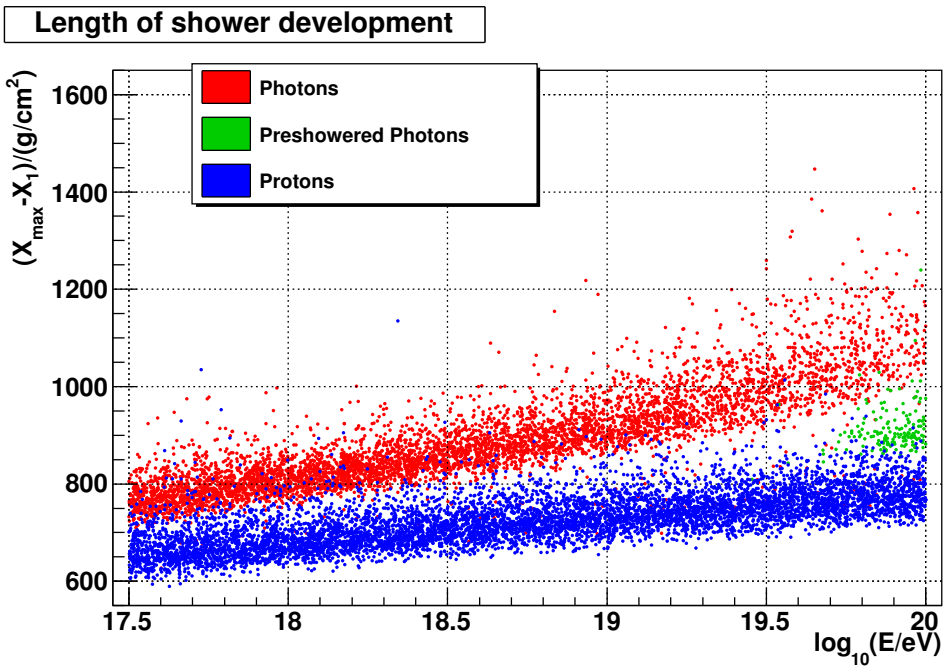

Figure 4.4.: $X_{\max} - X_1$ over logarithmic energy for photon and proton induced shower simulations. Photon induced showers affected by the preshower effect are shown in green. Only showers with $X_{\max}$ above the ground are included. Photons can be better discriminated from protons compared to figure 4.1.

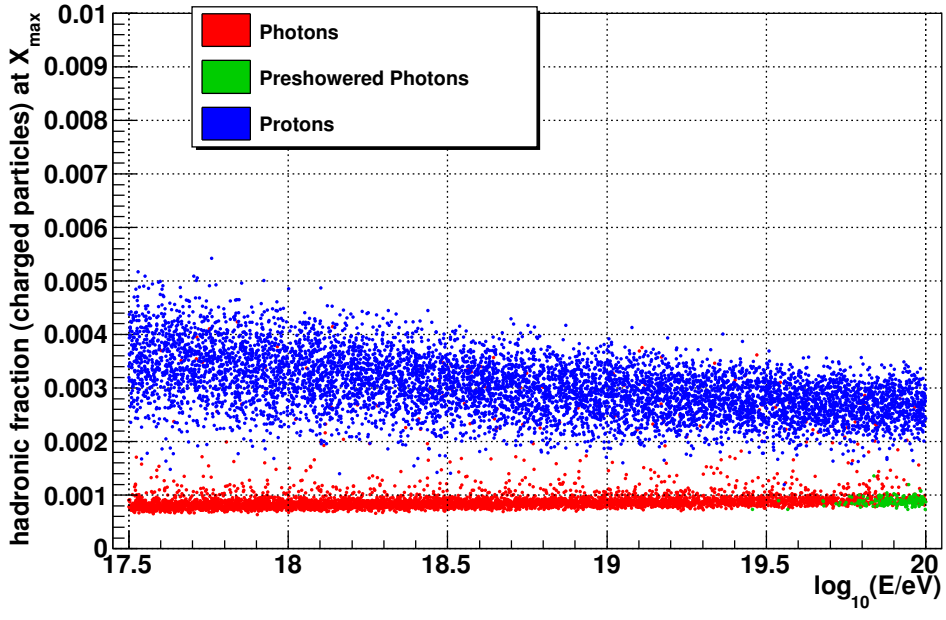

Figure 4.5.: Hadronic fraction of charged particles for photon and proton induced shower simulations. Photon induced showers affected by the preshower effect are shown in green. The fraction is calculated at shower maximum $X_{\max}$. Only showers with $X_{\max}$ above the ground are included.

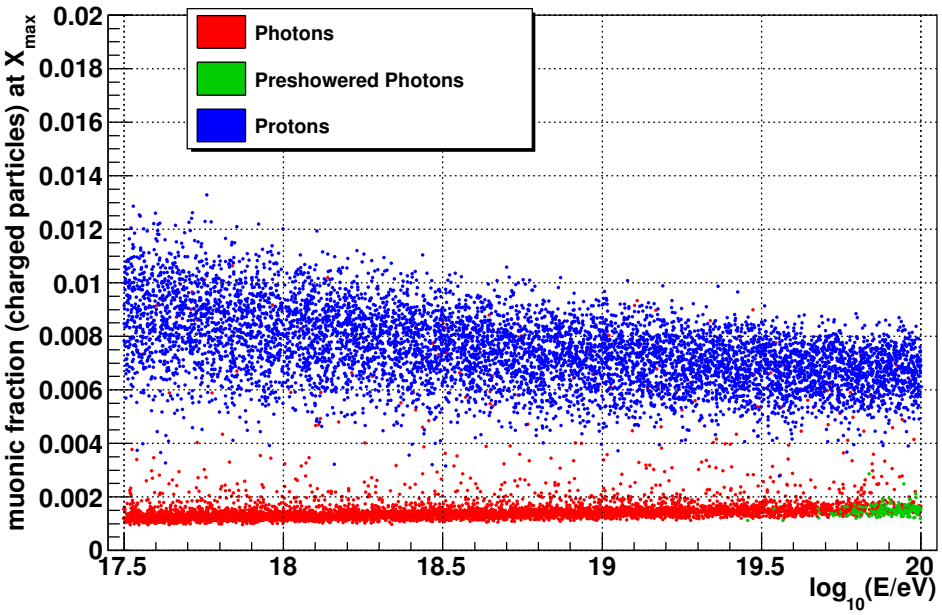

Figure 4.6.: Muonic fraction of charged particles for photon and proton induced shower simulations. Photon induced showers affected by the preshower effect are shown in green. The fraction is calculated at shower maximum $X_{\max}$. Only showers with $X_{\max}$ above the ground are included.

4.1.1. Invisible energy

While muons are created or decay, neutrinos are produced. These neutrinos withdraw energy from the shower and do not cause fluorescence light. Therefore they are called "invisible energy". Also high energy muons reaching the ground partly contribute to the missing energy. From the different muonic fractions shown in figure 4.6, a difference in the amount of invisible energy results for photons and protons. According to [44, Figure 2] the missing energy correction is in the order of 10 % for protons and in the order of 1 % for photons. In shower reconstructions of Fluorescence Detector data of the Pierre Auger Observatory, a correction for the invisible energy is applied using the average between proton and iron primaries [57]. For a photon primary this correction is wrong and has to be modified in the presented analysis. For an unknown primary, this has to be taken as a source of systematic uncertainty.

4.2. Landau-Pomeranchuk-Migdal effect

The LPM effect is one of the peculiarities of photon induced air showers. It is a quantum mechanical effect that reduces the cross section of e^+e^- pair production for photons in the field of nuclei. The interactions at multiple nuclei interfere destructively, which leads to a reduction of the cross section.

With increasing photon energy, the momentum that has to be transferred onto the nucleus in pair production becomes smaller. This momentum transfer is realized through the exchange of a virtual photon. When the wave length of the virtual photon becomes large compared to the distance between multiple nuclei, the original photon travels past multiple nuclei while the pair production and the emission of the virtual photon

is in progress. This distance traveled while emitting the virtual photon is called the formation length. The pair production at different nuclei while the photon travels the formation length interferes destructively, which leads to a reduction of the pair production cross section. The suppression increases with increasing photon energy and increasing material density. The suppression of the process is strongest for equal division of the energy between electron and positron. Therefore, an asymmetric energy division between positron and electron is favored. A very similar suppression occurs for electron bremsstrahlung. Due to the favored asymmetry in the energy division, the further interactions of the main secondary particle can again be suppressed by the LPM effect. So a large fraction of the original energy can be transported deep into the shower [58]. For a more detailed and quantitative description see [59].

For air showers the density dependence of the effect means that the suppression increases with the atmospheric depth[10]. This means the interaction probability is no longer constant per slant depth interval. As a consequence, the depth of the first interaction no longer follows an exponential distribution, but extremely high depths of first interaction are favored. Electromagnetic showers influenced by LPM effect show much higher fluctuations in the shower development compared to the absence of the LPM effect [58]. It can be shown that the LPM effect becomes noticeable for photon induced air showers for primary energies above 10^{18} eV [60].

In CORSIKA the LPM effect is implemented through a correction factor relative to the standard Bethe-Heitler cross-section [49]. The type and location of the interaction is calculated without taking the LPM effect into account. After that the correction factor is calculated and the interaction is discarded[11] with a probability of one minus the correction factor. Nevertheless, the first interaction is written to the output file even in case it is discarded, with the true first interaction happening deeper in the atmosphere. The event header of the output file, where normally the first interaction is stored, can no longer be modified after being written at the place of the normal first interaction. So instead, for this analysis, CORSIKA is modified so that the corrected height of the first interaction is written to the event terminator. With the height of the original first interaction still in place in the output file, the delay of the first interaction can be investigated (figure 4.7). The first interaction is only meaningful when no preshower (see section 4.3) has happened, so showers affected by the preshower effect are not included in figure 4.7.

[10] mainly an integral over air density
[11] the primary particle is just tracked further

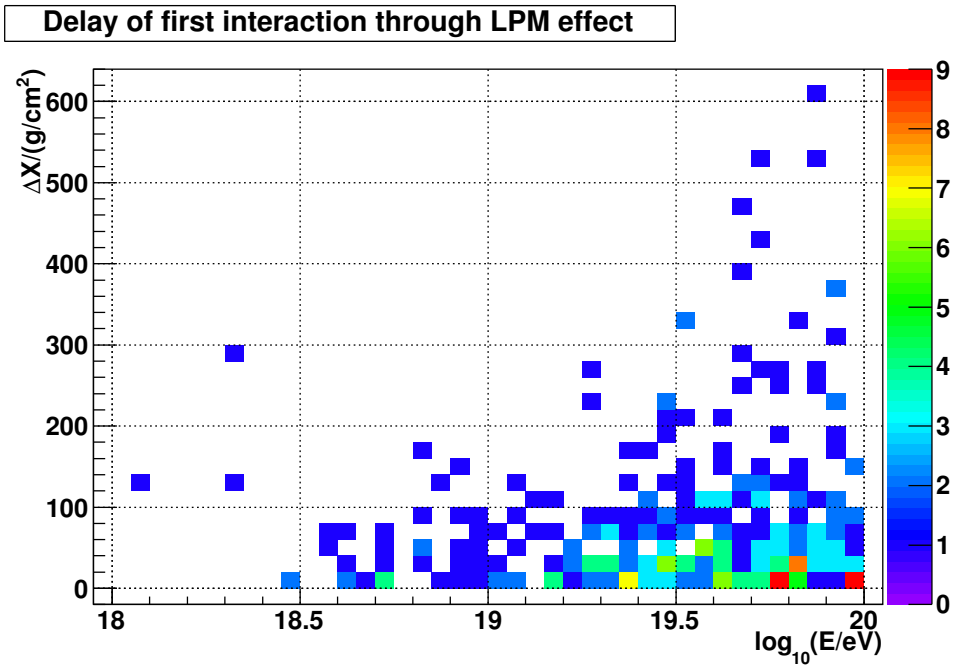

Figure 4.7.: Delay of the first interaction through LPM effect. The difference of the slant depths of the true first interaction and the first discarded interaction is shown. Approximately 150 showers are used per energy bin, showers affected by the preshower effect are excluded.

4.3. Preshower effect

Geomagnetic cascading or the *preshower effect* is the second peculiarity of UHE photons. Here the primary photon undergoes pair production in the magnetic field of the Earth before entering the atmosphere. The resulting electrons do bremsstrahlung in the same magnetic field. Therefore, a whole bunch of lower energetic photons and one or more e^+e^- pairs enter the atmosphere. When this happens, the particles generally have an energy which is too low for the LPM effect to be significant. So the preshower effect competes with the LPM effect. Like the LPM effect, the preshower effect becomes more likely at higher photon energies, with significant probabilities above some 10^{19} eV. The probability for a geomagnetic cascade to happen is also dependent on the transverse magnetic field, and therefore, on the arrival direction of the photon and the location on earth. For further information see [61] and [62].

In CORSIKA, the preshower effect is simulated with the PRESHOWER module described in [63]. For a geomagnetic field as over Malargüe, the probability for a geomagnetic cascade to happen is simulated. A significant fraction ($\gtrsim 5\,\%$) of primary photons develops a preshower at energies starting at roughly $10^{19.7}$ eV. It raises to roughly 40 % at 10^{20} eV. This is shown in figure 4.8. For the calculation of the preshower probability, 600 simulated CORSIKA showers per energy bin can be used[12]. The usual $\cos(\theta)\cdot\sin(\theta)$ zenith angle distributions up to zenith angles of $\theta = 65°$ is used. The direction dependence of the preshower effect is not investigated here. The number of particles entering the atmosphere, after geomagnetic cascading has taken place, is shown in figure 4.9. It can be seen that the preshower produces some hundred secondary particles. From figure 4.1 it can be concluded that, after a preshower happened, a photon primary at 10^{20} eV

[12] the same 300 showers used to study the LPM effect and 300 additional showers, which have been simulated before doing all modifications to CORSIKA

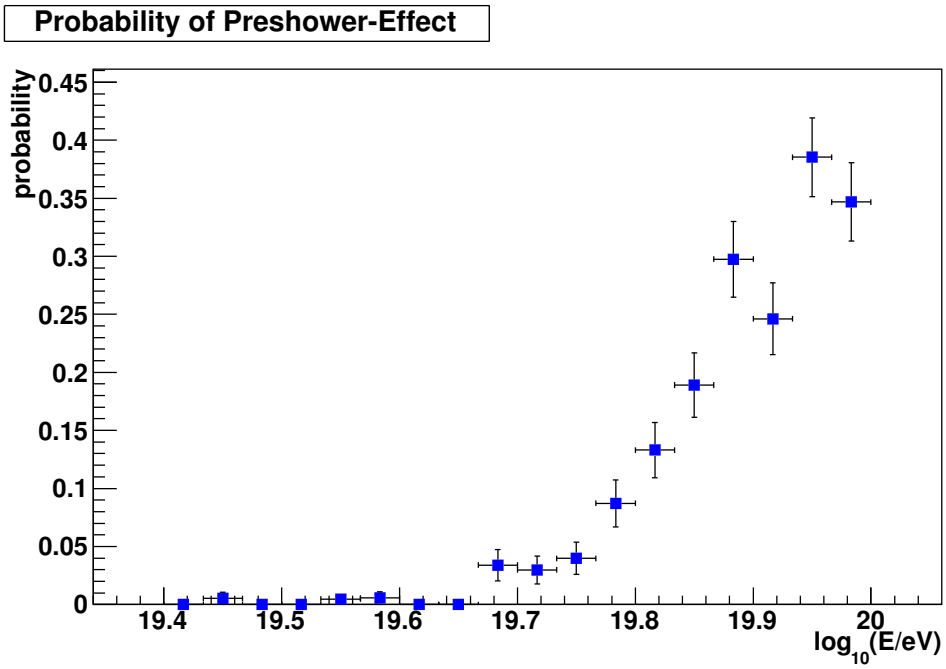

Figure 4.8.: Preshower probability averaged over all simulated showers (isotropic zenith angle distribution for a flat detector up to zenith angles of 65°). Determined from 600 simulations with the PRESHOWER module in CORSIKA per energy bin. The error bars in x direction correspond to the bin width.

looks like a photon at $\approx 10^{18.5}\,\mathrm{eV}$ in terms of $X_{\max}$. Showers induced by a photon with preshower are much more similar to proton induced showers at $10^{20}\,\mathrm{eV}$, compared to showers induced by an unconverted photon.

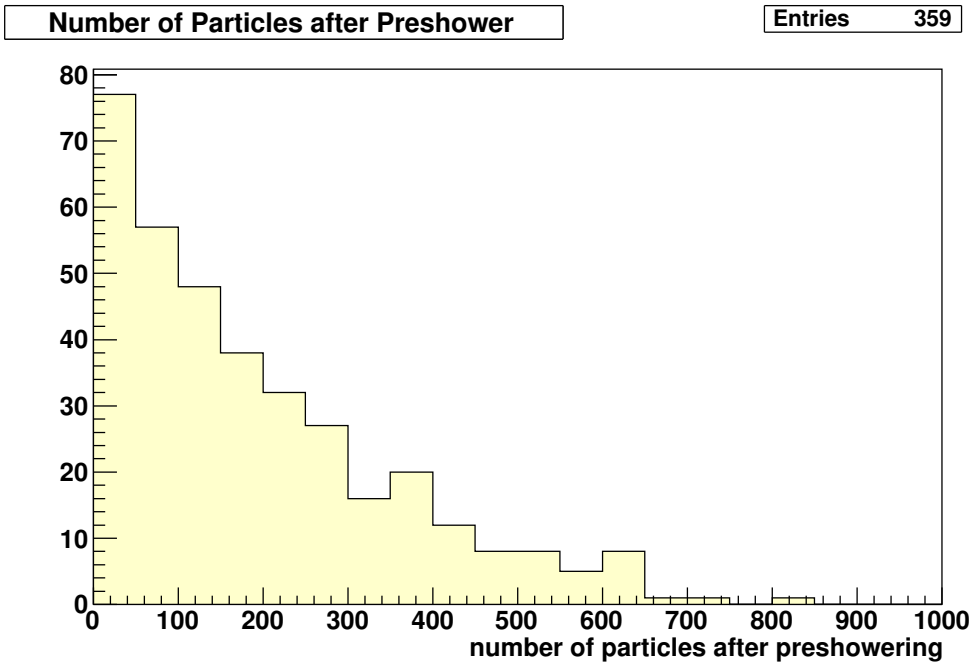

Figure 4.9.: Histogram of the number of particles entering the atmosphere after preshowering. Determined from 600 simulations per energy bin with the PRESHOWER module in CORSIKA. Energy from 10^{19} eV to 10^{20} eV with spectral index $\gamma = 1$. Simulations without a preshower are not included.

4.4. Current limits on photon flux and photon fraction at ultra-high energies

Although much work has been put into the search for ultra-high energy photons with air shower experiments, none have been found until now. Instead, limits on the photon flux[13] and photon fraction are calculated. The photon fraction f_γ is the number of primary photons N_γ divided by the number of all arriving primary particles N_{tot}:

$$f_\gamma = \frac{N_\gamma}{N_{\text{tot}}} \tag{4.1}$$

More and more exotic top-down models of UHECR production can be excluded, because the predicted photon flux is not observed. In figures 4.10 and 4.11 current limits on photon fraction and photon flux are shown. More details and references to the various shown analyses and theoretical predictions can be found in [64] and [65].

The shown analyses do not use directional information. The limits are averaged over the whole visible sky. Especially for photons also directional limits are interesting. One analysis doing this is shown in [28]. A combination of multiple observables of golden hybrid[14] showers achieves a better discrimination power, compared to discrimination with only SD or FD observables. This improved discrimination power comes at the cost of higher systematic uncertainties. Directional limits on the photon fraction in the order of 10% everywhere on the visible sky are deduced (see figure 4.12).

[13] photons per area, per solid angle and per time
[14] separate FD and SD reconstruction of the same shower possible

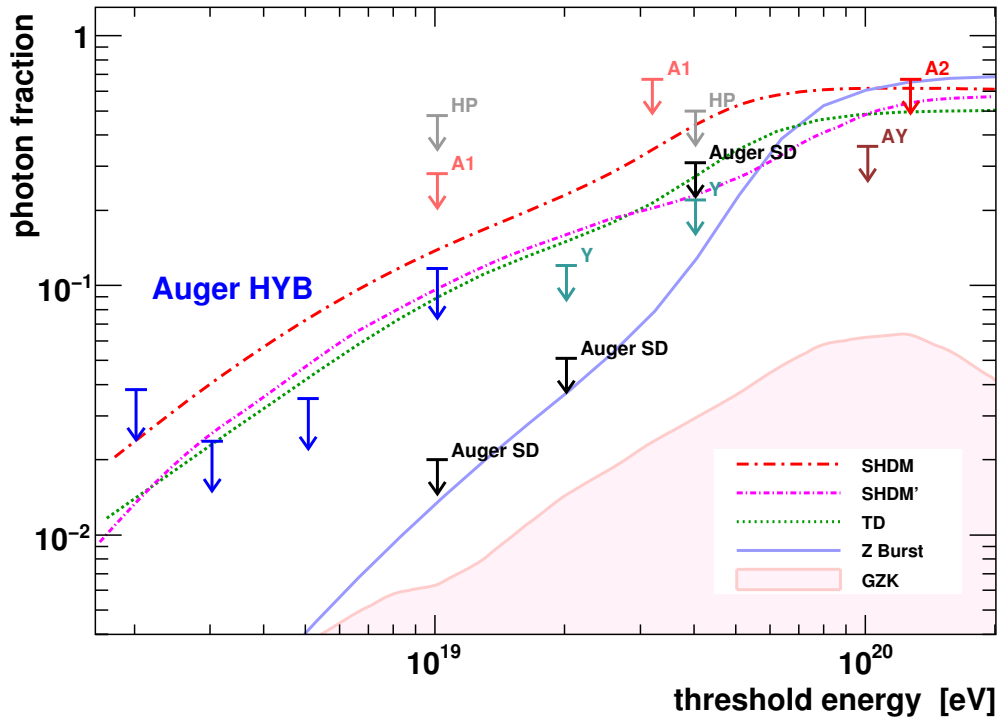

Figure 4.10.: Limits on the photon fraction from various experiments at 95 % confidence level and theoretical predictions. The Auger Hybrid limits (2009) are shown in blue and the Auger SD limits are shown in black. As a comparison limits from AGASA (A1, A2), AGASA-Yakutsk (AY), Yakutsk (Y) and Haverah Park (HP) are also shown. Various theoretical predictions from top down models are included as lines. The shaded area is the predicted fraction from GZK effect. Original and references can be found in [64].

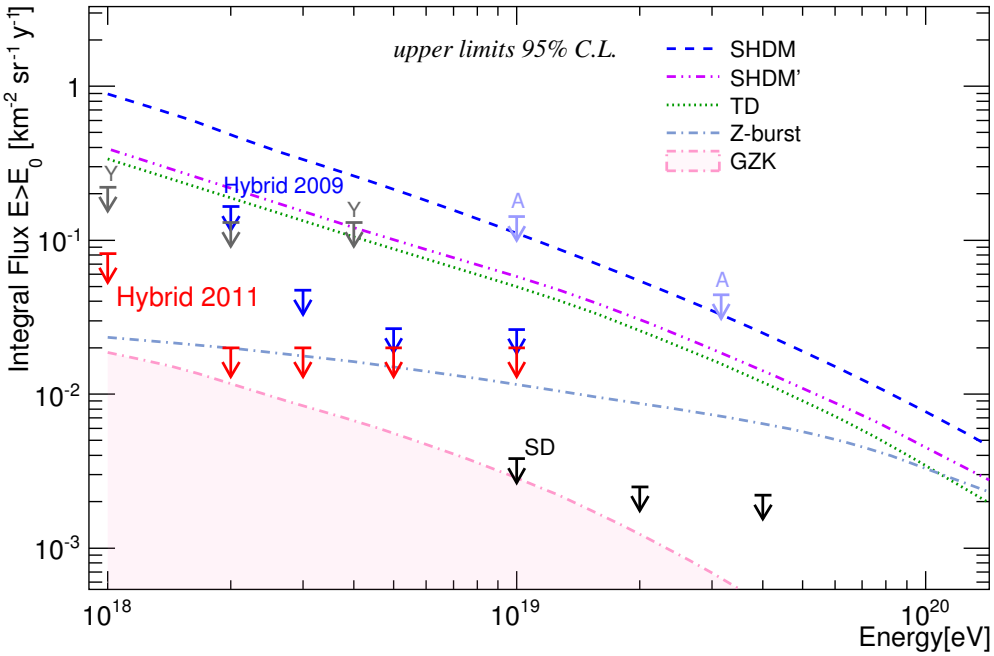

Figure 4.11.: Limits on the photon flux from various experiments at 95 % confidence level and theoretical predictions. Three analyses of Auger data (Hybrid 2009, Hybrid2011 and SD), AGASA (A) and Yakuts (Y) are shown. Various theoretical predictions from top down models are included as lines. The shaded area is the predicted flux from GZK effect. Original and references can be found in [65].

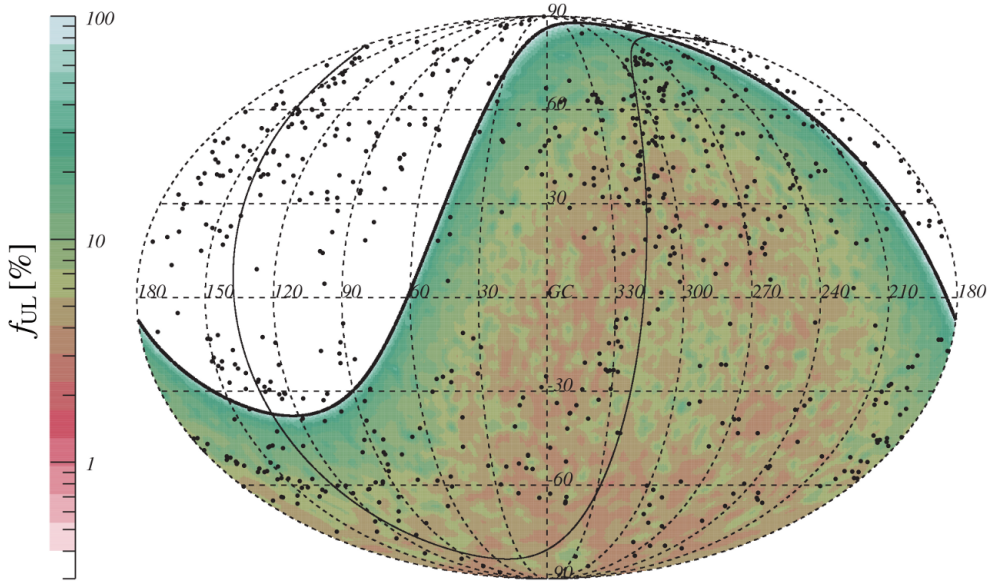

Figure 4.12.: Directional upper limit on the photon fraction at 90 % confidence level for a gaussian smearing of 1°. Some active galactic nuclei as potential sources are shown in black. Original in [28, Figure 9.25].

5. Photon point source search

5.1. Idea

One of the features which sets photons apart from charged hadrons is that they are not deflected by magnetic fields. This makes them especially suited for anisotropy studies and to identify their sources. Assuming that there are point sources (less than a degree in diameter[1]) of ultra-high energy photons, it can be tried to confirm or at least set limits on their existence.

A major problem while searching for photon induced air showers is the hadronic background, which produces a not negligible amount of showers with an $X_{\max}$ in the range where photon induced showers are expected. The exact distribution of $X_{\max}$ of the background can not be easily simulated, because of uncertainties in the composition and energy spectrum of the hadronic background. More uncertainties are arising from the hadronic interaction models for air shower simulations. In searches for photons, the hadronic background is often just ignored and conservatively included in the limit estimation[2]. In the search for photon point sources, the background can be estimated from data outside of the region of interest. This assumes the same hadronic composition in the *signal region* and in the *background region*. This can be assumed, because the magnetic fields should smear possible hadrons from the source candidate, but it has to be checked.

Based on a comparison of the $X_{\max}$ distribution between signal and background region, a non-vanishing photon count can be identified, or limits on the photon count can be set. A possible diffuse or isotropic photon fraction is included in the hadronic background and can not be identified with this method. Together with the total count of the observed events a limit on the photon fraction can be set.

In section 5.2 the data set for the analysis and the used quality cuts are shown. Also a cut on the maximum uncertainty of the arrival direction is discussed (section 5.2.2). After a short discussion of Centaurus A as a source candidate (section 5.3), the selection of the layouts of signal region and background region for the photon point source search is shown and motivated (section 5.4). To match the zenith angle distribution of the events from the signal region, the zenith angle distribution of the used shower simulations is reweighted in section 5.5. In section 5.6 the effect of a wrong missing energy correction for photon induced showers is demonstrated and a correction of the reconstructed shower energy is applied. A cut on X_{max} to discriminate between photons and hadrons is introduced in section 5.7, to be able to estimate the relative exposure of background region and signal region and to test the compatibility of the hadronic background. Afterwards the compatibility of the hadronic background is tested in section 5.8. In section 5.9 a formula for the estimation of the significance of observations in counting experiments is deduced. The deduced formula is applied to the number of events in the signal and background regions in section 5.10. Because no over-fluctuation of sufficient

[1] The central region of Centaurus A has a diameter of about a third of a degree

[2] this degrades the resulting limits

significance can be found, upper limits on the number of photon induced events in the signal region are set in section 5.11. In section 5.12 this limit is converted to a limit on the photon fraction, including a correction for the different acceptances of detector and used quality cuts for photons and protons (section 5.12.1).

5.2. Used data set

For the analysis, hybrid[3] ADSTs from the standard Auger Observer[4] reconstruction are used. Only Fluorescence Detector observables are used. The ADST release v7r3 is used, which uses $\overline{\text{Off}}\underline{\text{line}}$ v2r7p5 for reconstruction. All data from 2004 up to (and including) September 2011 is used. The used data cuts are given in section 5.2.3. After all cuts, 79195 events with energies above 10^{17} eV are available, which corresponds to an eposure in the order of $100\,\text{km}^2\,\text{sr}\,\text{yr}$.

For some parts of the analysis, air shower simulations for photons and protons are used. These are done with a modified CORSIKA version 6.980. Two bug fixes are included. One for the erroneous angle cut for ω-mesons and one for the never ending shower simulations (see section 4.0.1).

The simulations are done using QGSJET-II-03 ([51] and [52]) and FLUKA 2011.2.3 ([53], [54]) as hadronic interaction models and EGS4 ([55]) as electromagnetic interaction model. All showers with photons as primary particle are simulated with the PRESHOWER option enabled. The LPM effect is enabled for the simulations. All events are simulated with a continuous energy distribution with a spectral index of $\gamma = 1$. This means a constant number of events is located in every energy bin, with bin borders equally spaced in logarithm of the energy. The zenith angle θ is distributed as $\cos\theta \sin\theta$, which is correct for a flat detector. The thinning usually used for Auger simulations[5] is used. That means a thinning of 10^{-6} with an energy dependent maximum weight of $E \cdot 10^{-6}$ (evaluated at lower energy bin border). For further simulation parameters see the steering card in appendix A.1.

The simulations of photon and proton induced air showers are done in energy bins with a width of 0.1 in $\log_{10} E$. In each energy bin between $10^{17.2}$ eV and $10^{17.5}$ eV, 1000 events are simulated for each primary. Up to $10^{18.5}$ eV 600 events are simulated in each energy bin and up to 10^{19} eV 400 events are simulated in each energy bin and for photons and protons each.

The simulated CORSIKA showers are then processed through $\overline{\text{Off}}\underline{\text{line}}$ for the detector simulation and reconstruction. The ideal SD array is used. HEAT is disabled for the simulation. Mainly the $\overline{\text{Off}}\underline{\text{line}}$ module sequence of the `HdSimulationReconstruction` example is used with the difference that the `FastTankSimulatorOG` module is used instead of the normal `G4TankSimulatorOG` to speed up SD simulation. As long as no SD-only observables are used, this should not affect the analysis[6]. Every CORSIKA shower is reused 10 times with different positions of the shower core, distributed randomly and uniformly over the whole SD array.

[3] Events have been observed by the Fluorescence Detector and at least one SD station.
[4] `http://augerobserver.fzk.de`
[5] see [56], e.g.
[6] In hybrid mode, the FD reconstructions uses SD only for timing information and to locate the shower core.

5.2.1. Stereo event handling

Sometimes a single air shower is seen by more than one telescope site and can be reconstructed independently for every site. The best way to deal with this situation is to use the standard uncertainty-weighted mean of the various observables [66, eq. 11.26]:

$$\bar{Y} = \frac{\sum\limits_i Y_i \cdot w_i}{\sum\limits_i w_i} \tag{5.1}$$

$$\sigma(\bar{Y})^2 = \frac{1}{\sum\limits_i w_i} \tag{5.2}$$

where

$$w_i = \sigma(Y_i)^{-2} \tag{5.3}$$

Here $\sigma(Y_i)$ is the uncertainty on the observable Y_i coming directly from the χ^2-fit. Equation 5.1 gives the best estimator for Y, which can be the energy E of the primary particle or the slant depth $X_{\max}$ of the shower maximum. This is implemented as standard functionality in the ADST toolkit.

The other interesting observables are the arrival directions of the observed shower in local (azimuth and zenith) or equatorial (right ascension and declination) coordinates (see appendix B.3). These directions are given as pairs of coordinates with the corresponding uncertainties and correlation coefficient ρ. From these, the 2×2 correlation matrix can be constructed (x and y are placeholders for the two coordinates):

$$\underline{\mathbf{V}} = \begin{pmatrix} \sigma_x^2 & \sigma_x \sigma_y \rho \\ \sigma_x \sigma_y \rho & \sigma_y^2 \end{pmatrix} \tag{5.4}$$

Equations 5.1 and 5.2 are also valid for vector-valued $\mathbf{X}$ when w_i is replaced by $\underline{\mathbf{V_i}}^{-1}$ and all divisions are replaced by multiplications with the inverted matrix [66, 11.5.2]:

$$\bar{\mathbf{X}} = \left(\sum_i \underline{\mathbf{V_i}}^{-1} \right)^{-1} \left(\sum_i \underline{\mathbf{V_i}}^{-1} \mathbf{X_i} \right) \tag{5.5}$$

$$\underline{\bar{\mathbf{V}}} = \left(\sum_i \underline{\mathbf{V_i}}^{-1} \right)^{-1} \tag{5.6}$$

The periodicity in right ascension or azimuth at 360°/0° has to be taken into account. This can lead to a problem when the true direction is at this border, and two measured directions are at both sides of the border (e.g. 1° and 359°). In this case the correct result should be ≈ 0°. If the coordinates differ by more than 180°, the lower one is increased by 360°, so that the coordinates differ by less than 180° (359° and 361° for the used example). If needed, the resulting mean has to be shifted back to 0°–360°.

The second possible problem is that declination (or zenith) values outside the valid range are calculated. Values of the declination smaller than −90° or greater than 90° are interpreted as "journeys over the pole, coming from the given right ascension direction". That means the right ascension has to be changed by 180° and the declination δ is changed to $180° - \delta$ (or $-180° - \delta$, for $\delta < -90°$).

The first correction might lead to problems at the poles, while the second only appears at the poles. All events in this analysis for which the directions matter are far enough away from the celestial poles ($\delta_{\mathrm{CenA}} \approx -43°$) to not care about this. The reconstructed zenith angles and azimuths are not used to make quantitative deductions. The steps of the analysis which use the zenith angle only make qualitative deductions and the problems are ignored for the few events being potentially affected by this.

5.2.2. Maximum angular error cut

Data quality cuts for analyses using FD hybrid data normally contain cuts on the maximum uncertainties on E (relative) and X_{max} (absolute). What is normally not used is a cut on the maximum uncertainties of the arrival directions. For this the known uncertainty in the two orthogonal directions should be converted to one "angular uncertainty" which can be used for the cut.

First of all, the uncertainty in right ascension or azimuth has to be scaled down by $\cos(dec)$ or $\sin(\theta)$. This is to account for the fact that a difference of one degree (coordinate distance) of right ascension is a bigger physical distance at the equator than near the poles.

There are two obvious possibilities:

- use the maximum of the two uncertainties
- use the quadratic sum of the two uncertainties

On the second sight both of them are not satisfactory.

The maximum of the two uncertainties is only directly meaningful for a vanishing correlation coefficient $\rho = 0$. In other cases, the direction of the maximum uncertainty is not identical to one of the coordinate directions. To get the "real" maximum and minimum uncertainties, the coordinate axes have to be rotated to a coordinate system with uncorrelated quantities ($\rho' = 0$). This means, the transformed matrix $\underline{\mathbf{V}}'$ is diagonal with its eigenvalues (the maximum and minimum variances) on the two diagonal places. From linear algebra one knows that the eigenvalues of $\underline{\mathbf{V}}$ are the same as the ones of $\underline{\mathbf{V}}'$. Therefore, it is sufficient to calculate the eigenvalues of $\underline{\mathbf{V}}$ to get the maximum and minimum uncertainties. Using equation 5.4:

$$\det\left[\underline{\mathbf{V}} - \sigma^2 \underline{\mathbf{1}}_{\mathbf{2}\times\mathbf{2}}\right] \stackrel{!}{=} 0 \tag{5.7}$$

$$(\sigma_x^2 - \sigma^2)\cdot(\sigma_y^2 - \sigma^2) - (\sigma_x\sigma_y\rho)^2 \stackrel{!}{=} 0$$

$$\Rightarrow \sigma^2_{\mathrm{max,min}} = \frac{\sigma_x^2 + \sigma_y^2}{2} \pm \sqrt{\frac{(\sigma_x^2+\sigma_y^2)^2}{4} + \rho^2\sigma_x^2\sigma_y^2} \tag{5.8}$$

Selecting the plus sign one obtains the maximum one-dimensional uncertainty.[7]

Using the quadratic sum results in the problem of how to interpret the result and how the uncertainty is defined in the first place. The usual definition is to have a chance of 68.27 % for the real value to be within the uncertainty interval. For $\sigma_{\mathrm{min}} \approx \sigma_{\mathrm{max}}$ the true value approximately follows a Rayleigh distribution [20] with parameter $\sigma = \sqrt{(\sigma_x^2+\sigma_y^2)/2}$ for which the 68.27 % quantile can be calculated numerically as $\sigma \approx 1.5\cdot\sqrt{(\sigma_x^2+\sigma_y^2)/2}$. This case is shown in figure 5.1.

[7] Note that $\sigma_x^2 + \sigma_y^2 = \sigma^2_{\mathrm{min}} + \sigma^2_{\mathrm{max}}$

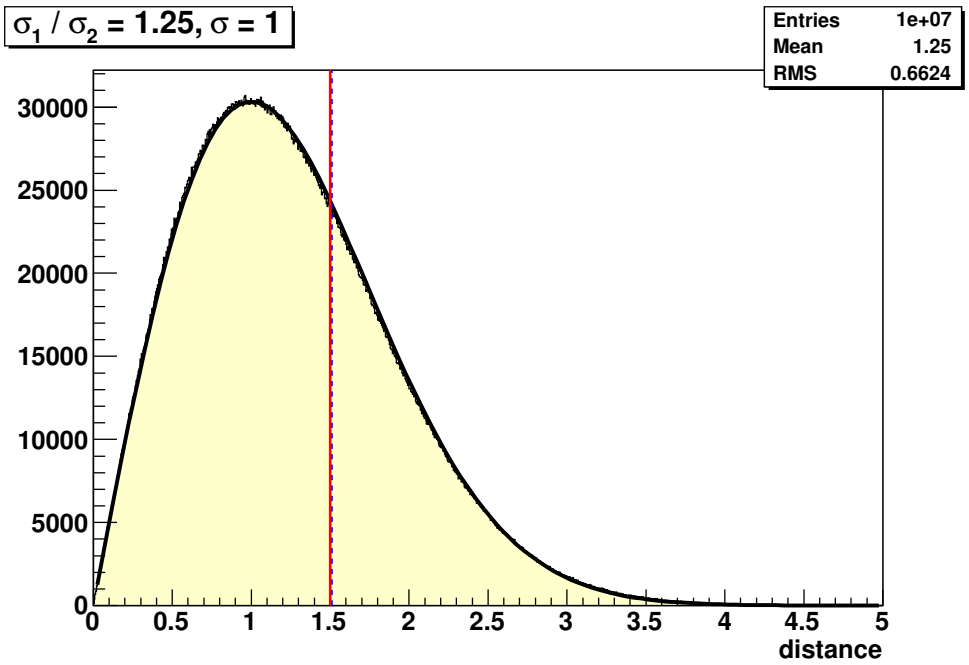

Figure 5.1.: Distribution of the quadratic sum of two normal distributed random variables with $\sigma_1/\sigma_2 = 1.25$ and $\sqrt{(\sigma_1^2 + \sigma_2^2)/2} = 1$. The distribution can be approximated by a Rayleigh distribution. The 68.27 % quantile (dashed line) is compared to 1.5σ (solid line).

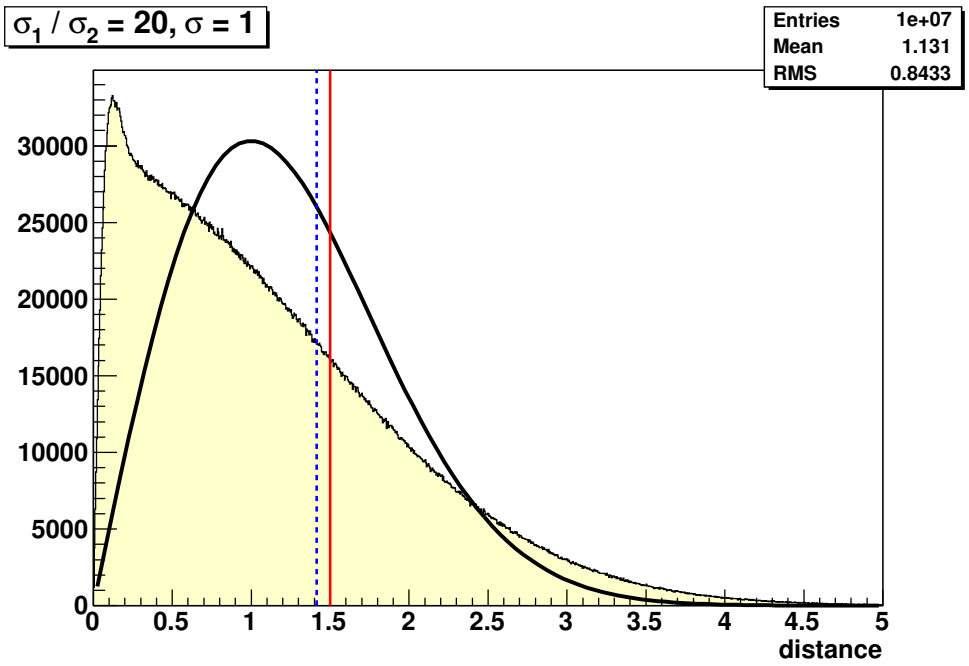

Figure 5.2.: Distribution of the quadratic sum of two normal distributed random variables with $\sigma_1/\sigma_2 = 20$ and $\sqrt{(\sigma_1^2 + \sigma_2^2)/2} = 1$. The distribution can no longer be approximated by a Rayleigh distribution. The 68.27 % quantile (dashed line) is compared to 1.5σ (solid line).

For the other case $\sigma_{\min} \approx 0$ (shown in figure 5.2) the distribution can be approximated by a half normal distribution and the 68.27 % quantile can be calculated as $\sigma \approx \sigma_{\max} \approx 1.4 \cdot \sqrt{(\sigma_x^2 + \sigma_y^2)/2}$. So

$$\sigma = 1.5 \cdot \sqrt{\frac{\sigma_x^2 + \sigma_y^2}{2}} \tag{5.9}$$

is used as a conservative estimator for the angular uncertainty for the maximum angular error cut.

5.2.3. Used cuts

Because not every detected event in the complete data set can be reliably reconstructed, some quality cuts have to be applied to the data before usage for the analysis. The cut files used with the ADST tool `SelectEvents` are shown in appendix A.2.

The shower core has to be within the detector array, that is within 1500 m to the closest hybrid station (`maxCoreTankDist 1500`). Events from a period without FD calibration or with detector problems are dismissed (`badFDPeriodRejection` for FD and `badPeriodsRejection` for SD). There have to be at least 5 Pixels in the shower axis fit (`nAxisPixels 5`), the reduced χ^2 of the time fit of the shower axis has to be below 5 (`timeFitChi2 5`) and the shower has to be downwards, that means the reconstructed zenith angle has to be below 90° (`maxZenithFD 90`).

The shower profile has to be described reasonably well with the Gaisser-Hillas (GH) function (`profileChi2 2.5`) and much better than with a linear function. The ratio between the χ^2 of the GH fit and a linear fit has to be below 0.9 (`profileChi2Ratio 0.9`). The reconstructed energy has to be above 10^{17} eV, (`minLgEnergyFD 17`), which mainly assures that the energy reconstruction has not failed completely (later on in the analysis stronger selections on the energy are done). The $X_{\max}$ resulting from the GH fit has to be within the observed field of view (FoV) (`xMaxInFOV 0`). The absolute uncertainty on $X_{\max}$ resulting from the Gaisser-Hillas fit has to be below $40\,\mathrm{g\,cm^{-2}}$ (`xMaxError 40`) and the relative uncertainty on the shower energy has to be below 20 % (`energyError .2`). The fraction of Cherenkov light in the shower has to be below 50 % (`maxCFrac 50`), because the reconstruction has not been tested for higher Cherenkov-fractions.

After the aforementioned quality cuts and after the combination of stereo events, 83120 hybrid events can be used. Also the cut on the angular uncertainty as defined in section 5.2.2 is used with a maximum angular uncertainty of 1.5°. This cut has an efficiency of 95.3 %. 79195 Events are used in the analysis.

Name of the cut	Argument	Event count	Efficiency
		1904000	
badFDPeriodRejection		1645538	86.4 %
maxCoreTankDist	1500	698266	42.4 %
nAxisPixels	5	600770	86.0 %
timeFitChi2	5	599500	99.8 %
maxZenithFD	90	514868	85.9 %
profileChi2	2.5	458491	89.1 %
profileChi2Ratio	0.9	149325	32.6 %
xMaxInFOV	0	136553	91.4 %
xMaxError	40	88235	64.6 %
energyError	0.2	87878	99.6 %
minLgEnergyFD	17	87220	99.3 %
maxCFrac	50	83714	96.0 %

Table 5.1.: Efficiency of the used quality cuts when applied to the Auger data. The correlations between the cuts are not studied. Stereo events observed by more than one telescope site are cut separately and counted for each site.

5.3. Centaurus A as a photon source candidate

There are only very few possible point sources for UHE photons. Galactic sources are generally assumed to be not able to produce particles (including photons) with high enough energies to be detected at the Pierre Auger Observatory. Most extragalactic sources have the problem that they are too far away. Due to interactions with low energy photons, like the cosmic microwave background, universal radio background or star light, UHE photons at about 10^{18} eV have an attenuation length of around 10 Mpc. See section 2.1.4 for further information. Therefore, only sources within a distance of 10 Mpc are reasonable candidates.

The only source candidate meeting this criterion is the radio galaxy Centaurus A at a distance of roughly 4 Mpc (see section 2.1.3). This source candidate is used for the further analysis.

5.4. Selection of signal region and background region

An important role in this analysis is played by the selection of the size and layout of the signal and background regions. The signal region should be big enough to contain (almost) all photons from the source candidate (if any), but should not be much bigger than needed to reduce the unrelated background. With a maximum (Gaussian) uncertainty of 1.5°, a typical uncertainty of 1° and a diameter of the core region of Centaurus A of less than 0.5°, a radius of 4° is chosen for the signal region. With this region size, the major part of the giant radio lobes of Centaurus A is also located in the signal region. A size of 3° would have even less background without loosing much signal, but the statistical uncertainty of the analysis would be increased because of less statistics for the background estimation. The size selection was done before the analysis steps of section 5.10 ff. were implemented. It does not impose a bias on the results for trying too many values.

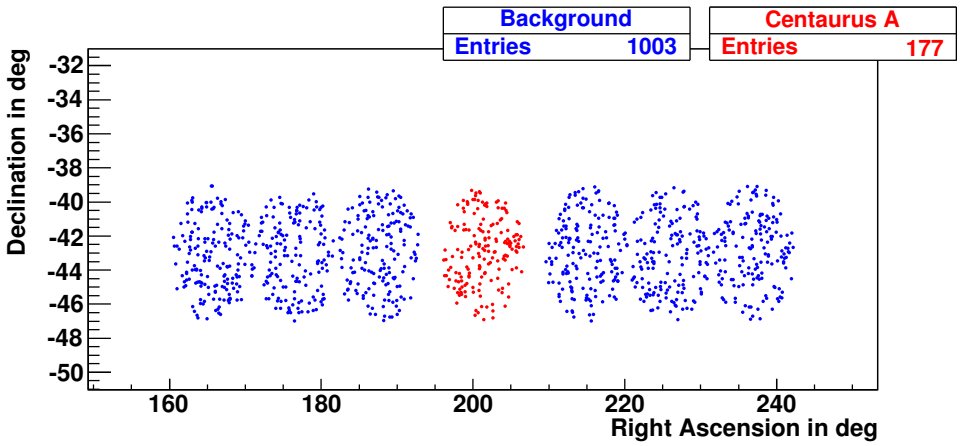

Figure 5.3.: Distribution of the events from signal and background regions on the sky. The radius of the signal region and every background region circle is 4°. The distance between Centaurus A and the first background region circle is 10°. Simple equirectangular projection with right ascension on abscissa, declination on ordinate.

No difference in the $X_{\max}$ distribution should arise from the selection of the regions alone. With the signal region fixed, the choice of the background region has to be done to achieve this. The layout of the background region is chosen to have the same (or very similar) zenith angle distribution in signal and background region. This is because the $X_{\max}$ distribution is correlated to the zenith angle distribution (section 5.4.1). Additionally, the background region must not contain any photon events originating from the source candidate. So the background region should not be directly adjacent to the signal region. A distance of 6° between the source candidate and the background region is assumed to be sufficient. To reduce statistical uncertainties, the background region should have the highest possible size.

To calculate the angular distance between two points (e.g. an event and the source candidate) the correct formula for distances on the sphere has to be used (declination δ and right ascension λ) [67, 3.208a]:

$$d = \arccos\left[\sin\delta_1 \sin\delta_2 + \cos\delta_1 \cos\delta_2 \cos(\lambda_1 - \lambda_2)\right] \tag{5.10}$$

The resulting angular distribution of the events is shown in figure 5.3. Because the declination distribution is strongly correlated to the zenith angle distribution, the same form in declination as the signal region is needed for the background region (section 5.4.2). Because there is also a small right ascension dependence of the zenith angle distribution, only three background region circles are used on each side of the signal region, which corresponds to a maximum distance of roughly 40° in right ascension for the background events from the source candidate (section 5.4.3).

5.4.1. Correlation between $X_{\max}$ and zenith angle

The $X_{\max}$ distribution is correlated to the zenith angle distribution as can be seen in figure 5.4.

The width of the bins in zenith angle in figure 5.4 is chosen such that there is equal

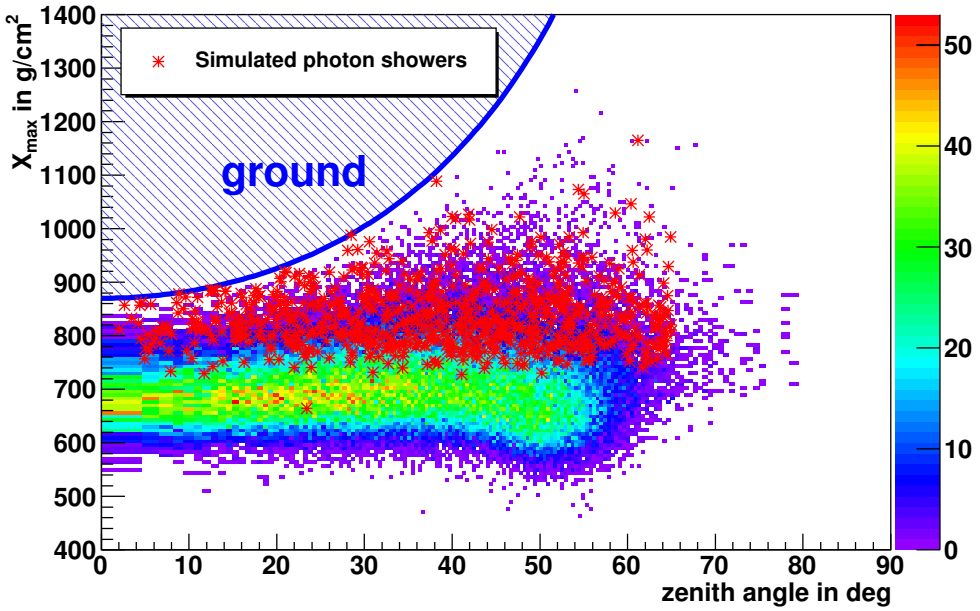

Figure 5.4.: Correlation between $X_{\max}$ and the zenith angle in the all-sky Auger data set after quality cuts from section 5.2.3. The bins in zenith have equal geometrical exposure. CORSIKA photon simulations are superimposed in red as comparison. Showers with an $X_{\max}$ in the region marked "ground" can not happen, because their shower maximum would be below the ground. The most important correlations are visible for showers with the highest $X_{\max}$, where most of the photons are located.

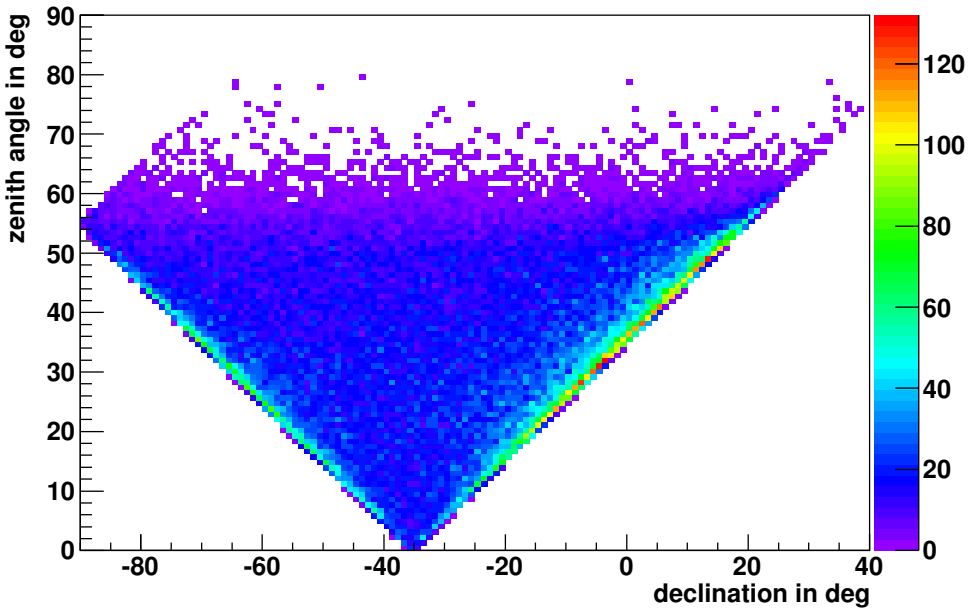

Figure 5.5.: Correlation between zenith angle and declination for the used Auger all-sky data set after quality cuts.

geometrical exposure in every zenith angle bin. The geometrical exposure is proportional to $4\sin(\theta)\cos(\theta) = 2\sin(2\theta)$. $\cos(\theta)$ is the projection of the surface detector onto the shower axis. $\sin(\theta) \cdot \mathrm{d}\theta$ is proportional to the solid angle element corresponding to the zenith interval $[\theta, \theta + \mathrm{d}\theta]$. That means the bins have to be equidistant in $\int 2\sin(2\theta) = -\cos(2\theta)$. The borders of the bins are therefore not equidistant in zenith angle although a linear zenith angle axis is used.

The correlation of X_{max} to zenith angle happens mainly because one can only reliably reconstruct shower observations where the shower has reached its maximum of development before reaching the ground. Because the slant depth of the ground level increases with increasing zenith angle, higher X_{max} values are possible at higher zenith angles. The slant depth of the ground in Malargüe can be approximated as $(870\,\mathrm{g\,cm^{-2}})/\cos(\theta)$ for $\theta < 60°$. This is especially important for photon induced showers, which generally have a higher X_{max} than hadron induced showers.

5.4.2. Choice of declination

The declination distribution, which can in principle be freely chosen for the background region, is the factor with the most influence on the zenith angle distribution. It can be seen that the declination distributions have to be identical in signal and background region. The easiest way to achieve this is to use one or more non-overlapping circles with the same radius and same declination of the center as the signal region.

In figure 5.5 the correlation between the declination and the zenith angle is shown. The triangle-like structure can be easily understood. The point with the declination of $-90°$ is the celestial south pole, which always has a fixed zenith angle equal to $90° + \delta$ with $\delta = -35.35° < 0$ being the latitude of Malargüe. With increasing declination, the points on the celestial sphere form circles of increasing diameters, which at some point reach below the horizon and run through the zenith point. With even further

increasing declination the circle no longer reaches the zenith and is completely located below the horizon when the declination is greater than $90 - \delta$. Some zenith-declination combinations at the border of the possible range are over-represented. This is caused by the fact that (on the sphere) the lines of constant declination and constant zenith angle are nearly parallel at these coordinates. Therefore, the created area element spanned by infinitesimal changes in declination and zenith angle becomes very large. In section 5.5 the particular comparison between the zenith angle distribution for isotropic events (all-sky) and for events with a declination distribution like in the signal region is shown. The accumulation at the borders is also visible there.

5.4.3. Choice of right ascension

What is still left to choose is the right ascensions of the positions of the background region centers. The obvious choice is to have the centers distributed symmetrically with respect to the signal region. The centers at each side of the signal region should have a distance of their centers of twice the radius (the distance of their right ascensions can be calculated by an inversion of equation 5.10). To get the maximum possible event count and the least possible statistical fluctuations in the background regions, the maximum count of circular background regions that is possible without overlap should be used. However, this is not necessarily the best choice, because also the region selection in right ascension can influence the zenith angle distribution. This does not follow from simple geometrical considerations like it is the case for the declination distribution and can not be calculated easily. Therefore the distance in right ascension between background region and the source candidate should be minimized.

The exposure for events at different right ascensions is different (cf. figure 5.6). The part of the sky that has its upper culmination at midnight during the summer is called "summer sky". The "winter sky" is defined accordingly. The summer sky and the winter sky are also partially visible during the other seasons, when the sky regions not yet or no longer culminate during the measurements. It can be expected that the summer sky has a relatively larger fraction of events taken in spring or autumn than the winter sky, because of the different lengths of the nights. Therefore, a difference in the zenith angle distributions for the summer sky and the winter sky can be expected. Also the effect of the different atmospheric conditions might be different for different zenith angles. This expectation seems to be justified as can be seen in figures 5.7 and 5.8.

The influence of the region selection in right ascension has not been studied extensively. The difference in the zenith angle distribution for different right ascensions has to be studied for different declinations separately. Because the right ascension selection has already been shown to have some influence, not all possible background region centers are used but only three to each side, which gives a spread in right ascension between 160° and 250°. In this range the exposure which can be seen in figure 5.6 changes almost linearly. The selection is not based on hard facts, because it does not quantitatively take the zenith angle distribution into account.

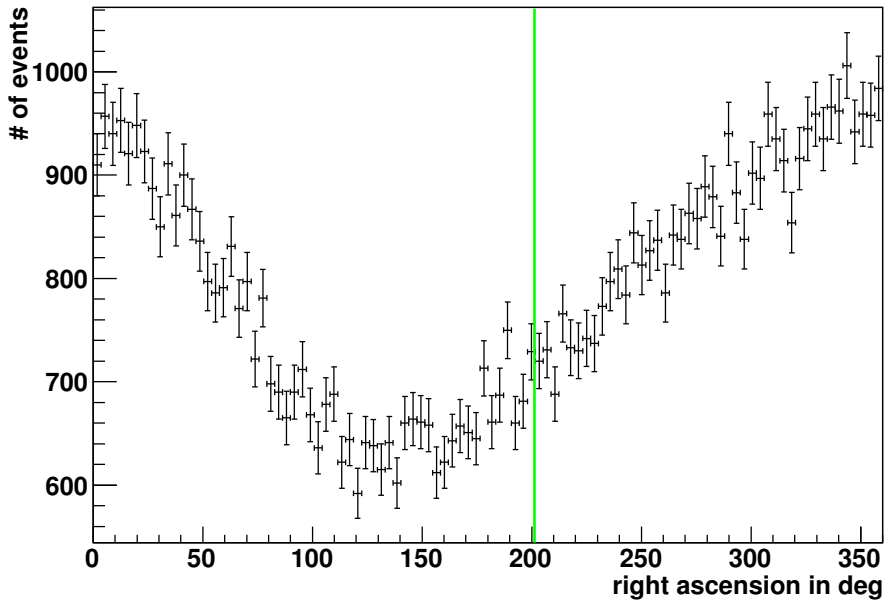

Figure 5.6.: Right ascension dependence of event counts in the Auger all-sky data sample after quality cuts. The right ascension of Centaurus A is marked with a green line.
0°: begin of southern spring; 90°: southern summer; 180°: southern autumn; 270°: southern winter
There is a clear abundance of events for sky regions which have their upper culmination at midnight in the summer months. This is likely to be caused by a combination of uptime differences in summer/winter and atmospheric influence (clouds and aerosol density).

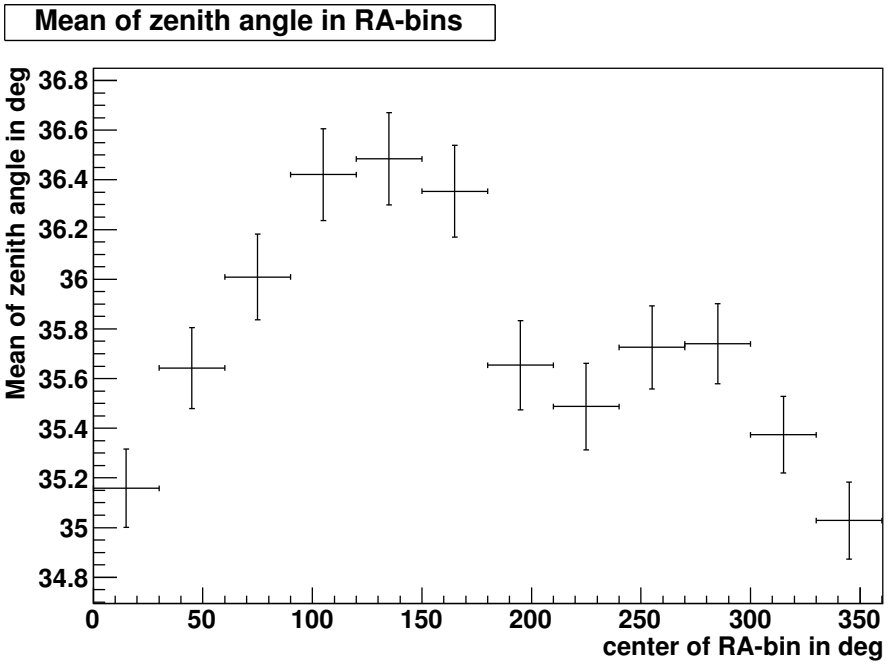

Figure 5.7.: Mean of zenith angles in right ascension bins of 30°. All available Auger data after quality cuts is used.
Generally, there seems to be a higher mean zenith angle in the events of the summer sky than of the winter sky

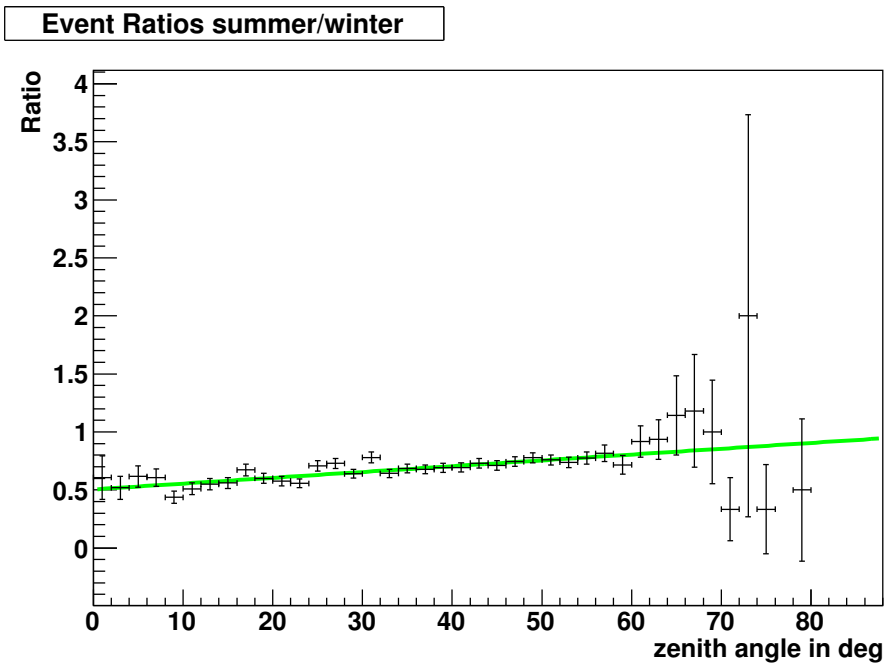

Figure 5.8.: Ratio of event counts in zenith angle bins between summer (right ascension 120°–180°) and winter (right ascension 330°–30°).
The fitted linear function is just an eye guide. There seemingly is a lower fraction of low zenith angle events in summer than in winter.

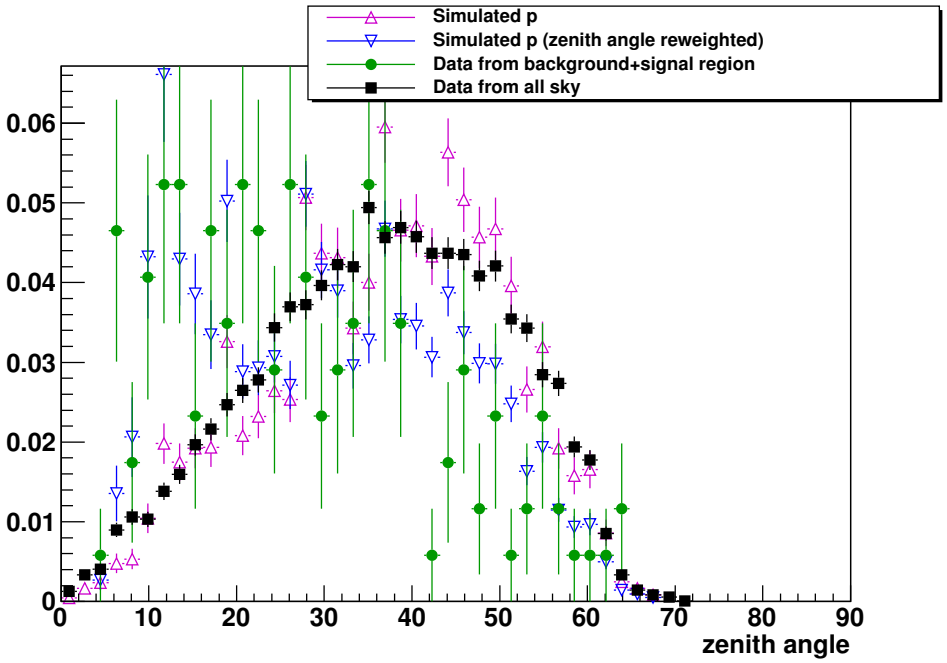

Figure 5.9.: Comparison of the Auger all-sky data (black ■) and data (green ●) from background and signal region with standard CORSIKA proton simulations (purple △) and reweighted proton simulations (blue ▽). The reconstructed energy is between 10^{18} eV and $10^{18.25}$ eV.
The zenith angle distribution for standard CORSIKA proton simulations (purple △) follows the distribution for all-sky data (black ■). To match the zenith angle distribution of events from the signal- and background-regions (green ●), the simulated events were reweighted with the weighting factor given in figure 5.11 (→blue ▽).

5.5. Correction of the simulated zenith angle distribution

For different declinations the zenith angle distribution differs. This has already been shown in section 5.4.2. More specifically, the zenith angle distribution of the events from the signal- or background-regions differs from the distribution of the all-sky data. The CORSIKA events are simulated with a zenith angle distribution as expected for all-sky events (see figure 5.9). To get a usable data set of simulated showers, comparable to the real data events from the signal- or background-regions, the all-sky simulations have to be reweighted for the different zenith angle distributions.

To determine the weighting factor, a toy-Monte-Carlo simulation is done. Events are isotropically diced over the sky in equatorial coordinates (declination and right ascension). For this, uniform distributions are used for right ascension ($\lambda \in [0, 360°)$) and the cosine of the declination ($\cos\delta \in [0, 1]$). Only events with directions inside the signal region are taken (the rest is discarded). This gives a declination distribution like for the signal data set. The corresponding zenith angle distribution is obtained by a transformation to horizontal coordinates (azimuth and altitude) for a place in the detector array (the method `ln_get_hrz_from_equ` from libnova[8] in used).

A single point in equatorial coordinates is transformed to different horizontal coordinates for different points in time, depending on the hour angle at that time. To account for

[8] `http://libnova.sourceforge.net/`

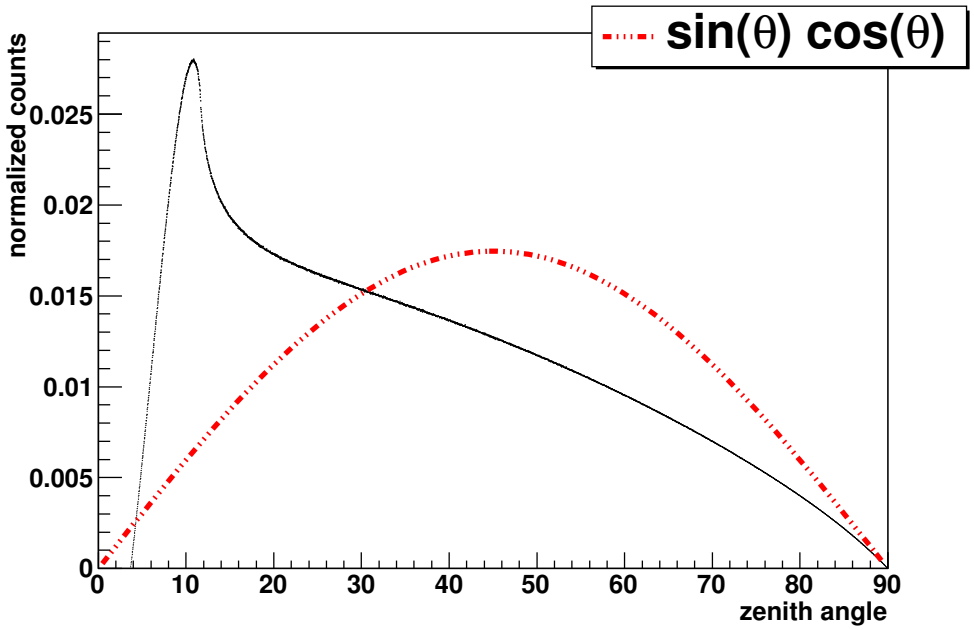

Figure 5.10.: Results of the toy MC (black histogram) with a declination distribution as in the signal region and completely random hour angle. The histogram is weighted with $\cos\theta$. $\sin\theta{\cdot}\cos\theta$ is shown with the dotted line as comparison.

that, the right ascension is replaced by a uniformly distributed random value. The coordinate conversion is then done for a fixed point in time. This gives a uniformly distributed hour angle, as is expected for a uniform uptime. That would not necessarily be the case if a random – solar – time was taken in a time interval that is not an integer multiple of whole sidereal days. The point in time for which the conversion is done is arbitrarily chosen as 0 JD[9].

Afterwards the zenith angles θ are filled into a histogram with a weighting factor of $\cos\theta$ (to account for the projection of the surface detector area onto the shower axis) and can be compared to the all-sky expectance of $\sin\theta\cos\theta$ (which is used by CORSIKA); see figure 5.10. When the zenith angles are weighted with a factor of $1/\sin\theta$, this gives the quotient of the first histogram and the all-sky expectance, which can be used as the reweighting factor to convert all-sky simulations to simulations for the Centaurus A events; see figure 5.11. With this reweighting factor the zenith angle distribution for events from Centaurus A can be reproduced by simulated proton showers (see figure 5.12). The simulated photon showers still show a different zenith angle distribution due to the suppression of low zenith angle showers because of the "$X_{\max}$ in FoV"-cut[10]. The histograms of the comparison of the (reweighted) simulations with the data for the other energy bins can be found in appendix B.2.

The performance of the toy MC to determine the reweighting factor can be improved by reducing the fraction of discarded "events". Arrival directions distributed over the whole sky are diced, although only directions in a very small sky region are not discarded. The first step is to limit the diced range of $\cos\delta$ to $[\cos(\delta_{\text{source}}+r),\ \cos(\delta_{\text{source}}-r)]$, where r is the radius of the signal region (4°) and δ_{source} is the declination of the source candidate (Centaurus A in this case). All directions with declinations outside this

[9] Julian Date
[10] Field of View

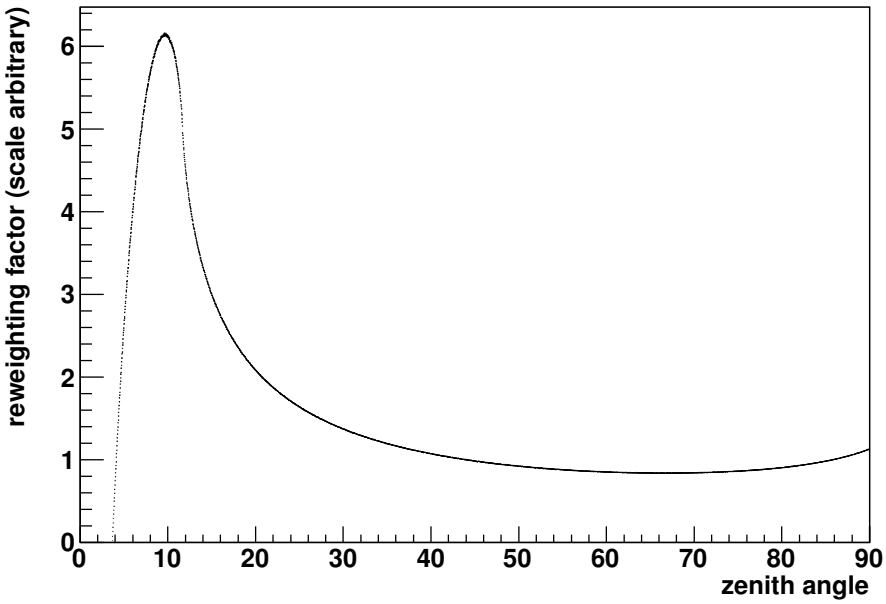

Figure 5.11.: The weighting factor needed to reweight all-sky simulations for the zenith angle distribution from Centaurus A. It is the quotient of the black and red curve in figure 5.10.

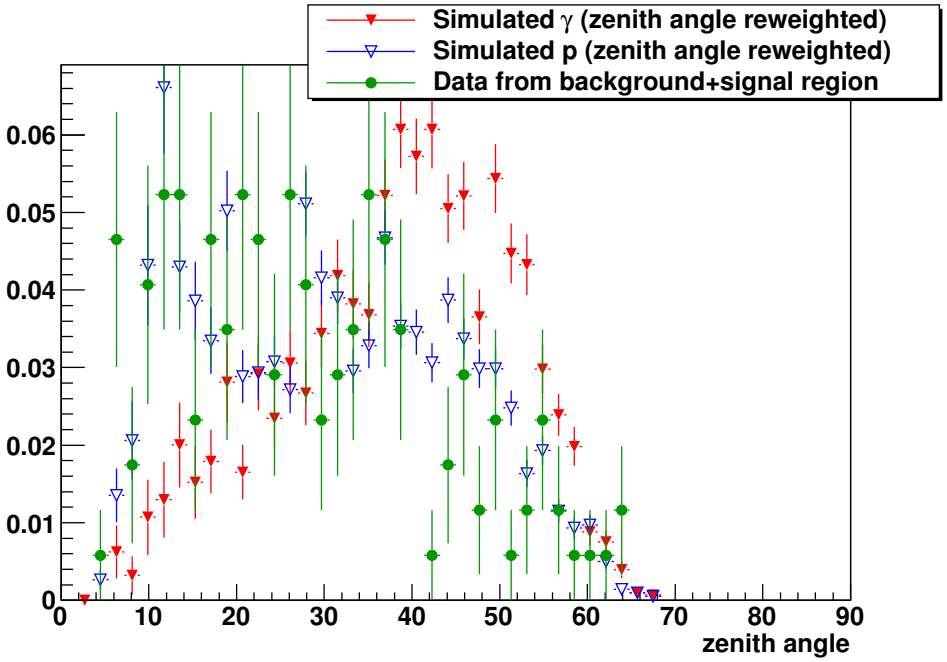

Figure 5.12.: Comparison of the data (green ●) from background and signal region with reweighted proton- (blue ▽) and photon-simulations (red ▼). The reconstructed energy is between 10^{18} eV and $10^{18.25}$ eV.
The proton simulations show a good agreement with the data. The simulated photon showers have a significant suppression of low zenith angles because these showers do reach the ground before reaching the maximum of shower development and do not survive the "$X_{\max}$ in FoV"-cut.

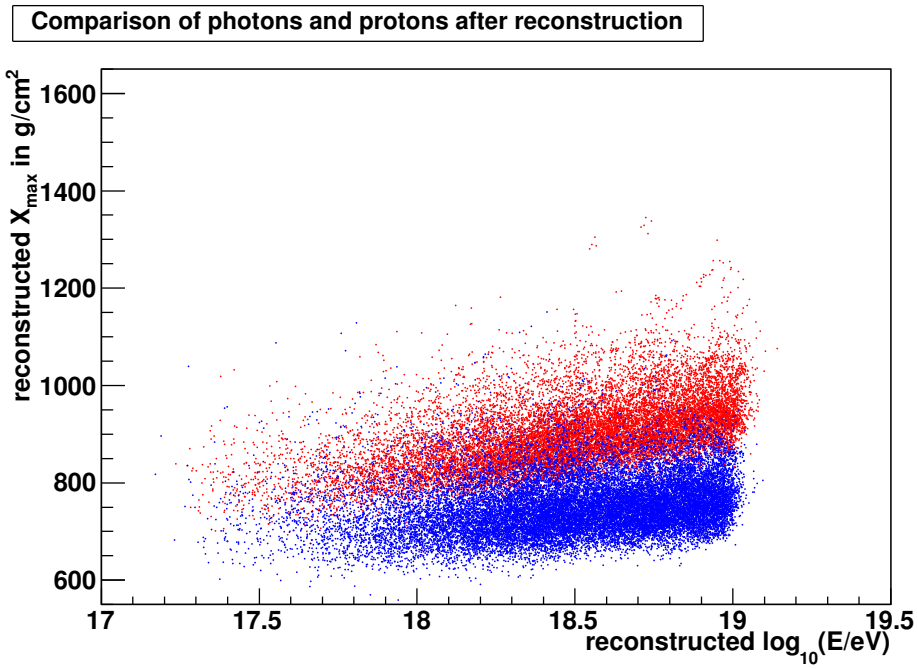

Figure 5.13.: Reconstructed $X_{\max}$ for simulated photons and protons over the reconstructed energy. All reconstructed (all-sky) events after quality cuts are used. No reweighting of the events for zenith angle or spectral index has been done. Even with the shift of the reconstructed energy of the photon induced showers, both primaries can still be distinguished.

range would be discarded anyway. The second step is to limit the interval of right ascension. For this the right ascension of the source candidate is set to 180° first, which prevents problems with the boundary at 360°. This does not change the zenith angle distribution as it should (in the simplified model of constant uptime) not depend on right ascension. The right ascension of the event is randomized anyway after the event is taken. Then the range of right ascension λ is limited to $[180° - \lambda_d, 180° + \lambda_d]$ with $\lambda_d = r/\min(\cos(\delta_{\text{source}} + r), \cos(\delta_{\text{source}} - r))$, which is the maximum right ascension difference a distance of r can have at the biggest or smallest possible declination of the circular sky region. This is a safe limitation of the range of λ which contains the complete circular region. It could be shrunk even smaller but the remaining performance improvement is not worth the additional effort of calculation.

5.6. Photon energy scale correction

The mean of the reconstructed energy is shifted to higher energies for photon induced showers, compared to the true energy, because of incorrect missing energy correction (see chapter 4.1.1 for explanation). This is not the case for proton primaries, for which the missing energy correction is optimized. Even after the incorrect missing energy correction for photon induced air showers, they can still be discriminated from proton induced air showers (see figure 5.13).

The shift in reconstructed energy has to be corrected for. Generally, two possibilities exist. The first one is to shift the energies of the reconstructed showers to get the correct mean shower energy. The second one is to shift all borders of energy bins in the opposite direction. As long as the energy is used only for the classification into energy

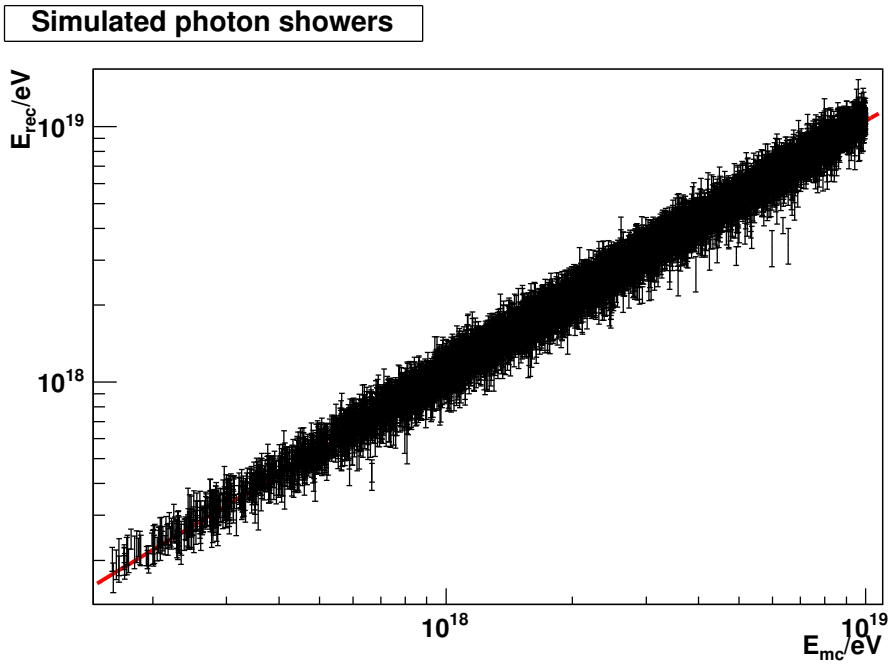

Figure 5.14.: Fit of the calibration function for energy scale correction.

bins, both possibilities would produce the same results. All events would end up in the same energy bins, because the relative energy shift between the events and the bin borders is identical for both methods. Because the method is more straight forward, the event energies are shifted and not the bin borders.

To get information about photons (like a limit on the photon count), the shifted event energies are used. To get information about hadrons, the unshifted energies are used. To get information about hadrons and photons at the same time in the same energy bin from the same events (like the total event number in an energy bin), there is no obvious way to do it right, because some of the events would have to be shifted and some would have to be not shifted with no way to identify the right correction for the specific events.

To do the energy shift, a calibration function is fitted through all the data points of the simulated photon showers using a χ^2 minimization. The reconstructed energy E_{rec} from Offline is plotted against the true energy E_{mc} which is used by CORSIKA. A function

$$E_{\mathrm{rec}} = b \cdot (E_{\mathrm{mc}})^a$$

is chosen, this corresponds to a linear function

$$\log(E_{\mathrm{rec}}) = a \cdot \log(E_{\mathrm{mc}}) + \log b$$

in log-log coordinates which are used in the analysis. The parameters a and b have no physical interpretations but are just arbitrary fit parameters. The uncertainties on the reconstructed energy is determined by Offline while fitting the Gaisser-Hillas-profile. The fitted function and the data points are shown in figure 5.14. The best parameters are $a = 0.9890 \pm 0.0006$ and $b = 1.70 \pm 0.04$. The χ^2/N_{dof} is 1.14, which means the (more or less arbitrarily chosen) form of the calibration function seems reasonable. There is no visible deviation of the calibration function from the data at the low or high end of the data range.

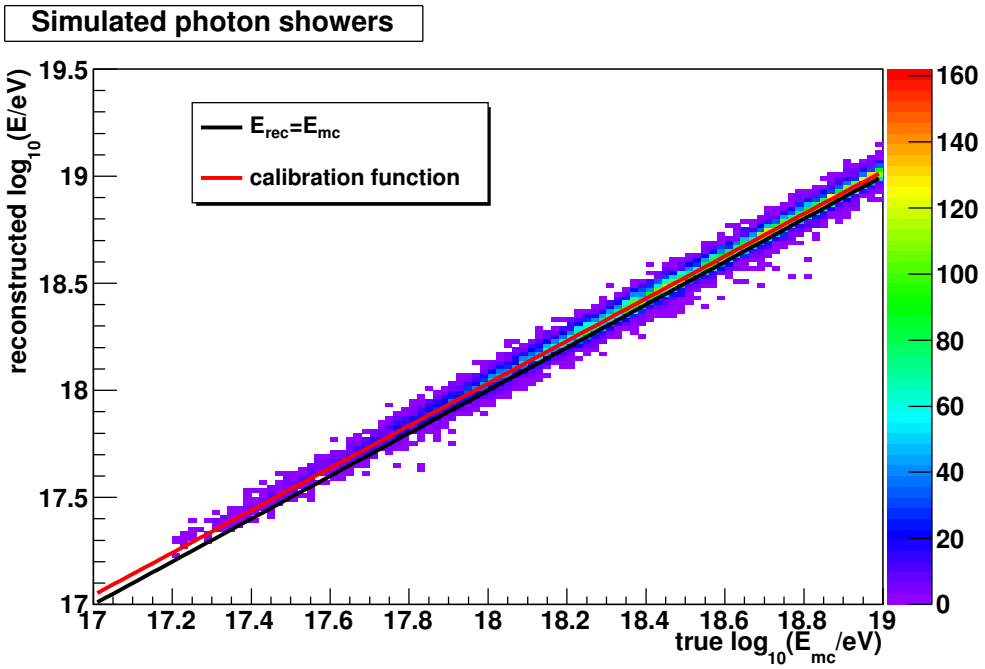

Figure 5.15.: Energy shift of photon induced air showers, with linear calibration function (red).

5.7. Photon candidate discrimination through $X_{\max}$-Cuts

For this analysis the hadronic composition of the events in the signal and the background regions has to be checked. To compare only the hadronic composition, a cut on $X_{\max}$ can be introduced to suppress possible photon events. The cut divides into a "low $X_{\max}$ range" below the cut and a "high $X_{\max}$ range" above the cut. The cut is chosen in every energy bin such that only a very small fraction of photon events is located below the cut value. Taking into account that the overall photon fraction is already known to be very small and that the majority of the hadronic events are located below the cut value, the event sample of the low $X_{\max}$ range is virtually photon-free. At the same time, if there are any photons in the sample, they should be nearly completely located in the high $X_{\max}$ range.

To get the cut values, CORSIKA shower simulations with detector simulation and event reconstruction through Offline are used. The simulated events are reweighted for a spectral index of the energy of $\gamma = 3$. From the CORSIKA simulations the events are already distributed with $\gamma = 1$, which means an additional weighting with $(E_{\mathrm{mc}})^{-2}$ has to be done. This reweighting is done through weights while filling the histograms. Another (multiplicative) weighting factor has to be used to obtain the zenith angle distribution from Centaurus A (as seen in section 5.5, figure 5.11). For the reweighting, the "true" directions and energies of the simulated events are used and not the reconstructed quantities. The cut values are determined with the photon missing energy correction applied (see section 5.6).

The determined $X_{\max}$ cut values are shown in figure 5.16 and table 5.2. For each energy bin, the cut value is chosen to be the 5% quantile of the $X_{\max}$ distribution of the simulated photon induced air showers in one energy bin. Therefore, the photon efficiency ε_γ of the cut for the high $X_{\max}$ range is $\varepsilon_\gamma = 0.95$. The small difference of ε_γ from 0.95 due to limited statistics in the simulations and the statistical uncertainty in

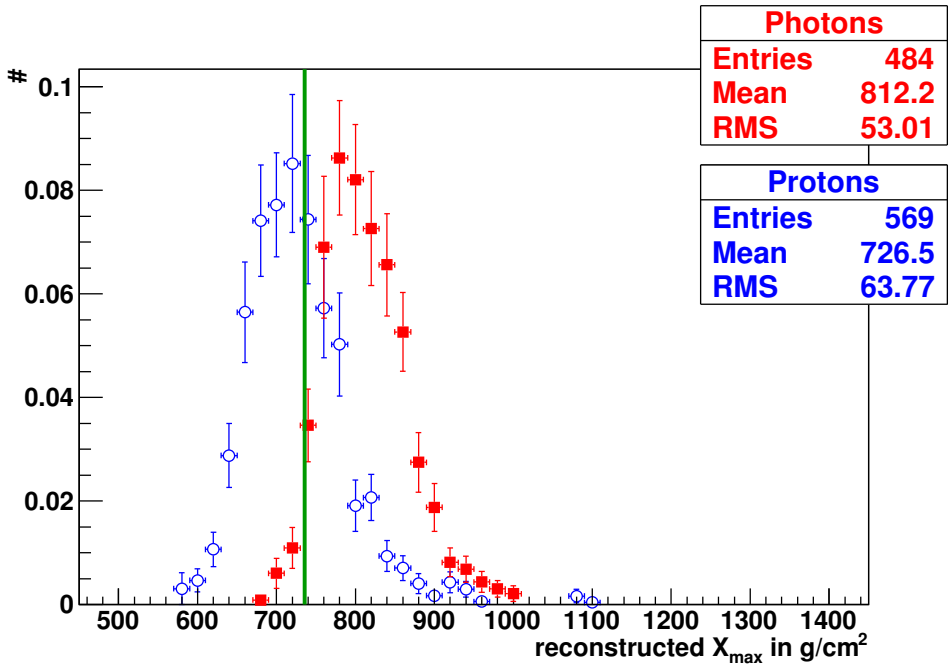

(5.16.a) Corrected photon energy $10^{17.5}$–$10^{17.75}$ eV

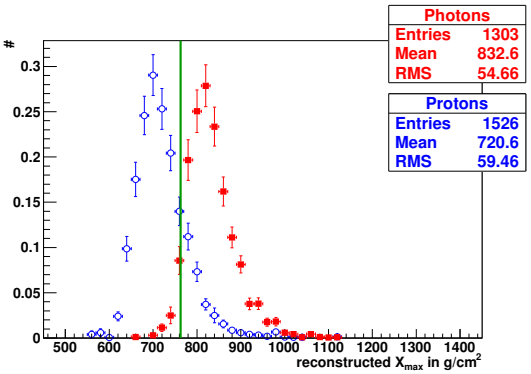

(5.16.b) Photon energy $10^{17.75}$–10^{18} eV

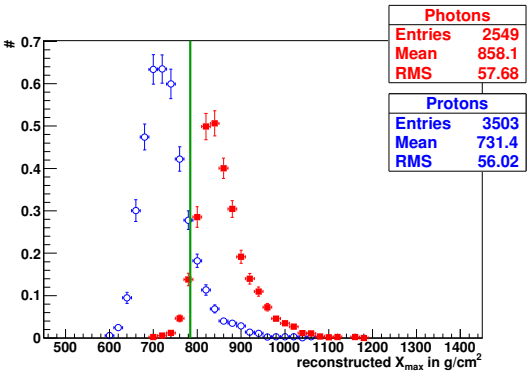

(5.16.c) Photon energy 10^{18}–$10^{18.25}$ eV

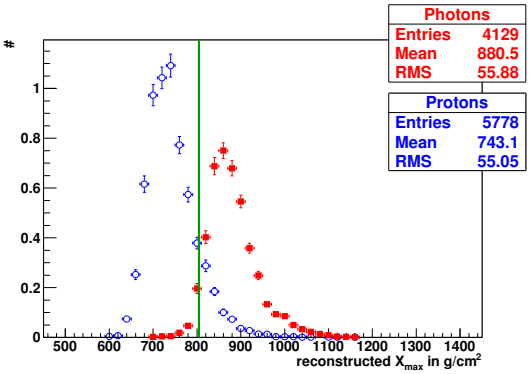

(5.16.d) Photon energy $10^{18.25}$–$10^{18.5}$ eV

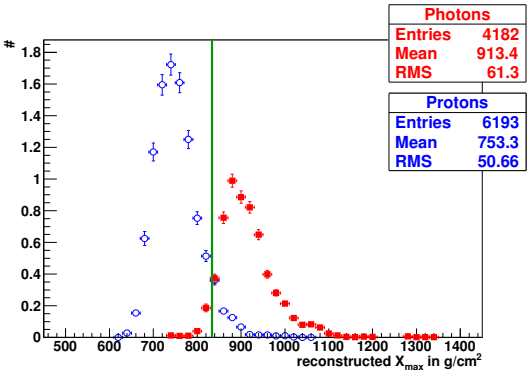

(5.16.e) Photon energy $10^{18.5}$–$10^{18.75}$ eV

Figure 5.16.: $X_{\max}$ cut values to discriminate photon induced showers. Simulated photon showers are printed in red ■, simulated proton showers are shown in blue ○ as comparison. The missing energy correction for photons is used. The cut value (vertical green line) is the 5% quantile of the $X_{\max}$ distribution of the photon induced showers.

Energy (eV)	$10^{17.5}$–$10^{17.75}$	$10^{17.75}$–10^{18}	10^{18}–$10^{18.25}$	$10^{18.25}$–$10^{18.5}$	$10^{18.5}$–$10^{18.75}$
cut ($\mathrm{g\,cm^{-2}}$)	736	763	784	805	834
proton efficiency ε_p	0.614±0.025	0.806±0.012	0.855±0.007	0.872±0.005	0.930±0.004
photon efficiency ε_γ	0.952±0.011	0.953±0.008	0.951±0.005	0.950±0.005	0.951±0.004

Table 5.2.: $X_{\max}$ cut values used to discriminate photon induced air showers. 5% quantile of photon induced air shower simulations in energy bin. The proton efficiency ε_p is the fraction of simulated proton showers *below* the cut value. The photon efficiency ε_γ is the fraction of simulated photon showers *above* the cut value and is chosen to be $\approx 95\,\%$.

the order of 1 % is ignored for the later analysis. It is negligible, compared to the other uncertainties involved. The cut value is independent of any hadron induced showers and therefore only slightly dependent on the hadronic interaction model.

For the proton simulations, the proton efficiency ε_p of the cut for the *low* $X_{\max}$ range is given in table 5.2 as comparison. It is in the order of 60% in the lowest energy bin and in the order of 90% for the highest energy bin. A higher proton efficiency means less background in the high $X_{\max}$ range. The statistical uncertainty is calculated as

$$\sigma_\varepsilon = \frac{\sqrt{\sum\limits_L w_i^2 \left(\sum\limits_H w_i\right)^2 + \sum\limits_H w_i^2 \left(\sum\limits_L w_i\right)^2}}{\left(\sum w_i\right)^2} \tag{5.11}$$

where the w_i are the weights of the single events which are summed over the low (L) and high (H) $X_{\max}$ ranges [68]. For the case of $w_i = 1$, the usual binomial uncertainty of $\sqrt{\varepsilon(1-\varepsilon)/N}$ arises (see appendix B.1.2 for the calculation).

5.8. Kolmogorov-Smirnov test in energy bins

A simple comparison (naked eye) of the $X_{\max}$ distributions in figure 5.17 does not yield any great difference between the distributions up to energies of $10^{18.75}$ eV. Because of the small sky regions, the statistics is very limited. Only up to energies of $10^{18.5}$ eV any further study is worthwhile.

The Kolmogorov-Smirnov test (often called only Kolmogorov test) [66, 11.4.2] can be used to quantitatively compare the $X_{\max}$ distributions between the signal and background data sets. Originally, the test is defined for unbinned data, so the test is run on the events with no binning in $X_{\max}$. Because of the low statistics, the test is not separately run on the events in the high $X_{\max}$ range, but only on the whole distribution, and on the events in the low $X_{\max}$ range.

The p-value of the Kolmogorov-Smirnov-Test is called KS-probability. It is the probability that two random realizations of the same distributions with the given event numbers have a greater difference in their shape. It is assumed that both distributions are indeed originating from the same (hidden) original distribution. Therefore, a high p-value corresponds to a good agreement of the distributions and a low p-value (usually the threshold is chosen to be 5%) corresponds to a bad agreement. Consequently, a low p-value suggests that both distributions are not realizations of the same mother distribution.

In figure 5.18 the KS-probabilities are shown for the compared distributions. The tests

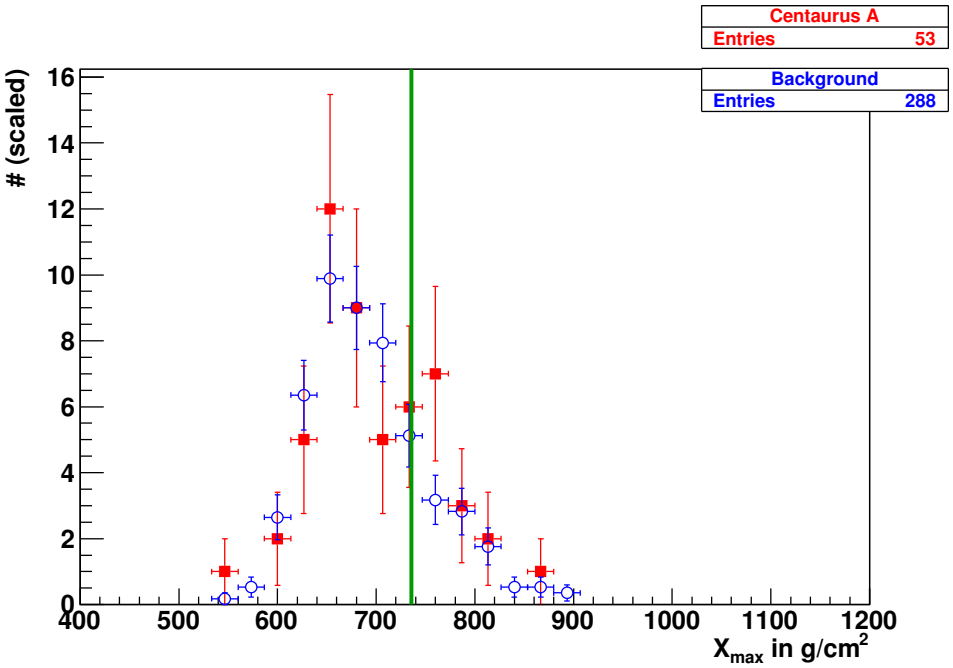

(5.17.a) True photon energy $10^{17.5}$-$10^{17.75}$ eV

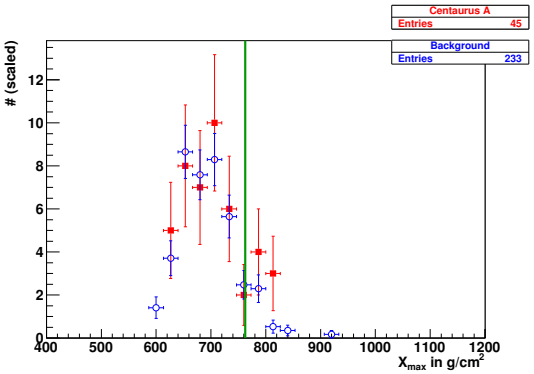

(5.17.b) True photon energy $10^{17.75}$-10^{18} eV

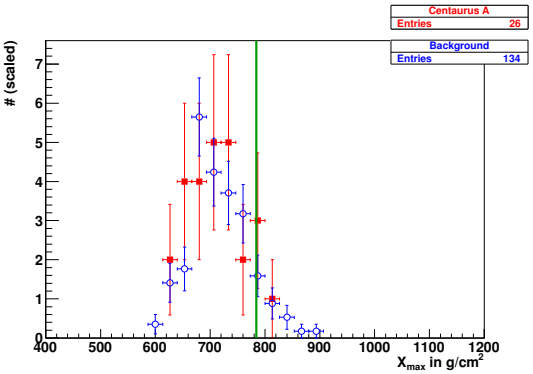

(5.17.c) True photon energy 10^{18}-$10^{18.25}$ eV

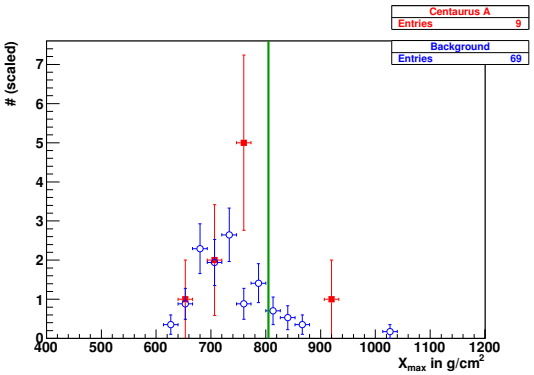

(5.17.d) True photon energy $10^{18.25}$-$10^{18.5}$ eV

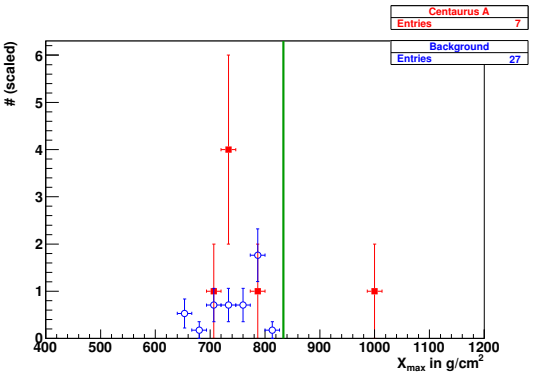

(5.17.e) True photon energy $10^{18.5}$-$10^{18.75}$ eV

Figure 5.17.: Comparison of the $X_{\max}$ distribution of the events from the signal region (■) and background region (○). The missing energy correction for photons is used. The vertical lines are the $X_{\max}$ cut values (section 5.7). The background histograms are scaled down to have the same integral in the low $X_{\max}$ range (left of cut value).

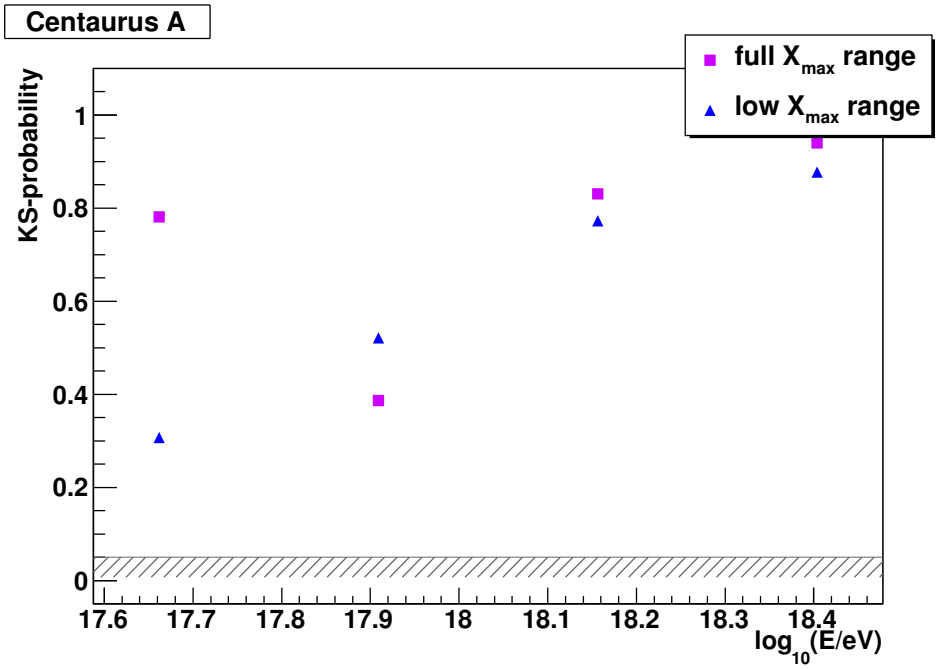

Figure 5.18.: Kolmogorov-Smirnov probabilities for the comparison of the $X_{\max}$ distributions in background- and signal-regions. The comparison is done for the whole $X_{\max}$ range and the low $X_{\max}$ range separately. The shaded area highlights probabilities below 5 %. All probabilities are above 5 %, which means the distributions appear to be compatible. Each energy bin has to be compared separately.
From this it can be concluded that the hadronic composition can not be distinguished in signal- and background-regions.

are performed using the `TMath:KolmogorovTest` routine of ROOT[11]. With all probabilities above 30% it can be concluded that the hadronic composition is identical in signal- and background-regions. With this prerequisite for the photon search fulfilled[12], now one can try to quantify (or set limits on) the photon count and the photon fraction in the observed events.

With enough statistics one could try to use the KS-test in the high $X_{\max}$ range to identify photons, and admix simulated photon showers to the data to set a limit on the photon number. Due to low statistics a different approach is chosen.

5.9. Significance of counting experiments with uptime estimation

It is often a problem to estimate the significance of positive or negative fluctuations in counting experiments, where N_{on} events have been counted in the direction of a source candidate and N_{off} events have been counted in a background region. An approach to this problem is given in [69]. The situation can be realized through pointing a photon detector in γ-ray astronomy to two different regions of the sky – this example is chosen in [69] – or, as is the case here, through selecting the arrival direction of events collected with a detector that covers a larger solid angle and has directional resolution sufficient to distinguish events from the source or background directions. Both arrival directions do not necessarily have the same exposure. This can be caused by different time spans of pointing to source or background (t_{on} and t_{off}), by different sizes of the solid angles associated with source and background regions and different geometrical exposure in both directions for a detector measuring both regions at once. In [69] the ratio $\alpha = t_{\text{on}}/t_{\text{off}}$ of the exposures is known with negligible uncertainty. This does not necessarily have to be the case. Sometimes only an estimator for α is known as the ratio $n_{\text{on}}/n_{\text{off}}$, where n_{on} and n_{off} are independent event counts that have the same exposure ratio as the important event counts N_{on} and N_{off}, but are not affected by a signal from the source candidate. This can be achieved by using different energy bands for n and N or – as in this analysis – by using some other means to exclude signal from entering n. The count in n should be statistically independent of the count in N, hence events should not be in n and N simultaneously.

An estimation for the Background $\hat{N}_B$ that is contained in N_{on} is then

$$\hat{N}_B = \alpha N_{\text{off}} \tag{5.12}$$

and the apparent number of events originating from the source is then

$$N_S = N_{\text{on}} - \hat{N}_B = N_{\text{on}} - \alpha N_{\text{off}} \tag{5.13}$$

The significance S of the observation of N_S has to be estimated, because N_S can be caused by statistical fluctuations in N_{on} and N_{off} in the absence of a real source. The N values can be assumed to follow a Poisson distribution with the average values $\langle N_{\text{on}} \rangle$ and $\langle N_{\text{off}} \rangle$.

[11] `http://root.cern.ch`
[12] A small difference in the composition might nevertheless go undetected.

5.9.1. Standard deviation of signal

The conventional approach to estimate the significance S (also given by T.-P. Li and Y.-Q. Ma in [69]) is

$$S = \frac{N_S}{\hat{\sigma}(N_S)} \tag{5.14}$$

with the simplest estimation (this first possibility is marked with 1 as lower index)

$$\sigma_1^2(N_S) = \sigma^2(N_{\text{on}}) + \sigma^2(\alpha N_{\text{off}}) \tag{5.15}$$

In the simple case of [69] equation 5.15 can be expanded as

$$\sigma_1^2(N_S) = \sigma^2(N_{\text{on}}) + \sigma^2(\alpha N_{\text{off}}) = \sigma^2(N_{\text{on}}) + \alpha^2\sigma^2(N_{\text{off}}) \tag{5.16}$$

with the best estimation for the standard deviation of N_S being

$$\hat{\sigma}_1(N_S) = \sqrt{\sigma^2(N_{\text{on}}) + \alpha^2\sigma^2(N_{\text{off}})} = \sqrt{N_{\text{on}} + \alpha^2 N_{\text{off}}} \tag{5.17}$$

and the significance therefore being

$$S_1 = \frac{N_S}{\hat{\sigma}_1(N_S)} = \frac{N_{\text{on}} - \alpha N_{\text{off}}}{\sqrt{N_{\text{on}} + \alpha^2 N_{\text{off}}}} \tag{5.18}$$

This formula is shown to be not very accurate, but can easily be adopted for the case of the not exactly known α, where $\sigma^2(\alpha) \neq 0$. Quantities and formulae corresponding to this are marked with a prime symbol. With $\alpha = n_{\text{on}}/n_{\text{off}}$ equation 5.15 can be expanded as

$$\begin{aligned}\sigma_1'^2(N_S) &= \sigma^2(N_{\text{on}}) + \sigma^2\left(\frac{n_{\text{on}}}{n_{\text{off}}}N_{\text{off}}\right) \\ &= \sigma^2(N_{\text{on}}) + \left(\frac{n_{\text{on}}}{n_{\text{off}}}\right)^2\sigma^2(N_{\text{off}}) + \left(\frac{N_{\text{off}}}{n_{\text{off}}}\right)^2\sigma^2(n_{\text{on}}) + \left(\frac{n_{\text{on}}}{n_{\text{off}}^2}N_{\text{off}}\right)^2\sigma^2(n_{\text{off}})\end{aligned} \tag{5.19}$$

which yields

$$\begin{aligned}\hat{\sigma}_1'(N_S) &= \sqrt{\sigma^2(N_{\text{on}}) + \left(\frac{n_{\text{on}}}{n_{\text{off}}}\right)^2\sigma^2(N_{\text{off}}) + \left(\frac{N_{\text{off}}}{n_{\text{off}}}\right)^2\sigma^2(n_{\text{on}}) + \left(\frac{n_{\text{on}}}{n_{\text{off}}^2}N_{\text{off}}\right)^2\sigma^2(n_{\text{off}})} \\ &= \sqrt{N_{\text{on}} + \left(\frac{n_{\text{on}}}{n_{\text{off}}}\right)^2 N_{\text{off}} + \left(\frac{N_{\text{off}}}{n_{\text{off}}}\right)^2 n_{\text{on}} + \left(\frac{n_{\text{on}}}{n_{\text{off}}^2}N_{\text{off}}\right)^2 n_{\text{off}}}\end{aligned} \tag{5.20}$$

and finally

$$S_1' = \frac{N_{\text{on}} - \frac{n_{\text{on}}}{n_{\text{off}}}N_{\text{off}}}{\sqrt{N_{\text{on}} + \left(\frac{n_{\text{on}}}{n_{\text{off}}}\right)^2 N_{\text{off}} + \left(\frac{N_{\text{off}}}{n_{\text{off}}}\right)^2 n_{\text{on}} + \left(\frac{n_{\text{on}}}{n_{\text{off}}^2}N_{\text{off}}\right)^2 n_{\text{off}}}} \tag{5.21}$$

An improvement of equation 5.18 is given in [69] as

$$S_2 = \frac{N_{\text{on}} - \alpha N_{\text{off}}}{\sqrt{\alpha(N_{\text{on}} + N_{\text{off}})}} \tag{5.22}$$

which can not easily be adopted for the more complicated case.

5.9.2. Likelihood ratio method

A second powerful approach used in [69] to estimate the significance is to use the maximum likelihood ratio hypothesis test. One tests the hypothesis $\langle N_S \rangle = 0$ (every apparent signal is just a fluctuation of background) against the hypothesis $\langle N_S \rangle \neq 0$ ($\langle N_S \rangle < 0$ is allowed). The observables are $X = (N_{\text{on}}, N_{\text{off}}, n_{\text{on}}, n_{\text{off}})$, the parameters of the theory are $\Theta = (\langle N_S \rangle, \langle N_B \rangle, \alpha, \langle n_{\text{off}} \rangle)$ which directly maps to $\Theta' = (\langle N_{\text{on}} \rangle, \langle N_{\text{off}} \rangle, \langle n_{\text{on}} \rangle, \langle n_{\text{off}} \rangle)$.

The likelihood function is simply the product of four Poisson probabilities:

$$L(X|\Theta) = P(N_{\text{on}}|\langle N_{\text{on}} \rangle) \cdot P(N_{\text{off}}|\langle N_{\text{off}} \rangle) \cdot P(n_{\text{on}}|\langle n_{\text{on}} \rangle) \cdot P(n_{\text{off}}|\langle n_{\text{off}} \rangle) \tag{5.23}$$

with

$$P(N|\lambda) = \frac{\lambda^N}{N!} \mathrm{e}^{-\lambda} \tag{5.24}$$

The likelihood ratio to test (or reject) the null-hypothesis is

$$\lambda = \frac{L\left(X|\hat{\Theta}_c\right)}{L\left(X|\hat{\Theta}\right)} = \frac{L\left(X|\langle N_S \rangle = 0, \left\langle \hat{N}_B \right\rangle_c, \hat{\alpha}_c, \langle \hat{n}_{\text{off}} \rangle_c\right)}{L\left(X|\left\langle \hat{N}_S \right\rangle, \left\langle \hat{N}_B \right\rangle, \hat{\alpha}, \langle \hat{n}_{\text{off}} \rangle\right)} \tag{5.25}$$

Here $\hat{\Theta}\left(\left\langle \hat{N}_S \right\rangle, \left\langle \hat{N}_B \right\rangle, \hat{\alpha}, \langle \hat{n}_{\text{off}} \rangle\right)$ is the set of parameters that maximizes L for the observed X and $\hat{\Theta}_c\left(\langle N_S \rangle = 0, \left\langle \hat{N}_B \right\rangle_c, \hat{\alpha}_c, \langle \hat{n}_{\text{off}} \rangle_c\right)$ is the set of parameters that maximizes L under the condition that $\langle N_S \rangle = 0$

If the null-hypothesis is true, for only one fixed parameter ($\langle N_S \rangle = 0$) in the null-hypothesis the quantity $-2 \ln \lambda$ will asymptotically follow a χ^2 distribution with one degree of freedom [69]:

$$-2 \ln \lambda \sim \chi^2(1) \tag{5.26}$$

The sum of k independent standard normal random variables follows a χ^2-distribution with k degrees of freedom [67, 16.2.4.6.1]. This means that the square of one standard normal variable is distributed as $\chi^2(1)$. In the inverse, the square root of a $\chi^2(1)$ distributed random variable follows a (half) standard normal distribution. Consequential, one can conclude that the quantity

$$S_3 = \sqrt{-2 \ln \lambda} \tag{5.27}$$

follows a standard normal distribution if the null-hypothesis is true. That means S_3 can indeed be interpreted as a significance in the traditional sense.

For the general case it is obvious that

$$\left\langle \hat{N}_S \right\rangle = N_{\text{on}} - \hat{\alpha} N_{\text{off}} \tag{5.28a}$$

$$\left\langle \hat{N}_B \right\rangle = \hat{\alpha} N_{\text{off}} \tag{5.28b}$$

$$\hat{\alpha} = \frac{n_{\text{on}}}{n_{\text{off}}} \tag{5.28c}$$

$$\langle \hat{n}_{\text{off}} \rangle = n_{\text{off}} \tag{5.28d}$$

or

$$\left\langle \hat{N}_{\text{on}} \right\rangle = N_{\text{on}} \tag{5.29a}$$

$$\left\langle \hat{N}_{\text{off}} \right\rangle = N_{\text{off}} \tag{5.29b}$$

$$\langle \hat{n}_{\text{on}} \rangle = n_{\text{on}} \tag{5.29c}$$

$$\langle \hat{n}_{\text{off}} \rangle = n_{\text{off}} \tag{5.29d}$$

For the null-hypothesis the best estimator for the background is no longer $\langle \hat{N}_B \rangle = \hat{\alpha} N_{\text{off}}$ but one can get a better estimator by including N_{on} (all estimators under the condition of the null hypothesis are marked with c as a lower index):

$$\langle \hat{N}_{\text{on}} \rangle_c = \langle \hat{N}_B \rangle_c = \hat{\alpha}_c \frac{N_{\text{on}} + N_{\text{off}}}{1 + \hat{\alpha}_c} = \frac{\hat{\alpha}_c}{1 + \hat{\alpha}_c} (N_{\text{on}} + N_{\text{off}}) \tag{5.30a}$$

This obviously also changes $\langle \hat{N}_{\text{off}} \rangle_c$:

$$\langle \hat{N}_{\text{off}} \rangle_c = \frac{1}{\hat{\alpha}_c} \langle \hat{N}_B \rangle_c = \frac{N_{\text{on}} + N_{\text{off}}}{1 + \hat{\alpha}_c} = \frac{1}{1 + \hat{\alpha}_c} (N_{\text{on}} + N_{\text{off}}) \tag{5.30b}$$

Because, in the absence of a signal, the there is no general difference between N and n, the corresponding estimators for the n values are:

$$\langle \hat{n}_{\text{on}} \rangle_c = \frac{\hat{\alpha}_c}{1 + \hat{\alpha}_c} (n_{\text{on}} + n_{\text{off}}) \tag{5.30c}$$

$$\langle \hat{n}_{\text{off}} \rangle_c = \frac{1}{1 + \hat{\alpha}_c} (n_{\text{on}} + n_{\text{off}}) \tag{5.30d}$$

Also the estimate for α should be no longer based only on n_{on} and n_{off} but also on N_{on} and N_{off}:

$$\hat{\alpha}_c = \frac{n_{\text{on}} + N_{\text{on}}}{n_{\text{off}} + N_{\text{off}}} \tag{5.30e}$$

Using equations 5.23, 5.28 and 5.29 one gets for the general likelihood function:

$$\begin{aligned}
L\left(X|\hat{\Theta}\right) &= L\left(X|\hat{\Theta}'\right) = L\left(X|\left\langle \hat{N}_S \right\rangle, \left\langle \hat{N}_B \right\rangle, \hat{\alpha}, \langle \hat{n}_{\text{off}} \rangle\right) \\
&= P(N_{\text{on}}|\langle N_{\text{on}} \rangle = N_{\text{on}}) \cdot P(N_{\text{off}}|\langle N_{\text{off}} \rangle = N_{\text{off}}) \cdot \\
&\quad P(n_{\text{on}}|\langle n_{\text{on}} \rangle = n_{\text{on}}) \cdot P(n_{\text{off}}|\langle n_{\text{off}} \rangle = n_{\text{off}}) \\
&= \frac{N_{\text{on}}^{N_{\text{on}}}}{N_{\text{on}}!} \exp(-N_{\text{on}}) \cdot \frac{N_{\text{off}}^{N_{\text{off}}}}{N_{\text{off}}!} \exp(-N_{\text{off}}) \cdot \frac{n_{\text{on}}^{n_{\text{on}}}}{n_{\text{on}}!} \exp(-n_{\text{on}}) \cdot \frac{n_{\text{off}}^{n_{\text{off}}}}{n_{\text{off}}!} \exp(-n_{\text{off}}) \\
&= \frac{N_{\text{on}}^{N_{\text{on}}}}{N_{\text{on}}!} \frac{N_{\text{off}}^{N_{\text{off}}}}{N_{\text{off}}!} \frac{n_{\text{on}}^{n_{\text{on}}}}{n_{\text{on}}!} \frac{n_{\text{off}}^{n_{\text{off}}}}{n_{\text{off}}!} \exp\left(-(N_{\text{on}} + N_{\text{off}} + n_{\text{on}} + n_{\text{off}})\right)
\end{aligned} \tag{5.31}$$

Using equations 5.23 and 5.30 one gets for the likelihood function of the null-hypothesis:

$$\begin{aligned}
L\left(X|\hat{\Theta}_c\right) &= L\left(X|\langle N_S \rangle = 0, \left\langle \hat{N}_B \right\rangle_c, \hat{\alpha}_c, \langle \hat{n}_{\text{off}} \rangle_c\right) \\
&= P\left(N_{\text{on}}|\langle N_{\text{on}} \rangle = \frac{\hat{\alpha}_c}{1 + \hat{\alpha}_c}(N_{\text{on}} + N_{\text{off}})\right) \cdot P\left(N_{\text{off}}|\langle N_{\text{off}} \rangle = \frac{1}{1 + \hat{\alpha}_c}(N_{\text{on}} + N_{\text{off}})\right) \cdot \\
&\quad P\left(n_{\text{on}}|\langle n_{\text{on}} \rangle = \frac{\hat{\alpha}_c}{1 + \hat{\alpha}_c}(n_{\text{on}} + n_{\text{off}})\right) \cdot P\left(n_{\text{off}}|\langle n_{\text{off}} \rangle = \frac{1}{1 + \hat{\alpha}_c}(n_{\text{on}} + n_{\text{off}})\right) \\
&= \frac{\left(\frac{\hat{\alpha}_c}{1+\hat{\alpha}_c}(N_{\text{on}} + N_{\text{off}})\right)^{N_{\text{on}}}}{N_{\text{on}}!} \frac{\left(\frac{1}{1+\hat{\alpha}_c}(N_{\text{on}} + N_{\text{off}})\right)^{N_{\text{off}}}}{N_{\text{off}}!} \cdot \\
&\quad \frac{\left(\frac{\hat{\alpha}_c}{1+\hat{\alpha}_c}(n_{\text{on}} + n_{\text{off}})\right)^{n_{\text{on}}}}{n_{\text{on}}!} \frac{\left(\frac{1}{1+\hat{\alpha}_c}(n_{\text{on}} + n_{\text{off}})\right)^{n_{\text{off}}}}{n_{\text{off}}!} \cdot \\
&\quad \exp\left(-(N_{\text{on}} + N_{\text{off}} + n_{\text{on}} + n_{\text{off}})\right)
\end{aligned} \tag{5.32}$$

An additional intermediate step is given in appendix B.1.1.

Putting equations 5.31 and 5.32 into equation 5.25 one gets:

$$\lambda = \left(\frac{\hat{\alpha}_c}{1+\hat{\alpha}_c}\frac{N_{on}+N_{off}}{N_{on}}\right)^{N_{on}}\left(\frac{1}{1+\hat{\alpha}_c}\frac{N_{on}+N_{off}}{N_{off}}\right)^{N_{off}} \left(\frac{\hat{\alpha}_c}{1+\hat{\alpha}_c}\frac{n_{on}+n_{off}}{n_{on}}\right)^{n_{on}}\left(\frac{1}{1+\hat{\alpha}_c}\frac{n_{on}+n_{off}}{n_{off}}\right)^{n_{off}} \tag{5.33}$$

Finally one gets by putting equation 5.33 into equation 5.27:

$$S_3' = \sqrt{2}\left\{N_{on}\ln\left(\frac{1+\hat{\alpha}_c}{\hat{\alpha}_c}\frac{N_{on}}{N_{on}+N_{off}}\right) + N_{off}\ln\left((1+\hat{\alpha}_c)\frac{N_{off}}{N_{on}+N_{off}}\right) + n_{on}\ln\left(\frac{1+\hat{\alpha}_c}{\hat{\alpha}_c}\frac{n_{on}}{n_{on}+n_{off}}\right) + n_{off}\ln\left((1+\hat{\alpha}_c)\frac{n_{off}}{n_{on}+n_{off}}\right)\right\}^{1/2} \tag{5.34}$$

with (equation 5.30e)

$$\hat{\alpha}_c = \frac{n_{on}+N_{on}}{n_{off}+N_{off}}$$

The corresponding formula from [69] for exactly known α is:

$$S_3 = \sqrt{2}\left\{N_{on}\ln\left(\frac{1+\alpha}{\alpha}\frac{N_{on}}{N_{on}+N_{off}}\right) + N_{off}\ln\left((1+\alpha)\frac{N_{off}}{N_{on}+N_{off}}\right)\right\}^{1/2} \tag{5.35}$$

For improved usefulness the sign of S_3 and S_3' can be defined as negative for $N_S \leq 0$, so that over- and under-fluctuations can be handled separately.

5.9.3. Verification of the formulae

As already done by T.-P. Li and Y.-Q. Ma in [69], the formulae for S can be tested with a Monte Carlo simulation. Therefore, the true values of $\langle N_{off}\rangle$, α ,$\langle N_{on}\rangle = \alpha\langle N_{off}\rangle$ and also $\langle n_{off}\rangle$ and $\langle n_{on}\rangle = \alpha\langle n_{off}\rangle$ are chosen, and Poisson distributed pseudo random integers N_{on}, N_{off} and n_{on}, n_{off} for the given average values are drawn.

For the simulations $\alpha = 0.2$, $\langle N_{off}\rangle = 41$ and $\langle n_{off}\rangle = 110$ are used. The MC experiment is repeated 10^8 times.

For every sample of pseudo-random numbers the significances are calculated with the different formulae and filled into histograms. These histograms can be compared with a standard normal distribution which is scaled by the integral of the simulated distribution[13].

Alternatively, the histogram content in all bins above a given significance S can be divided by the total histogram content to get the integral frequency distribution of the significances. This can be compared to the (inverted) cumulative distribution function of the normal distribution:

$$P = 1 - \frac{1}{2}\left[1 + \mathrm{Erf}\left(\frac{S}{\sqrt{2}}\right)\right] \tag{5.36}$$

where Erf(x) is the error function.

The verification plots from [69] can be reproduced nicely (see figure 5.19). The original formulae S_1 (equation 5.18), S_2 (equation 5.22) and S_3 (equation 5.35) are not suited for the case of the not exactly known α as in this analysis (see figures 5.20 and 5.22). S_3' (equation 5.34) should be used instead (see figures 5.21 and 5.22).

[13] total count in the histogram multiplied with the bin width

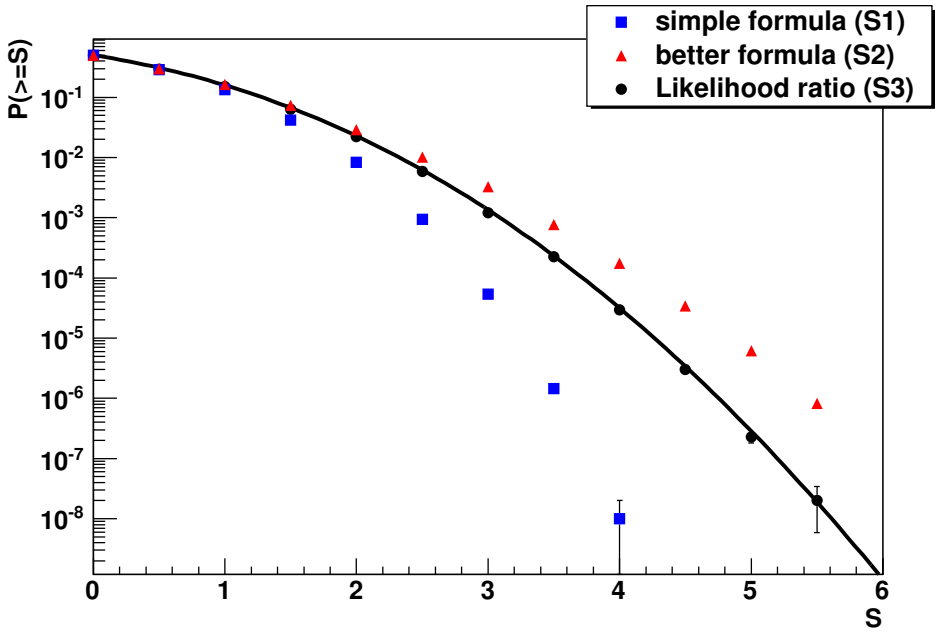

Figure 5.19.: Integral frequency distributions of the significances of the Monte Carlo samples for an exactly known α. Formulae as given in [69]. $\alpha = 0.2$, $\langle N_{\text{off}} \rangle = 41$
As expected the simplest formula S_1 (equation 5.18) has the largest deviation from the standard normal distribution. S_3 (equation 5.35), which is based on the likelihood ratio test, shows very good agreement.

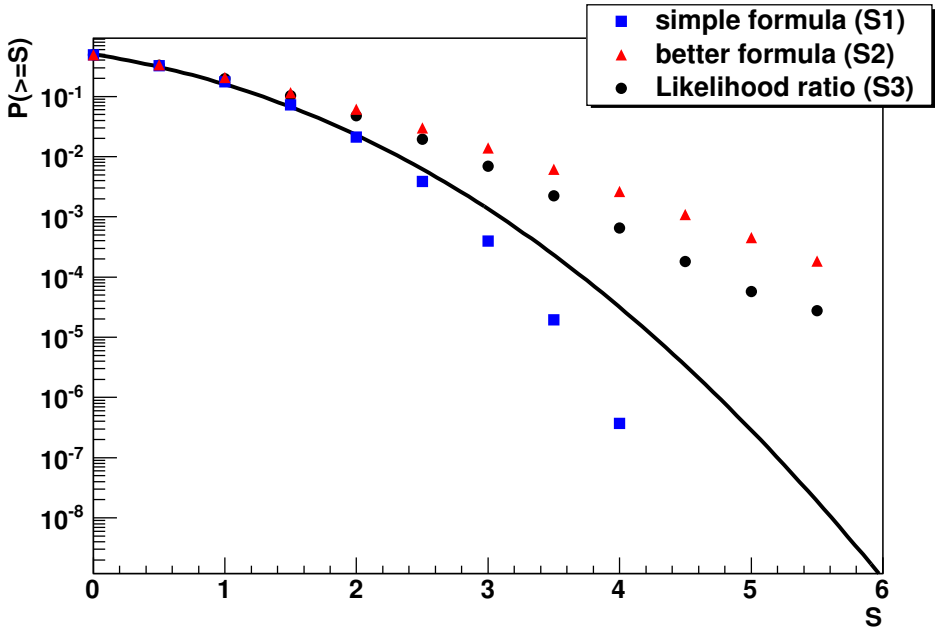

Figure 5.20.: Integral frequency distributions of the significances of the Monte Carlo samples for an estimated α. $\alpha = 0.2$, $\langle N_{\text{off}} \rangle = 41$, $\langle n_{\text{off}} \rangle = 110$
As expected the unmodified formulae S_1 (equation 5.18), S_2 (equation 5.22) and S_3 (equation 5.35) show very bad agreement with the standard normal distribution.

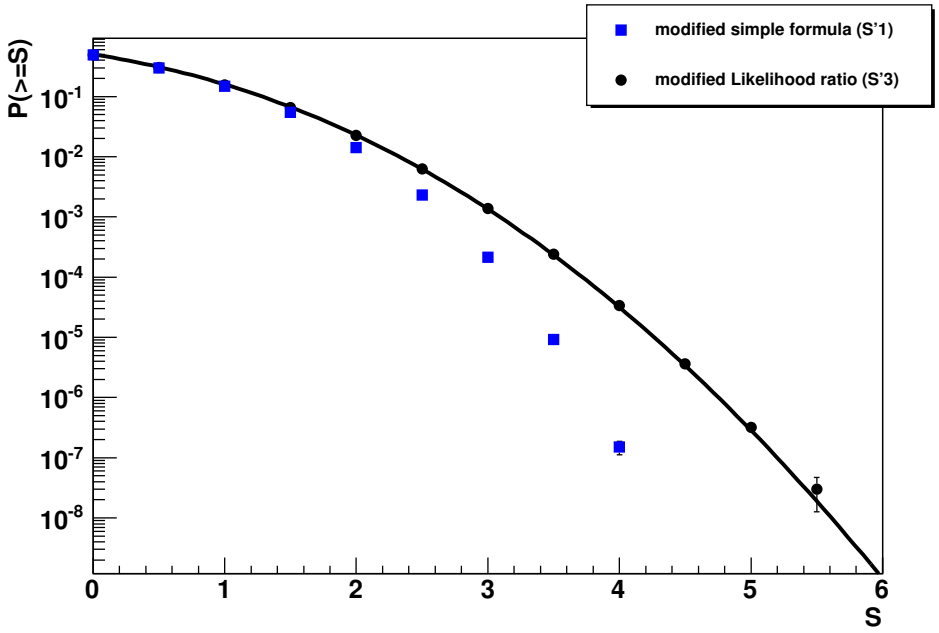

Figure 5.21.: Integral frequency distributions of the significances of the Monte Carlo samples for an estimated α with the modified set of formulae. $\alpha = 0.2$, $\langle N_{\text{off}} \rangle = 41$, $\langle n_{\text{off}} \rangle = 110$
As expected the simplest formula S_1' (equation 5.21) again shows large deviations from the standard normal distribution. S_3' (equation 5.34), which is based on the likelihood ratio test, shows very good agreement and should be used.

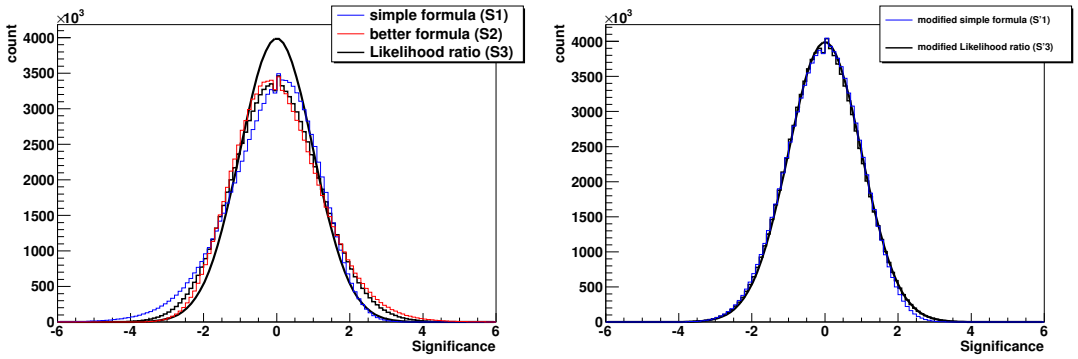

Figure 5.22.: Distributions of the significances of the Monte Carlo samples for an estimated α.
The unmodified formulae show a great difference from the standard normal distributions while the modified formulae fit much better. At $S = 0$ an artifact of the discrete nature of the count numbers can be seen. The likelihood ratio formula is only exact in the asymptotic limit of $N \to \infty$.

Computational stumbling blocks

While computing the values of S_3 or S_3' in the analysis, there are two places where problems can arise. These cases have to be handled separately in computer code.

The first problem occurs at a significance of 0, which happens if $N_{\text{on}} = \alpha \cdot N_{\text{off}}$ and $n_{\text{on}} = \alpha \cdot n_{\text{off}}$. This means all arguments of the logarithms become 1. Sometimes it can happen that $\ln(1)$ is not correctly calculated as 0 but as some small negative number $\sim -10^{-15}$, which becomes a major problem when taking the square root.

The second problem arises when one of the counts is zero. Then $0 \cdot \ln(0)$ is calculated which is undefined. The proper result should be 0 ($\lim_{x \to 0+} x \cdot \ln(x) = 0$).

5.10. Determination of the number of photon candidate events

To identify an excess of photon induced showers in the events from the signal region, simply the counts in the high X_{max} ranges are compared between signal and background region. The missing energy correction for photons is applied to all events (see section 5.6). The counts are named N_{HS} (high, signal) and N_{HB} (high, background). The scaling factor α which is necessary for the background region has to be estimated. The ratio of the event counts in the low X_{max} range, which should be uninfluenced from photon induced showers, can be used for this. The involved counts are named N_{LS} (low, signal) and N_{LB} (low, background).

$$\alpha = \frac{N_{LS}}{N_{LB}} \tag{5.37}$$

The apparent photon count N_γ is the excess of N_{HS} over the background-expectation:

$$N_\gamma = N_{HS} - \alpha N_{HB} \tag{5.38}$$

The numbers are given in table 5.3 and shown in figure 5.23.

energy interval	counts				scaling	apparent
(eV)	N_{HS}	N_{HB}	N_{LS}	N_{LB}	α	N_γ
$10^{17.5}$ –$10^{17.75}$	16	56	37	232	0.16	7.1
$10^{17.75}$–10^{18}	8	23	37	210	0.18	3.9
10^{18} –$10^{18.25}$	3	16	23	118	0.19	-0.1
$10^{18.25}$–$10^{18.5}$	1	10	8	59	0.14	-0.4

Table 5.3.: Event counts in the analyzed energy bins, divided by the X_{max} cuts. Also the scaling factor for the background expectation and the apparent photon count N_γ is given.

5.10.1. Significance

It is not trivial to estimate the significance of over- or under-fluctuations of the photon candidate count in signal and background regions. As shown in section 5.9 a likelihood ratio approach can be used.

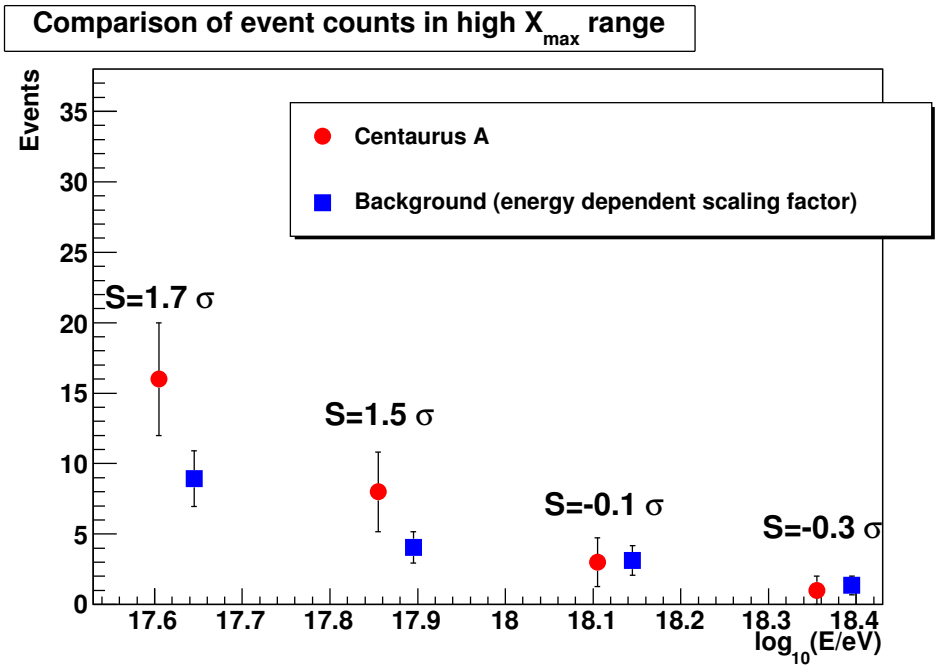

Figure 5.23.: Event counts in the high $X_{\max}$ range with the significances of the deviations. $S > 0$ means over-fluctuation, $S < 0$ means under-fluctuation. The over-fluctuations in the lowest energy bins can still happen by chance.

For this in equation 5.34 the substitutions $N_{\text{on}} = N_{HS}$, $N_{\text{off}} = N_{HB}$, $n_{\text{on}} = N_{LS}$ and $n_{\text{off}} = N_{LB}$ have to be done. The significances are shown in figure 5.23.

The significances are 1.7 and 1.5 for the two lowest energy bins and nearly zero for the two highest energy bins. This means, no excess of photons from Centaurus A is found.

5.11. Limits on the photon count at ultra-high energies from Centaurus A

The significance formula is now used again to set limits on the photon count at 95% confidence level. The limit at 95%CL is the average photon count in the signal region which gives a higher significance than observed in 95% of all cases when it is added to the background expectation. This accounts for the fact that the observed count can be an under-fluctuation with the true average being higher.

To calculate the limit a toy-MC is done. New values for N_{HS}, N_{HB}, N_{LS} and N_{LB} are chosen pseudo-randomly from a Poisson distribution. The means of the Poisson distributions are chosen to be

$$\langle N_{LS} \rangle = N_{LS} \tag{5.39}$$
$$\langle N_{LB} \rangle = N_{LB} \tag{5.40}$$
$$\langle N_{HB} \rangle = N_{HB} \tag{5.41}$$
$$\langle N_{HS} \rangle = \frac{N_{LS}}{N_{LB}} N_{HB} + \langle N_P \rangle \tag{5.42}$$

where $\langle N_P \rangle$ is the mean number of photons added to the high $X_{\max}$ range. For each set of these new random counts the significance is calculated and $\langle N_P \rangle$ is chosen such that

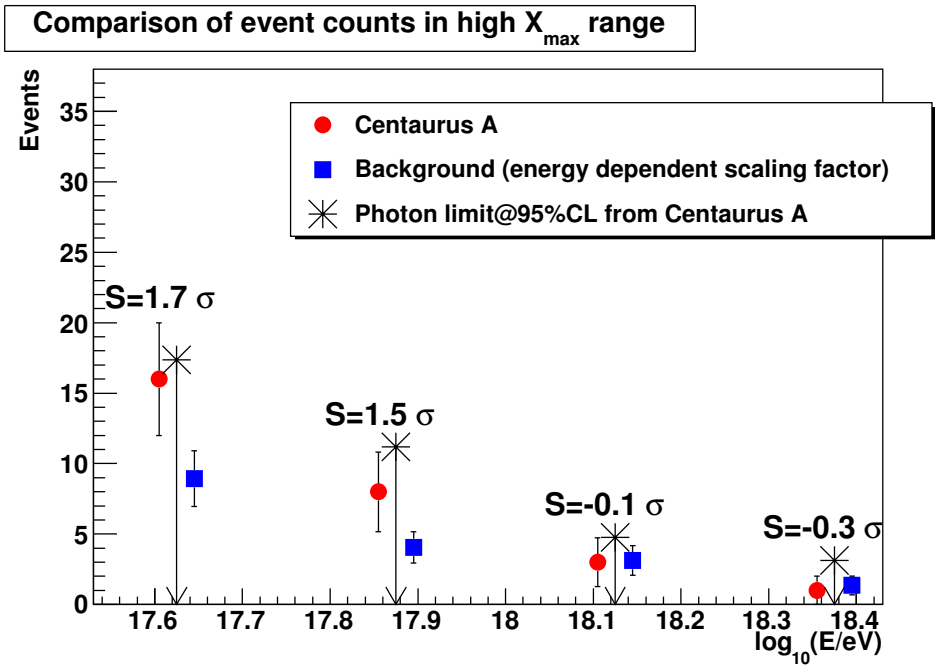

Figure 5.24.: Upper limits on photon count at 95% confidence level. As comparison, the event counts in the high $X_{\max}$ range from the Centaurus A region and the background region (scaled down) are shown with the significances of the deviations.

the significance is higher than the observed significance in 95% of all cases[14]. Because of the photon efficiency of the cut, only $\varepsilon_\gamma = 95\,\%$ of the photons are expected to be above the $X_{\max}$ cut value. The chosen $\langle N_P \rangle$ is divided by $\varepsilon_\gamma = 0.95$ to get the limit on the overall photon count:

$$N_{\gamma,95\%} = \frac{\langle N_P \rangle}{\varepsilon_\gamma} = \frac{\langle N_P \rangle}{0.95} \tag{5.43}$$

The resulting limits are shown in figure 5.24.

5.12. Limits on the photon fraction at ultra-high energies from Centaurus A

The limits on the photon count from Centaurus A are not of much use. It can not be easily compared to results from other experiments or analyses. Furthermore, it is not a physical quantity but dependent on the experiment and data set. More useful quantities would be a limit on the photon fraction and the photon flux. Both have their own challenges. To calculate the photon flux, the exposure for photon induced air showers of the detector has to be determined. At least a lower limit on the exposure is needed for a conservative photon flux limit. This is not done in this analysis.

Calculating the limit on the photon fraction has its own challenges. The photon fraction f_γ is defined as

$$f_\gamma = \frac{N_\gamma}{N_\gamma + N_{\text{hadr}}} = \frac{N_\gamma}{N_{\text{tot}}} \tag{5.44}$$

[14]This is the confidence level.

with the photon number N_γ, the number of hadronic showers N_{hadr} and the total event count N_{tot}. The main problem appears when the energy dependence is added to equation 5.44:

$$f_\gamma(E) = \frac{N_\gamma(E_\gamma(E))}{N_\gamma(E_\gamma(E)) + N_{\mathrm{hadr}}(E)} = \frac{N_\gamma(E_\gamma(E))}{N_{\mathrm{tot}}(E)} \tag{5.45}$$

Here E is the energy interval of true energy (which is the same as the apparent energy interval for hadrons) and $E_\gamma(E)$ is the reconstructed energy interval for photons corresponding to E. The problem arises from the different energy scales of photon induced air showers (E_γ) and hadron induced air showers (E). Therefore, it is nearly impossible to get the correct number of N_{tot}, unless N_γ and N_{hadr} are known exactly – this is not the case for N_γ, for which only a limit is known.

Nevertheless, the (obviously not completely correct) count of all events with reconstructed energy in the interval E is used as an estimator for $N_{\mathrm{tot}}(E)$. That means $N_\gamma(E_\gamma) \approx N_\gamma(E)$ is used in the denominator. The resulting systematic uncertainty is expected to be small, because N_γ is small compared to N_{hadr}, and the difference between E and E_γ is also small compared to the width of the intervals.

So the limit on the photon fraction is given as

$$f_{\gamma,95\%} = \frac{N_{\gamma,95\%}}{N_{\mathrm{tot}}} \tag{5.46}$$

An additional statistical uncertainty on this quantity is given through the (Poissonian) uncertainty on N_{tot}:

$$\sigma(f_{\gamma,95\%}) = \frac{f_{\gamma,95\%}}{\sqrt{N_{\mathrm{tot}}}} \tag{5.47}$$

This uncertainty is in addition to the uncertainty that is inherent to limits given at a specific confidence level. There is no easy way to include it into the confidence level formalism. For this a direct calculation of the limit on the photon fraction would be needed, without a detour via a limit on the photon count. N_{tot} would have to be included and varied in the toy-MC. As a downside, the significance formula could be no longer used as a means of comparison.

5.12.1. Correction for different detector acceptance

Equation 5.46 gives a limit on the observed photon fraction. The interesting quantity is the fraction of γ among the primaries which enter the atmosphere. Therefore, a correction for effects of different acceptance of the detector after cuts for photon and proton induced air showers has to be done.

It can be seen that $N_\gamma = p_\gamma \cdot N_{\gamma,\mathrm{true}}$ and $N_{\mathrm{hadr}} = p_{\mathrm{hadr}} \cdot N_{\mathrm{hadr,true}}$. Here the acceptance probabilities p_γ and p_{hadr} are the probabilities for γ or hadron induced air showers to be measured with the detector, reconstructed and not discarded by the quality cuts. For this analysis it is assumed that $p_{\mathrm{hadr}} = p_{\mathrm{p}}$, which means $N_{\mathrm{hadr}} = p_{\mathrm{p}} \cdot N_{\mathrm{hadr,true}}$.

$$f_{\gamma,\mathrm{true}} = \frac{N_{\gamma,\mathrm{true}}}{N_{\gamma,true} + N_{\mathrm{hadr,true}}} = \frac{N_\gamma/p_\gamma}{N_\gamma/p_\gamma + N_{\mathrm{hadr}}/p_{\mathrm{p}}} = \frac{p_{\mathrm{p}}}{p_\gamma}\frac{N_\gamma}{N_\gamma\frac{p_{\mathrm{p}}}{p_\gamma} + N_{\mathrm{hadr}}} \tag{5.48}$$

$$\leq \frac{p_{\mathrm{p}}}{p_\gamma}\frac{N_\gamma}{N_\gamma + N_{\mathrm{hadr}}} = \frac{p_{\mathrm{p}}}{p_\gamma} f_\gamma \tag{5.49}$$

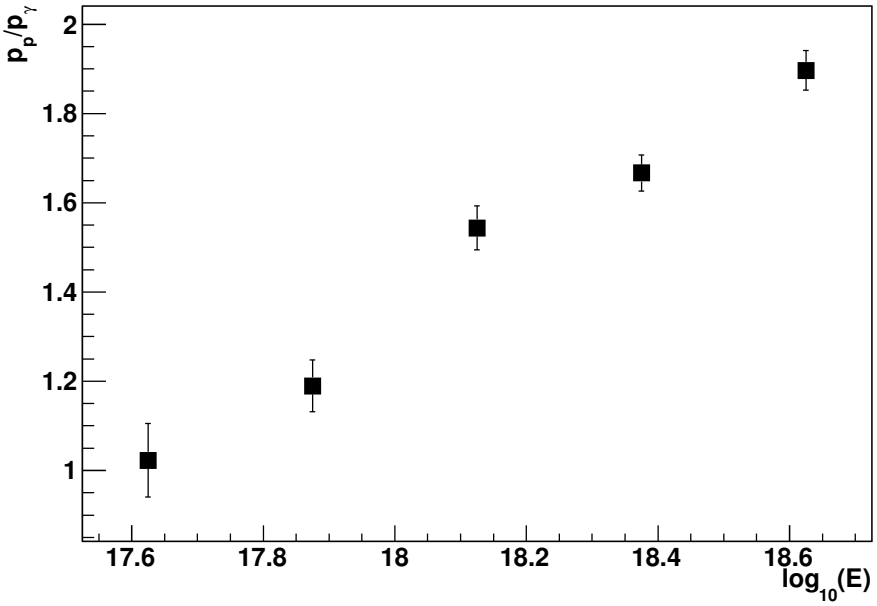

Figure 5.25.: Ratio of acceptance probabilities (after reconstruction and cuts) for proton and γ induced air showers. Simulations have been reweighted for zenith angle distribution from Centaurus A and energy spectrum $\gamma = 3$.

The inequation 5.49 holds as long as $p_\mathrm{p} > p_\gamma$ (the identity is true when $p_\mathrm{p} = p_\gamma$ or $N_\gamma = 0$). In this case the photon fraction is overestimated, which means a conservative limit arises.

The ratio of acceptance probabilities (the absolute values do not matter) has to be determined by simulations. This is the first place in this analysis where the hadronic composition and the hadronic interaction model matter. A pure protonic composition with QGSJET-II as interaction model is assumed. Other primaries and interaction models would have to be used to get an estimator for the systematic uncertainty arising from this choice. This is beyond the scope of this thesis.

The same number of simulated CORSIKA showers are used for photons and protons. All events are reweighted by energy ($\gamma = 3$) and zenith angle (see section 5.5) and sorted into energy bins by their true (MC) energy. The sum of the weights Σ_γ and Σ_p is generated for every energy bin together with the sum of the squares of the weights $\Sigma_{\gamma,2}$ and $\Sigma_{\mathrm{p},2}$.

The ratio of the sum of weights is used as an estimator of the acceptance probability ratio:

$$\frac{p_\mathrm{p}}{p_\gamma} = \frac{\Sigma_\mathrm{p}}{\Sigma_\gamma} \tag{5.50}$$

The statistical uncertainty on the ratio can be estimated through

$$\sigma\left(\frac{p_\mathrm{p}}{p_\gamma}\right) = \frac{\Sigma_\mathrm{p}}{\Sigma_\gamma}\sqrt{\left(\frac{\sigma\left(\Sigma_\gamma\right)}{\Sigma_\gamma}\right)^2 + \left(\frac{\sigma\left(\Sigma_\mathrm{p}\right)}{\Sigma_\mathrm{p}}\right)^2} = \frac{\Sigma_\mathrm{p}}{\Sigma_\gamma}\sqrt{\left(\frac{\sqrt{\Sigma_{\gamma,2}}}{\Sigma_\gamma}\right)^2 + \left(\frac{\sqrt{\Sigma_{p,2}}}{\Sigma_\mathrm{p}}\right)^2} \tag{5.51}$$

which is the Gaussian error propagation on the ratio, where $\sigma\left(\Sigma_x\right) = \sqrt{\Sigma_{x,2}}$.

The acceptance probability ratios are shown in figure 5.25 and table 5.4. It is greater

Energy (eV)	$10^{17.5}$–$10^{17.75}$	$10^{17.75}$–10^{18}	10^{18}–$10^{18.25}$	$10^{18.25}$–$10^{18.5}$
p_p/p_γ	1.02±0.08	1.19±0.06	1.54±0.05	1.67±0.04

Table 5.4.: Ratio of acceptance probabilities (after reconstruction and cuts) for proton and γ induced air showers. Simulations have been reweighted for zenith angle distribution from Centaurus A and energy spectrum $\gamma = 3$.

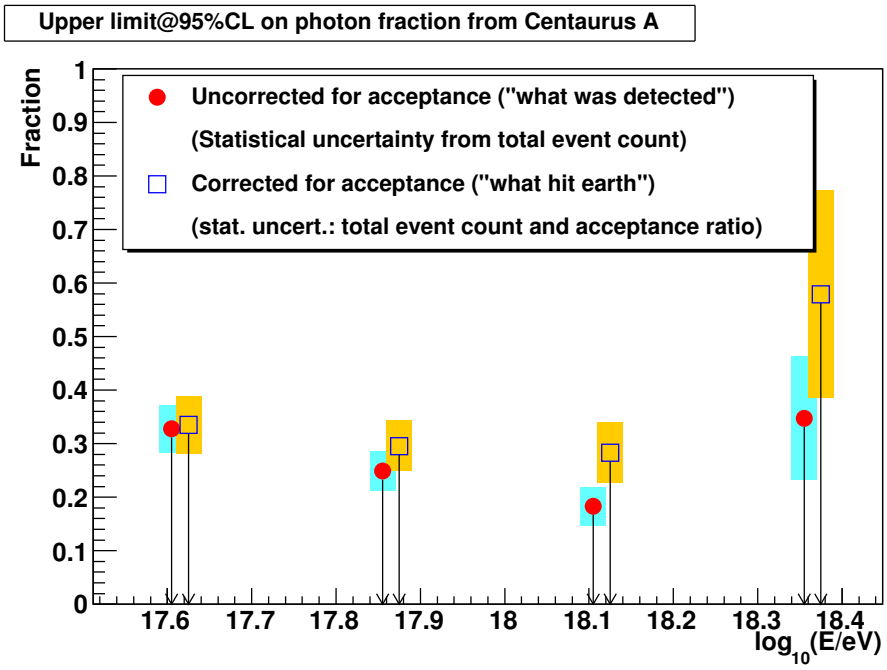

Figure 5.26.: Upper limits on the photon fraction at 95% confidence level in different energy bins. Additional statistical uncertainties are shown as colored bands. The fractions shown with red filled circles are limits on the photon fraction in the detected events. The fractions shown with blue squares are corrected for the different acceptance probabilities of photons and hadrons and are a limit on the real physical photon fraction, not biased by detector effects.

than unity for all energies. That means equation 5.49 can be used as a conservative estimator of the true photon fraction limit.

In figure 5.26 the uncorrected limits $f_{\gamma,95\%}$ and corrected limits $f_{\gamma,95\%,true}$ are plotted. The additional statistical uncertainty on $f_{\gamma,95\%,true}$ is calculated:

$$\sigma\left(f_{\gamma,95\%,true}\right) = f_{\gamma,95\%,true} \cdot \left(\frac{\sigma\left(\frac{p_p}{p_\gamma}\right)}{\frac{p_p}{p_\gamma}} \oplus \frac{\sigma(f_{\gamma,95\%})}{f_{\gamma,95\%}} \right) \tag{5.52}$$

The additional statistical uncertainties on the fractions can not easily be incorporated into the confidence level expression which is symbolized by the downwards arrow.

It can be seen that the statistics is not sufficient to produce reliable limits in the energy range above $10^{18.25}$ eV. At energies between $10^{17.5}$ and $10^{18.25}$, the photon fraction at 95% confidence level from Centaurus A is below 35%. This photon fraction only includes an excess of photons from the Centaurus A region compared to the background region but not a possible overall diffuse photon fraction.

There are some sources of systematic uncertainties. The first one is the acceptance probability correction. Here the used primary and interaction model (chosen as proton

Energy interval (eV)	Photon count limit @95%CL	Photon fraction limit@95%CL	
		uncorrected	corrected
$10^{17.5}$ –$10^{17.75}$	17.4	0.33±0.05	0.34±0.05
$10^{17.75}$–10^{18}	11.2	0.25±0.04	0.30±0.05
10^{18} –$10^{18.25}$	4.8	0.18±0.04	0.28±0.06
$10^{18.25}$–$10^{18.5}$	3.1	0.35±0.12	0.58±0.19

Table 5.5.: Upper limits on photon fraction and photon counts in different energy intervals.

and QGSJET-II) introduce an uncertainty. It might also be changed by a different choice of the spectral index or a time-dependent detector simulation using the true detector status. The second systematic uncertainty comes from possible differences in the hadronic composition between signal and background regions, which might go undetected by the KS-test. Both are not studied or quantified for this analysis. The spectral index of photons for the simulations also affects the calculated $X_{\max}$-cut values, which mainly manifests as a systematic uncertainty on the photon efficiency ε_γ. These systematics is hopefully small because of the small energy bins. Another not thoroughly studied possible source of systematic uncertainty is the seasonal dependence of the zenith-angle and $X_{\max}$ distributions that accompanies the choice of the background region in right ascension.

All systematic uncertainties are assumed to be small compared to the large statistical uncertainties.

5.13. Discussion of results

In concordance with all other searches for UHE photon induced air showers, this analysis does not find evidence for the existence of UHE photons in the cosmic rays. The upper limits on the photon fraction set in this analysis (figure 5.27), which are between 30 % and 35 % for energies between $10^{17.5}$ eV and $10^{18.25}$ eV, are too high to exclude any of the common photon production models shown in 4.10. However, the theoretical predictions are calculated for all-sky events and have to be adapted to the case of the point source Centaurus A.

Limits for Centaurus A are not explicitly given in [28], but results in the region around Centaurus A do not appear to be special when compared to the rest of the sky. The limits set in [28] are in the order of 1 % when a Gaussian weight of 6° is applied to the events and in the order of 10 % when a Gaussian weight of 1° is applied, which is much stricter than the limits set in this thesis.

It is not easy to compare the upper limits on the photon fraction set in this analysis with other analyses. Usually integral limits are given for open energy intervals without an upper border (analyses in [64] and [65]). The analysis in [28] uses only one energy bin from $10^{17.2}$ eV to $10^{18.5}$ eV and therefore has a larger data set in each energy bin compared to this analysis. This is one of the possible reasons for the lower limits of the analysis in [28]. To increase the width of the energy bins and to allow integral limits for this analysis, a different solution to determine the energy dependent $X_{\max}$-cut would have to be found. For the much broader energy intervals, the role of the chosen spectral index for simulations would vastly increase. The systematics introduced by wrong assumptions on the spectral index and a possible difference of spectral indices of

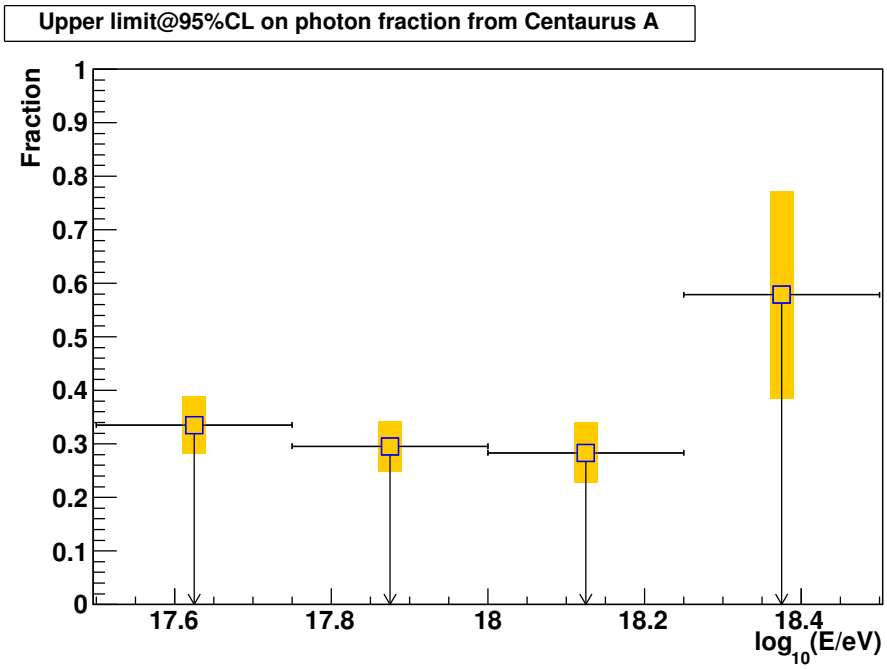

Figure 5.27.: Upper limits on the photon fraction at 95% confidence level in different energy bins. Additional statistical uncertainties are shown as colored blocks. The fractions are corrected for the different acceptance probabilities of photons and hadrons and are a limit on the real physical photon fraction.

hadronic and photonic cosmic rays would have to be studied.

The analysis in [28] has a lower statistical uncertainty on the background expectation than this analysis. Through the use of a method called "shuffling technique", all events can be used to calculate the background expectation, not just a limited background region. It might be worth evaluating the possibility to get a better expectation value of the background through a greater event count in the background region. After a thorough study of the seasonal dependence of events and the effect of the right ascension on data, the background region could be extended in right ascension. Perhaps even the complete all-sky event set could be used as background with the proper reweighting of zenith angle. For this a new estimator for significance has to be found, which also works on weighted event counts. It might even be possible to slightly increase the background region radius if the new systematic uncertainty introduced by this is outweighed by the decrease in statistical uncertainty.

There are various parameters in this analysis, like the radius of the signal region or the photon efficiency of the $X_{\max}$ cut, that have been chosen a priori and can in principle be changed. Although a change would likely bring the limits set in this analysis below 10 %, it has not been done to prevent the bias imposed by trying too many values and using the ones which give the best limits. To get a better discriminatory power between photons and hadrons, a second $X_{\max}$ cut value at a lower photon efficiency (e.g. ε_γ = 0.7), which means a higher $X_{\max}$ value and a much reduced hadron background count in the high range, could be introduced. Of the three resulting $X_{\max}$ ranges, the lowest would still be used to determine the exposure ratio and check for the hadronic composition, the highest would be used to set the photon limit, the middle range would not be used. The downside of this measure would be a much higher uncertainty on the background expectation because of the much lower statistics. The analysis in [28] uses photon efficiencies of 0.46 and 0.86. Independent of the photon efficiency, the

hadron background suppression is better in [28] than in this analysis, because also other variables than the X_{max} are used for photon discrimination.

Although the limits in [28] are better than the limits in this thesis, through the use of SD observables there are much more possible systematic uncertainties than in this thesis.

6. Summary and Outlook

It was shown, that the slant depth of the maximum ($X_{\max}$) of extensive air showers, measured with the fluorescence detector of the Pierre Auger Observatory, can be used for hadron-photon-discrimination.

Centaurus A has been chosen as a source candidate for a search for a point source of UHE photons. The method chosen involved comparing the $X_{\max}$-distributions between events from a signal region with a radius of 4° around Centaurus A and events from a suitable background region, which has been found using the zenith angle distribution of events as an argument. To obtain a nearly photon-free subset of data, a cut on $X_{\max}$ was introduced using simulations of photon induced air showers, which selects photons with 95% efficiency. The correct zenith angle distribution as observed from the Centaurus A-region has been used for the simulations. Using the Kolmogorov-Smirnov test, it has been shown that the hadronic composition seems to be identical between signal region and background region, so that the search for photons could be performed.

To search for photons, the count of the photon candidate events in the signal region was compared with the count of photon candidate events in the background region. The complementary photon-reduced event count was used as a scaling factor between signal and background region. To get a significance of observed event counts, the Li-Ma-formula was adopted to the case of a not exactly known scaling factor α.

Between $10^{17.5}$ eV and 10^{18} eV an over-fluctuation of photon candidate events with a significance of 1.5 was observed. Between 10^{18} eV and $10^{18.5}$ eV no excess was found. Converted to a limit at a confidence level of 95%, the photon fraction is below 40% between $10^{17.5}$ eV and $10^{17.75}$ eV, and below 35% between $10^{17.75}$ eV and $10^{18.25}$ eV. This does not reach the limits found in [28].

The main limitation at the moment is small statistics, which can only be improved by data to be taken in the next years.

There are various possible changes to the method, which are worthy to be considered. The radius of the signal region could be modified to better match the expected photonic size of Centaurus A. Here the steep drop in statistics reduces the feasibility. An $X_{\max}$ cut at a lower photon efficiency might lead to better limits because of a much reduced hadron background count in the high $X_{\max}$ range. The current $X_{\max}$ cut would still be needed additionally to define a low range to determine the background scaling factor and to test the composition of the hadronic background.

It might be worth evaluating the possibility to get a better expectation value of the background through a greater event count in the background region. The energy binning could be changed to give integral limit or use only one energy bin, but this would need a really energy dependent $X_{\max}$-cut and not one value per energy bin.

There are various other useful tests for the comparison of two $X_{\max}$-distributions in the low $X_{\max}$-region, like the Cramér-von Mises test [66, 11.4.1]. It might be worth evaluating those tests to better find or reject a difference in hadronic composition that poses a source of systematic uncertainty.

Bibliography

[1] V.F. Hess. Über Beobachtungen der durchdringenden Strahlung bei sieben Freiballonfahrten. *Physikalische Zeitschrift*, 13:1084–1091, 1912.

[2] D. J. Bird, S. C. Corbato, H. Y. Dai, J. W. Elbert, K. D. Green, M. A. Huang, D. B. Kieda, S. Ko, C. G. Larsen, E. C. Loh, M. Z. Luo, M. H. Salamon, J. D. Smith, P. Sokolsky, P. Sommers, J. K. K. Tang, and S. B. Thomas. Detection of a cosmic ray with measured energy well beyond the expected spectral cutoff due to cosmic microwave radiation. *The Astrophysical Journal*, 441:144–150, March 1995.

[3] T. K. Gaisser and T. Stanev. High-energy cosmic rays. *Nuclear Physics A*, 777:98–110, October 2006. arXiv:astro-ph/0510321.

[4] J. Abraham et al. Measurement of the energy spectrum of cosmic rays above 10^{18} eV using the Pierre Auger Observatory. *Physics Letters B*, 685:239–246, March 2010. arXiv:1002.1975v1 [astro-ph.HE].

[5] J. Blümer, R. Engel, and J. R. Hörandel. Cosmic rays from the knee to the highest energies. *Progress in Particle and Nuclear Physics*, 63:293–338, October 2009.

[6] W. F. Hanlon. Updated cosmic ray spectrum, November 2011. `http://www.physics.utah.edu/~whanlon/spectrum.html`, visited 2011-11-21.

[7] P. Homola, J. Abraham, et al. Ultra-high energy photon studies with the Pierre Auger Observatory. *Proc. 31st Int. Cosmic Ray Conf.*, 2009. arXiv:0906.2347v2 [astro-ph.HE].

[8] E. Fermi. On the Origin of the Cosmic Radiation. *Physical Review*, 75:1169–1174, April 1949.

[9] R. D. Blandford and J. P. Ostriker. Particle acceleration by astrophysical shocks. *The Astrophysical Journal Letters*, 221:L29–L32, April 1978.

[10] C. Wiebusch. Lecture Notes to "Astroteilchenphysik". RWTH Aachen, SS2010.

[11] A. M. Hillas. The Origin of Ultra-High-Energy Cosmic Rays. *Annual review of astronomy and astrophysics*, 22:425–444, 1984.

[12] D. F. Torres and L. A. Anchordoqui. Astrophysical origins of ultrahigh energy cosmic rays. *Reports on Progress in Physics*, 67:1663–1730, September 2004. arXiv:astro-ph/0402371.

[13] G. L. H. Harris, M. Rejkuba, and W. E. Harris. The Distance to NGC 5128 (Centaurus A). *Publications of the Astronomical Society of Australia (PASA)*, 27:457–462, October 2010.

[14] M. Cappellari, N. Neumayer, J. Reunanen, P. P. van der Werf, P. T. de Zeeuw, and H.-W. Rix. The mass of the black hole in Centaurus A from SINFONI AO-assisted integral-field observations of stellar kinematics. *MNRAS*, 394:660–674, April 2009. arXiv:0812.1000v1 [astro-ph].

[15] D. L. Meier, D. L. Jauncey, R. A. Preston, A. K. Tzioumis, A. E. Wehrle, R. Batchelor, J. Gates, P. A. Hamilton, B. R. Harvey, R. F. Haynes, B. Johnson, P. . McCulloch, G. Moorey, D. D. Morabito, G. D. Nicolson, A. E. Niell, J. G. Robertson, G. W. R. Royle, L. Skjerve, M. A. Slade, O. B. Slee, A. Watkinson, and A. E. Wright. The high-resolution structure of the Centaurus A nucleus at 2.3 and 8.4 GHz. *Astronomical Journal*, 98:27–35, July 1989.

[16] H. Alvarez, J. Aparici, J. May, and P. Reich. The radio continuum spectrum of Centaurus A's large-scale components. *Astronomy and Astrophysics*, 355:863–872, March 2000.

[17] NASA/CXC/CfA/R.Kraft et al. Chandra X-ray Image of Centaurus A, 2008. `http://chandra.harvard.edu/photo/2008/cena/more.html`, visited 2011-12-21.

[18] P. L. Biermann and V. de Souza. On a common origin of galactic and extragalactic cosmic rays. *ArXiv e-prints*, June 2011. arXiv:1106.0625v1 [astro-ph.HE].

[19] F. Aharonian et al. Discovery of Very High Energy γ-Ray Emission from Centaurus A with H.E.S.S. *Astrophysical Journal Letters*, 695:L40–L44, April 2009. arXiv:0903.1582v1 [astro-ph.CO].

[20] M. Grigat. *Large scale anisotropy studies of ultra high energy cosmic rays using data taken with the surface detector of the Pierre Auger Observatory.* PhD thesis, RWTH Aachen, 2011.

[21] K. Greisen. End to the Cosmic-Ray Spectrum? *Physical Review Letters*, 16:748–750, April 1966.

[22] G. T. Zatsepin and V. A. Kuz'min. Upper Limit of the Spectrum of Cosmic Rays. *Journal of Experimental and Theoretical Physics Letters*, 4:78, August 1966.

[23] G. R. Blumenthal. Energy Loss of High-Energy Cosmic Rays in Pair-Producing Collisions with Ambient Photons. *Phys. Rev. D*, 1:1596–1602, March 1970.

[24] M. Risse and P. Homola. Search for ultrahigh energy photons using air showers. *Mod.Phys.Lett.*, A22:749–766, 2007. arXiv:astro-ph/0702632.

[25] G. B. Gelmini, O. E. Kalashev, and D. V. Semikoz. GZK photons as ultra-high-energy cosmic rays. *Journal of Experimental and Theoretical Physics*, 106:1061–1082, June 2008. arXiv:astro-ph/0506128.

[26] A. Kusenko, J. Schissel, and F. W. Stecker. Interactions of ultrahigh-energy cosmic rays with photons in the galactic center. *Astroparticle Physics*, 25:242–245, May 2006. arXiv:astro-ph/0508142.

[27] R. W. Clay, B. J. Whelan, and P. G. Edwards. Centaurus A at Ultra-High Energies. *Publications of the Astronomical Society of Australia (PASA)*, 27:439–448, October 2010. arXiv:1001.0813v1 [astro-ph.HE].

[28] D. Kuempel. *Multivariate Search for a Directional Excess of EeV Photons with the Pierre Auger Observatory.* PhD thesis, Bergische Universität Wuppertal, March 2011. GAP2011-053.

[29] Pierre Auger, P. Ehrenfest, R. Maze, J. Daudin, and Robley A. Fréon. Extensive cosmic-ray showers. *Rev. Mod. Phys.*, 11:288–291, July 1939.

[30] O. C. Alkhofer. *Introduction to Cosmic Radiation.* Verlag Carl Thiemig, 1975.

[31] T. K. Gaisser and A. M. Hillas. Reliability of the method of constant intensity cuts

for reconstructing the average development of vertical showers. *Proc. 15th ICRC*, 8:353–357, 1977.

[32] F. Arqueros, J. R. Hörandel, and B. Keilhauer. Air fluorescence relevant for cosmic-ray detection—Summary of the 5th fluorescence workshop, El Escorial 2007. *Nuclear Instruments and Methods in Physics Research A*, 597:1–22, November 2008. arXiv:0807.3760 [astro-ph].

[33] T. Suomijarvi, J. Abraham, et al. Performance and operation of the Surface Detector of the Pierre Auger Observatory. *Proc. 31st Int. Cosmic Ray Conf.*, 2009. arXiv:0906.2354v2 [astro-ph.IM].

[34] H. P. Dembinski. *Measurement of the flux of ultra high energy cosmic rays using data from very inclined air showers at the Pierre Auger Observatory.* PhD thesis, RWTH Aachen, 2009.

[35] J. Abraham et al. The Fluorescence Detector of the Pierre Auger Observatory. *Nucl.Instrum.Meth.*, A620:227–251, August 2010. arXiv:0907.4282v1 [astro-ph.IM].

[36] N. Sakaki, Y. Watanabe, M. Nagano, and K. Kobayakawa. Fluorescence in air excited by electrons from a ^{90}Sr source. *Nuclear Instruments and Methods in Physics Research A*, 597:88–93, November 2008.

[37] T. H.-J. Mathes. The HEAT Telescopes of the Pierre Auger Observatory: Status and First Data. *Proc. 32nd Int. Cosmic Ray Conf.*, 2011. arXiv:1107.4807v1 [astro-ph.IM].

[38] F. Sánchez, J. Abraham, et al. The AMIGA detector of the Pierre Auger Observatory: an overview. *Proc. 32nd Int. Cosmic Ray Conf.*, 2011. arXiv:1107.4807v1 [astro-ph.IM].

[39] J. L. Kelley, J. Abraham, et al. AERA: the Auger Engineering Radio Array. *Proc. 32nd Int. Cosmic Ray Conf.*, 2011. arXiv:1107.4807v1 [astro-ph.IM].

[40] P. S. Allison, J. Abraham, et al. Microwave detection of cosmic ray showers at the Pierre Auger Observatory. *Proc. 32nd Int. Cosmic Ray Conf.*, 2011. arXiv:1107.4807v1 [astro-ph.IM].

[41] M. Mostafá and The Pierre AUGER Collaboration. Hybrid Activities of the Pierre Auger Observatory. *Nuclear Physics B Proceedings Supplements*, 165:50–58, 2007.

[42] B.R. Dawson, J. Abraham, et al. Hybrid Performance of the Pierre Auger Observatory. *Proc. 30th Int. Cosmic Ray Conf.*, 2011. arXiv:0706.1105v1 [astro-ph].

[43] D. Kuempel, K.-H. Kampert, and M. Risse. Geometry reconstruction of fluorescence detectors revisited. *Astroparticle Physics*, 30:167–174, November 2008. arXiv:0806.4523 [astro-ph].

[44] T. Pierog et al. Dependence of the longitudinal shower profile on the characteristics of hadronic multiparticle production. *Proc. 29th Int. Cosmic Ray Conf.*, 7:103, 2005.

[45] H. M.J. Barbosa, F. Catalani, J.A. Chinellato, and C. Dobrigkeit. Determination of the calorimetric energy in extensive air showers. *Astropart.Phys.*, 22:159–166, 2004. arXiv:astro-ph/0310234v3.

[46] S. Argiro, S.L.C. Barroso, J. Gonzales, L. Nellen, T. Paul, T.A. Porter, L. Prado Jr., M. Roth, R. Ulrich, and D. Veberic. The Offline framework of the Pierre Auger Observatory. *Nucl. Instr. and Meth.*, A580:1485–1496, 2007.

[47] D. Heck, J. Knapp, J.N. Capdevielle, G. Schatz, and T. Thouw. CORSIKA: A Monte Carlo Code to Simulate Extensive Air Showers. *FZKA*, 6019, 1998.

[48] D. Heck. The CURVED Version of the Air Shower Simulation Program CORSIKA. *FZKA*, 6954, 2004.

[49] D. Heck and J. Knapp. Upgrade of the Monte Carlo Code CORSIKA to Simulate Extensive Air Showers with Energies $> 10^{20}$ eV. *FZKA*, 6097, 1998.

[50] D. Heck. nie fertig werdende CORSIKA-Simulationen. private communication, 2011.

[51] S. Ostapchenko. On the re-summation of enhanced Pomeron diagrams. *Phys.Lett.*, B636:40–45, 2006.

[52] S. Ostapchenko. Non-linear screening effects in high energy hadronic interactions. *Phys.Rev.*, D74:014026, 2006.

[53] G. Battistoni, S. Muraro, P.R. Sala, F. Cerutti, A. Ferrari, S. Roesler, A. Fassò, and J. Ranft. The FLUKA code: Description and benchmarking. *AIP Conference Proceeding*, 896:31–49, 2007. Proceedings of the Hadronic Shower Simulation Workshop 2006, Fermilab 6–8 September 2006, M. Albrow, R. Raja eds.

[54] A. Ferrari, P.R. Sala, A. Fassò, and J. Ranft. FLUKA: a multi-particle transport code. *CERN-2005-10*, 2005. INFN/TC_05/11, SLAC-R-773.

[55] W. R. Nelson, H. Hirayama, and D. W. O. Rogers. The EGS4 Code System. *SLAC report*, 265, December 1985.

[56] C. Bleve, J. Knapp, and J. Schovanscová. Parameters and strategy for a CORSIKA mass production below 65°. *Auger internal note*, August 2008. GAP-2009-075.

[57] R. Engel. Some Comments on the Energy Scale of the Pierre Auger Observatory. *AIP Conference Proceedings*, 1367(1):50–53, 2011.

[58] E. Konishi, A. Adachi, N. Takahashi, and A. Misaki. On the characteristics of individual cascade showers with the LPM effect in extremely high-energies. *J.Phys.G*, G17:719–732, 1991.

[59] S. Klein. Suppression of bremsstrahlung and pair production due to environmental factors. *Rev. Mod. Phys.*, 71:1501–1538, 1999. arXiv:hep-ph/9802442.

[60] A.N. Cillis, H. Fanchiotti, C.A. Garcia Canal, and S.J. Sciutto. Influence of the LPM effect and dielectric suppression on particle air showers. *Phys.Rev.*, D59:113012, 1999. arXiv:astro-ph/9809334.

[61] T. Stanev and H.P. Vankov. The Nature of the highest energy cosmic rays. *Phys.Rev.*, D55:1365–1371, 1997. arXiv:astro-ph/9607011.

[62] X. Bertou, P. Billoir, and S. Dagoret-Campagne. LPM effect and pair production in the geomagnetic field: a signature of ultra-high energy photons in the Pierre Auger Observatory. *Astroparticle Physics*, 14(2):121 – 130, 2000.

[63] P. Homola, D. Góra, D. Heck, H. Klages, J. PeĶala, M. Risse, B. Wilczyńska, and H. Wilczyński. Simulation of ultra-high energy photon propagation in the geomagnetic field. *Computer Physics Communications*, 173:71–90, December 2005. arXiv:astro-ph/0311442.

[64] J. Abraham et al. Upper limit on the cosmic-ray photon fraction at EeV energies from the Pierre Auger Observatory. *Astropart.Phys.*, 31:399–406, 2009.

arXiv:0903.1127v2 [astro-ph.HE].

[65] M. Settimo, J. Abraham, et al. An update on a search for ultra-high energy photons using the Pierre Auger Observatory. *Proc. 32nd Int. Cosmic Ray Conf.*, 2011. arXiv:1107.4805v1 [astro-ph.HE].

[66] F. James. *Statistical Methods in Experimental Physics*. World Scientific, Singapore, 2nd edition, 2006. ISBN 981-270-527-9.

[67] I. N. Bronstein, K. A. Semendjajew, G. Musiol, and H. Mühlig. *Taschenbuch der Mathematik*. Verlag Harri Deutsch, Frankfurt/Main, 6 edition, 2005.

[68] B. List. Statistical Error of Efficiency Determination from Weighted Events. `http://www.desy.de/~blist/notes/effic.ps.gz`.

[69] T.-P. Li and Y.-Q. Ma. Analysis methods for results in gamma-ray astronomy. *The Astrophysical Journal*, 272:317–324, September 1983.

Appendix A.

Steering cards

A.1. CORSIKA steering cards

The shown steering card is for a photon induced shower. For a proton induced shower, the "PRMPAR" parameter is changed to 14 and the "GCOORD" line is removed.

```
1  RUNNR   1000
2  EVTNR   1                                  number of first ↙
       ↳ shower event
3  NSHOW   1                                  number of showers to ↙
       ↳ generate
4  PRMPAR  1                                  particle type of ↙
       ↳ prim. particle
5  ESLOPE  -1                                 slope of primary ↙
       ↳ energy spectrum
6  ERANGE  3.16227E8  3.98107E8               energy range of ↙
       ↳ primary particle (10^(17.5) .. 10^(17.6)) eV
7  THETAP  0.  65.                            range of zenith angle ↙
       ↳ (degree)
8  PHIP    -180.  180.                        range of azimuth ↙
       ↳ angle (degree)
9  OBSLEV  1.452E+05                          observation level (in ↙
       ↳ cm)
10 FIXCHI  0.                                 starting altitude ↙
       ↳ (g/cm**2)
11 MAGNET  2.010E+01  -1.420E+01
12 ECTMAP  2.5E+05
13 HADFLG  0  0  0  0  0  2                   flags ↙
       ↳ hadr.interact.&fragmentation
14 ECUTS   1.0E-01 1.0E-01 2.5E-04 2.5E-04    energy cuts for ↙
       ↳ particles
15 MUADDI  T                                  additional info for ↙
       ↳ muons
16 MUMULT  T                                  muon multiple ↙
       ↳ scattering angle
17 ELMFLG  F   T                              em. interaction flags ↙
       ↳ (NKG,EGS)
18 STEPFC  1.0                                mult. scattering step ↙
       ↳ length fact.
19 RADNKG  5.0E+05                            outer radius for NKG ↙
       ↳ lat.dens.distr.
```

```
20 ARRANG  0.                                  rotation of array to ↙
     ↳ north
21 LONGI   T  5.  T  T                         longit.distr. & step ↙
     ↳ size & fit & out
22 MAXPRT  1                                   max. number of ↙
     ↳ printed events
23 DATBAS  T                                   write .dbase file
24 PAROUT  T T                                 write DAT file
25 USER    middendorf                          user
26 THIN    1.E-06 3.16227E2 1.0E+04            thining parameters
27 THINH   1.0E+00 1.0E+02
28 DEBUG   F  6  F  1000000                    debug flag and ↙
     ↳ log.unit for out
29 GCOORD  -69.585 -35.463 2010. 2 0           geographical ↙
     ↳ coordinates used for PRESHOWER module
30 SEED    895648043 0 0
31 SEED    552147649 0 0
32 DIRECT  /some_fancy_directory_name/
33 EXIT
```

A.2. ADST cut files

The cuts are applied onto data and simulations using the `SelectEvents` program from the ADST toolkit.

A.2.1. fd.cuts

```
1  ADST cuts version: 1.0
2
3   badFDPeriodRejection
4   eyeCut              1111
5
6   # # geometry related cuts
7   maxCoreTankDist     1500.   # maximum shower plane distance ↙
      ↳ core-hybrid-tank
8   nAxisPixels         5       # min number of pixels used in ↙
      ↳ axis fit
9   timeFitChi2         5.
10  maxZenithFD         90.
11  # minViewAngle      15.     # minimum viewing angle
12
13
14  # # profile related cuts
15  profileChi2         2.5     # max reduced GH chi2
16  profileChi2Ratio    0.9     # cut on ratio of GH and linear ↙
      ↳ chi^2
17
18  xMaxInFOV           0.0     # max distance of xMax to borders
19  xMaxError           40.0    # max error on xMax [g/cm^2]
```

```
20  energyError          .2       # max error on energy (relative)
21
22  minLgEnergyFD        17.
23  maxCFrac             50.      # maximum Cherenkov-fraction [%]
```

A.2.2. sd.cuts

```
1  ADST cuts version: 1.0
2
3  # SD cuts
4  badPeriodsRejection
5  badPeriodsRejectionFromFile
```

A.3. Offline steering cards for simulation

A.3.1. ModuleSequence.xml

```
1  <!-- A sequence for golden hybrid simulation and ↙
       ↳ reconstruction -->
2
3  <sequenceFile>
4
5    <enableTiming/>
6
7    <moduleControl>
8
9      <loop numTimes="1" pushEventToStack="yes">
10
11       <module> EventFileReaderOG </module>
12       <module> MCShowerCheckerOG </module>
13
14       <loop numTimes="10" pushEventToStack="yes">
15
16         <module> EventGeneratorOG </module>
17
18         <!-- SD simulation part -->
19         <loop numTimes="unbounded" pushEventToStack="no">
20           <module> CachedShowerRegeneratorOG </module>
21           <module> FastTankSimulatorOG </module>
22         </loop>
23
24         <try>  <!-- catch triggerless events for RecData* -->
25
26           <module> SdSimulationCalibrationFillerOG </module>
27           <module> SdPMTSimulatorOG </module>
28           <module> SdFilterFADCSimulatorMTU </module>
29           <module> SdBaselineSimulatorOG </module>
30           <module> TankTriggerSimulatorOG </module>
31           <module> TankGPSSimulatorOG </module>
32
33           <!-- FD simulation part -->
```

```
34          <module> FdSimEventCheckerOG </module>
35          <module> ShowerLightSimulatorKG </module>
36          <module> LightAtDiaphragmSimulatorKG </module>
37          <module> ShowerPhotonGeneratorOG </module>
38          <module> TelescopeSimulatorKG </module>
39          <module> FdBackgroundSimulatorOG </module>
40          <module> FdElectronicsSimulatorOG </module>
41          <module> FdTriggerSimulatorOG </module>
42
43          <!-- Trigger and Event builder -->
44          <module> CentralTriggerSimulatorXb </module>
45          <module> CentralTriggerEventBuilderOG </module>
46          <module> EventBuilderOG </module>
47
48          <!-- export simulation in Offline format -->
49  <!--          <module> EventFileExporterOG </module> -->
50
51          <!-- Reconstruction -->
52          <module> EventCheckerOG </module>
53
54          <try> <!-- run RecData*, even if checker, ↙
                ↳ calibrator send Continue -->
55
56            <module> SdCalibratorOG </module>
57
58            <!-- Hybrid reconstruction -->
59            <try>  <!-- limit how far a Continue goes -->
60              <module> FdCalibratorOG </module>
61              <module> FdPulseFinderOG </module>
62              <module> PixelSelectorOG </module>
63              <module> FdSDPFinderOG </module>
64          <module> FdAxisFinderOG </module>
65              <module> HybridGeometryFinderOG </module>
66              <module> FdApertureLightOG </module>
67              <module> FdProfileReconstructorKG </module>
68            </try>
69
70            <!-- SD reconstruction -->
71            <try>   <!-- limit how far a Continue goes -->
72              <module> SdEventSelectorOG </module>
73              <module> SdMonteCarloEventSelectorOG </module>
74              <module> SdPlaneFitOG </module>
75              <module> LDFFinderKG </module>
76              <module> Risetime1000LLL </module>
77              <module> SdEventPosteriorSelectorOG </module>
78            </try>
79
80          </try> <!-- catch calibrator Continues -->
81        </try> <!-- catch trigger Continues -->
82
83        <!-- export the ADST -->
```

```
84          <module> RecDataWriterNG </module>
85
86        </loop>
87      </loop>
88
89    </moduleControl>
90
91 </sequenceFile>
```

A.3.2. bootstrap.xml

```
1  <?xml version="1.0" encoding="iso-8859-1"?>
2
3  <!DOCTYPE bootstrap [
4             <!ENTITY myConfigFiles '.'>
5             <!ENTITY standardSdIdealDetConfig SYSTEM '/home/↙
                 ↪ lm195519/offline_install/share/auger-offline/↙
                 ↪ config/standardSdIdealDetConfig.xml'>
6             <!ENTITY standardSdSimModuleConfig SYSTEM '/home/↙
                 ↪ lm195519/offline_install/share/auger-offline/↙
                 ↪ config/standardSdSimModuleConfig.xml'>
7             <!ENTITY standardSdRecModuleConfig SYSTEM '/home/↙
                 ↪ lm195519/offline_install/share/auger-offline/↙
                 ↪ config/standardSdRecModuleConfig.xml'>
8             <!ENTITY standardFdIdealDetConfig SYSTEM '/home/↙
                 ↪ lm195519/offline_install/share/auger-offline/↙
                 ↪ config/standardFdIdealDetConfig.xml'>
9             <!ENTITY standardFdSimModuleConfig SYSTEM '/home/↙
                 ↪ lm195519/offline_install/share/auger-offline/↙
                 ↪ config/standardFdSimModuleConfig.xml'>
10            <!ENTITY standardFdRecModuleConfig SYSTEM '/home/↙
                 ↪ lm195519/offline_install/share/auger-offline/↙
                 ↪ config/standardFdRecModuleConfig.xml'>
11            <!ENTITY standardHdRecModuleConfig SYSTEM '/home/↙
                 ↪ lm195519/offline_install/share/auger-offline/↙
                 ↪ config/standardHdRecModuleConfig.xml'>
12            ]>
13
14 <bootstrap xmlns:xsi="http://www.w3.org/2001/XMLSchema-↙
     ↪ instance"
15              xsi:noNamespaceSchemaLocation='/home/lm195519/↙
                   ↪ offline_install/share/auger-offline/config/↙
                   ↪ bootstrap.xsd'
16              xmlns:xlink="http://www.auger.org/schema/types">
17
18   &standardSdIdealDetConfig;
19   &standardSdSimModuleConfig;
20   &standardSdRecModuleConfig;
21
22   &standardFdIdealDetConfig;
23   &standardFdSimModuleConfig;
24   &standardFdRecModuleConfig;
```

```
25   &standardHdRecModuleConfig;
26
27   <centralConfig>
28
29     <configLink
30       id          = "FTelescopeListXMLManager"
31       type        = "XML"
32       xlink:href = "./FTelescopeList.xml"/>
33
34
35     <configLink
36       id          = "FastTankSimulator"
37       type        = "XML"
38       xlink:href = "/home/lm195519/offline_install/share/auger-offline/config/FastTankSimulator.xml"/>
39
40     <configLink
41       id          = "ModuleSequence"
42       type        = "XML"
43       xlink:href = "./ModuleSequence.xml"/>
44
45     <configLink
46       id          = "EventFileReader"
47       type        = "XML"
48       xlink:href = "./EventFileReader.xml"/>
49
50 <!--    <configLink
51       id          = "EventFileExporter"
52       type        = "XML"
53       xlink:href = "./EventFileExporter.xml"/>-->
54
55     <configLink
56       id          = "EventGenerator"
57       type        = "XML"
58       xlink:href = "./EventGenerator.xml"/>
59
60     <configLink
61       id          = "CachedShowerRegenerator"
62       type        = "XML"
63       xlink:href = "./CachedShowerRegenerator.xml"/>
64
65   </centralConfig>
66
67   <parameterOverrides>
68
69    <configLink id="FdProfileReconstructor">
70      <FdProfileReconstructorKG>
71      <profileCalculation>
72        <multipleScatteringLDF> eNone </multipleScatteringLDF>
73      </profileCalculation>
```

```
74        </FdProfileReconstructorKG>
75      </configLink>
76
77      <configLink id="RecDataWriter">
78        <RecDataWriter>
79          <asciiOutput>
80            <outputFileMode> eWrite </outputFileMode>
81            <mode> Hybrid </mode>
82          </asciiOutput>
83        </RecDataWriter>
84      </configLink>
85
86    </parameterOverrides>
87
88 </bootstrap>
```

Appendix B.

Miscellaneous

B.1. Calculations

B.1.1. Likelihood

This is equation 5.32 with an additional intermediate step:

$$
\begin{aligned}
L\left(X|\hat{\Theta}_c\right) &= L\left(X|\left\langle N_S\right\rangle = 0, \left\langle \hat{N}_B\right\rangle_c, \hat{\alpha}_c, \left\langle \hat{n}_{\text{off}}\right\rangle_c\right) \\
&= P\left(N_{\text{on}}|\left\langle N_{\text{on}}\right\rangle = \frac{\hat{\alpha}_c}{1+\hat{\alpha}_c}\left(N_{\text{on}}+N_{\text{off}}\right)\right)\cdot P\left(N_{\text{off}}|\left\langle N_{\text{off}}\right\rangle = \frac{1}{1+\hat{\alpha}_c}\left(N_{\text{on}}+N_{\text{off}}\right)\right)\cdot \\
&\quad P\left(n_{\text{on}}|\left\langle n_{\text{on}}\right\rangle = \frac{\hat{\alpha}_c}{1+\hat{\alpha}_c}\left(n_{\text{on}}+n_{\text{off}}\right)\right)\cdot P\left(n_{\text{off}}|\left\langle n_{\text{off}}\right\rangle = \frac{1}{1+\hat{\alpha}_c}\left(n_{\text{on}}+n_{\text{off}}\right)\right) \\
&= \frac{\left(\frac{\hat{\alpha}_c}{1+\hat{\alpha}_c}\left(N_{\text{on}}+N_{\text{off}}\right)\right)^{N_{\text{on}}}}{N_{\text{on}}!}\exp\left(-\frac{\hat{\alpha}_c}{1+\hat{\alpha}_c}\left(N_{\text{on}}+N_{\text{off}}\right)\right)\cdot \\
&\quad \frac{\left(\frac{1}{1+\hat{\alpha}_c}\left(N_{\text{on}}+N_{\text{off}}\right)\right)^{N_{\text{off}}}}{N_{\text{off}}!}\exp\left(-\frac{1}{1+\hat{\alpha}_c}\left(N_{\text{on}}+N_{\text{off}}\right)\right)\cdot \\
&\quad \frac{\left(\frac{\hat{\alpha}_c}{1+\hat{\alpha}_c}\left(n_{\text{on}}+n_{\text{off}}\right)\right)^{n_{\text{on}}}}{n_{\text{on}}!}\exp\left(-\frac{\hat{\alpha}_c}{1+\hat{\alpha}_c}\left(n_{\text{on}}+n_{\text{off}}\right)\right)\cdot \\
&\quad \frac{\left(\frac{1}{1+\hat{\alpha}_c}\left(n_{\text{on}}+n_{\text{off}}\right)\right)^{n_{\text{off}}}}{n_{\text{off}}!}\exp\left(-\frac{1}{1+\hat{\alpha}_c}\left(n_{\text{on}}+n_{\text{off}}\right)\right) \\
&= \frac{\left(\frac{\hat{\alpha}_c}{1+\hat{\alpha}_c}\left(N_{\text{on}}+N_{\text{off}}\right)\right)^{N_{\text{on}}}}{N_{\text{on}}!}\frac{\left(\frac{1}{1+\hat{\alpha}_c}\left(N_{\text{on}}+N_{\text{off}}\right)\right)^{N_{\text{off}}}}{N_{\text{off}}!}\cdot \\
&\quad \frac{\left(\frac{\hat{\alpha}_c}{1+\hat{\alpha}_c}\left(n_{\text{on}}+n_{\text{off}}\right)\right)^{n_{\text{on}}}}{n_{\text{on}}!}\frac{\left(\frac{1}{1+\hat{\alpha}_c}\left(n_{\text{on}}+n_{\text{off}}\right)\right)^{n_{\text{off}}}}{n_{\text{off}}!}\cdot \\
&\quad \exp\left(-\left(N_{\text{on}}+N_{\text{off}}+n_{\text{on}}+n_{\text{off}}\right)\right)
\end{aligned}
\tag{B.1}
$$

B.1.2. Statistical uncertainty of efficiency for weighted counts

In section 5.7 the statistical uncertainty for an efficiency calculated with weighted events is given as (equation 5.11):

$$
\sigma_\varepsilon = \frac{\sqrt{\sum\limits_L w_i^2\left(\sum\limits_H w_i\right)^2 + \sum\limits_H w_i^2\left(\sum\limits_L w_i\right)^2}}{\left(\sum w_i\right)^2} \tag{B.2}
$$

where the w_i are the weights of the single events which are summed over the L and the H data sample.

For the case of $w_i = 1$ with n events in L and $N - n$ events in H, it follows ($\varepsilon = n/N$):

$$\begin{aligned}
\sigma_\varepsilon &= \frac{\sqrt{n\,(N-n)^2 + (N-n)n^2}}{N^2} \\
&= \frac{\sqrt{\varepsilon N\,((1-\varepsilon)N)^2 + (1-\varepsilon)N\,(\varepsilon N)^2}}{N^2} \\
&= \sqrt{\frac{\varepsilon\,(1-\varepsilon)^2 N^3 + \varepsilon^2(1-\varepsilon)N^3}{N^4}} \\
&= \sqrt{\frac{\varepsilon\,(1-2\varepsilon+\varepsilon^2) + \varepsilon^2(1-\varepsilon)}{N}} \\
&= \sqrt{\frac{\varepsilon - 2\varepsilon^2 + \varepsilon^3 + \varepsilon^2 - \varepsilon^3}{N}} \\
&= \sqrt{\frac{\varepsilon - \varepsilon^2}{N}} = \sqrt{\frac{\varepsilon(1-\varepsilon)}{N}}
\end{aligned} \tag{B.3}$$

The usual binomial uncertainty arises.

B.2. Comparison of simulations and data

In section 5.5 the reweighting, which is needed to match the zenith angle distributions of events from Centaurus A with shower simulations, is introduced. The effect of the correction is shown for one energy bin. The other energy bins are shown here.

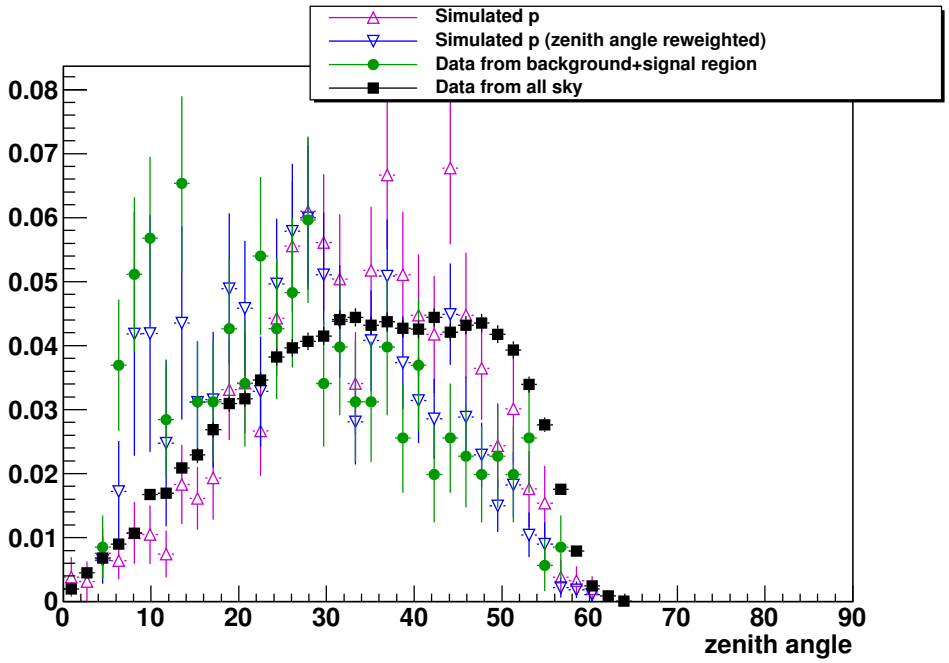

Figure B.1.: Comparison of the the all-sky data (black ■) and data (green ●) from background and signal region with standard CORSIKA proton simulations (purple △) and reweighted proton simulations (blue ▽). Reconstructed energy between $10^{17.5}$ eV and $10^{17.75}$ eV.

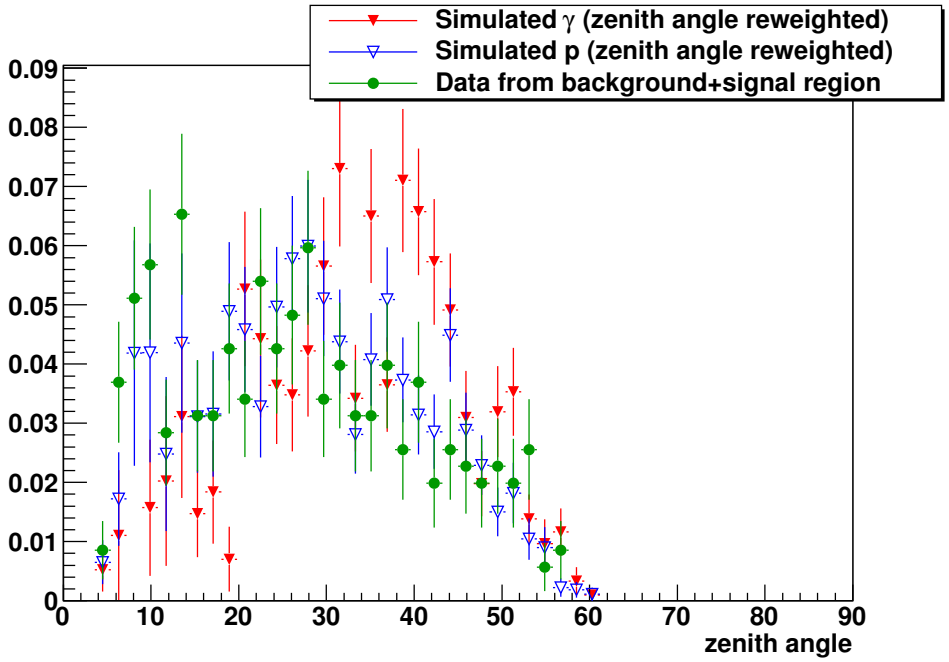

Figure B.2.: Comparison of the data (green ●) from background and signal region with reweighted proton- (blue ▽) and photon-simulations (red ▼). Reconstructed energy between $10^{17.5}$ eV and $10^{17.75}$ eV.

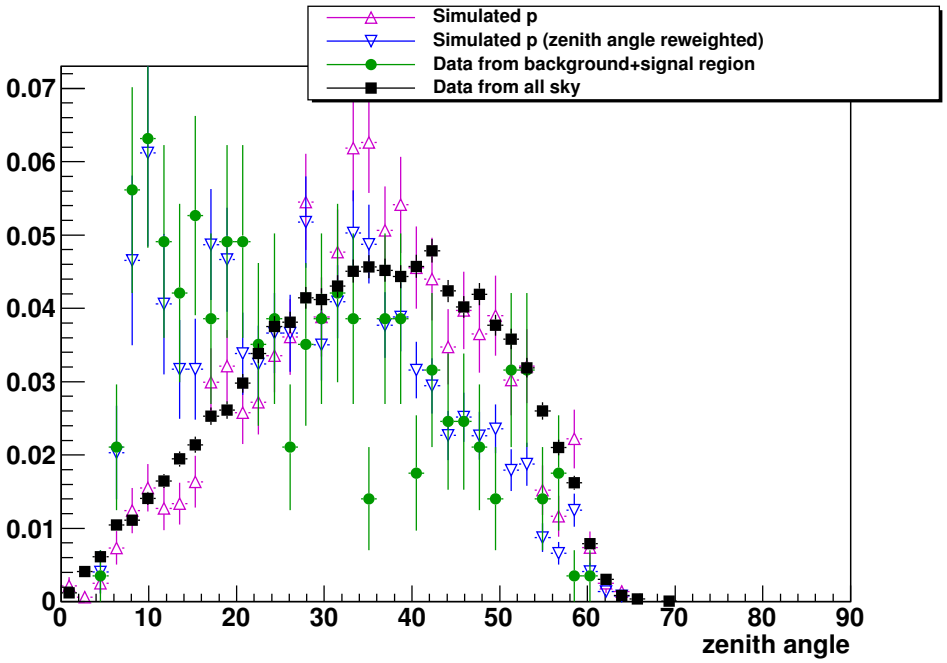

Figure B.3.: Comparison of the the all-sky data (black ■) and data (green ●) from background and signal region with standard CORSIKA proton simulations (purple △) and reweighted proton simulations (blue ▽). Reconstructed energy between $10^{17.75}$ eV and 10^{18} eV.

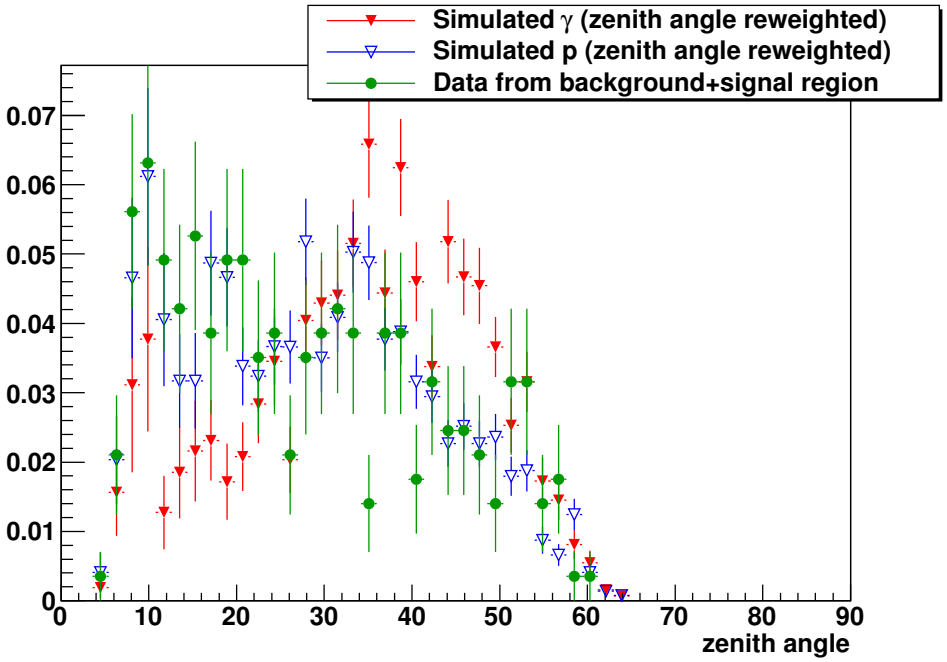

Figure B.4.: Comparison of the data (green ●) from background and signal region with reweighted proton- (blue ▽) and photon-simulations (red ▼). Reconstructed energy between $10^{17.75}$ eV and 10^{18} eV.

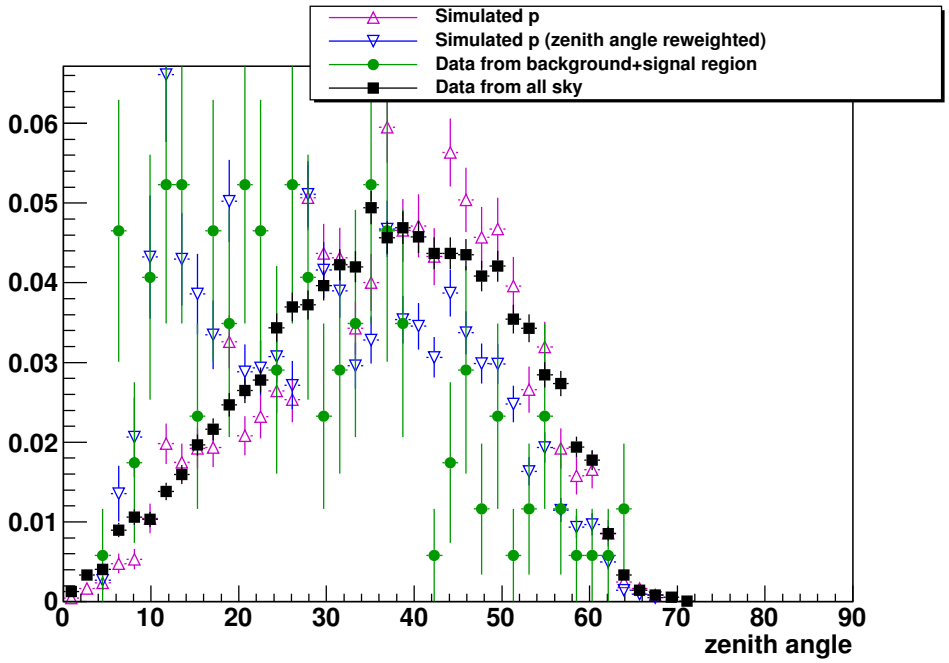

Figure B.5.: Comparison of the the all-sky data (black ■) and data (green ●) from background and signal region with standard CORSIKA proton simulations (purple △) and reweighted proton simulations (blue ▽). Reconstructed energy between 10^{18} eV and $10^{18.25}$ eV.

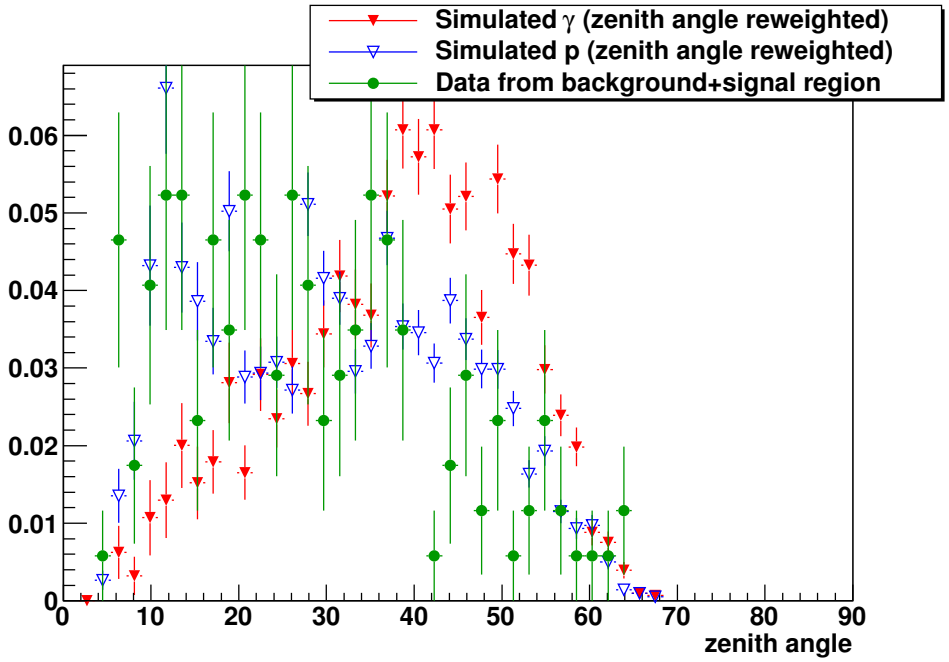

Figure B.6.: Comparison of the data (green ●) from background and signal region with reweighted proton- (blue ▽) and photon-simulations (red ▼). Reconstructed energy between 10^{18} eV and $10^{18.25}$ eV.

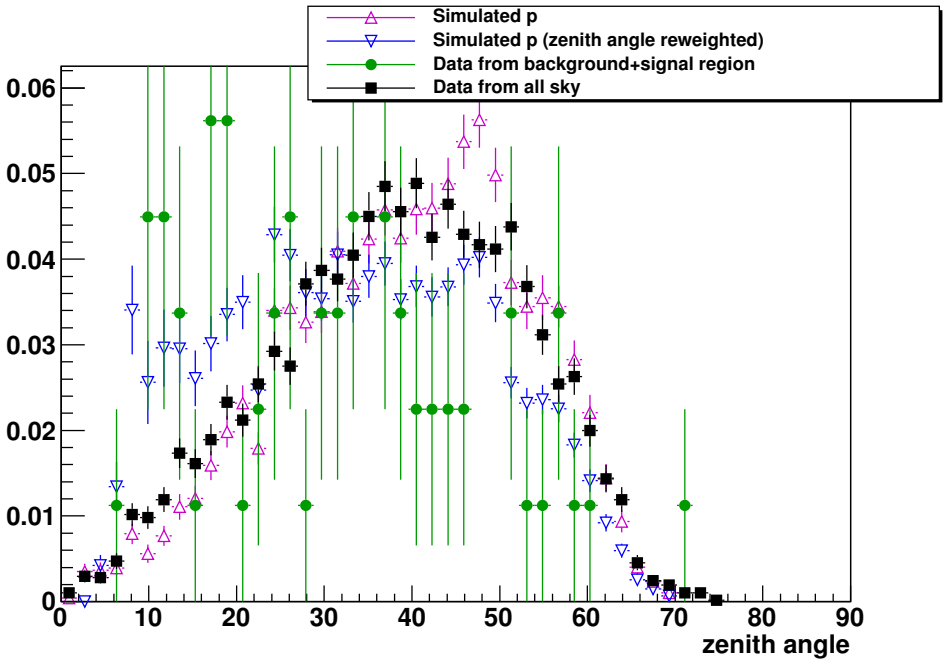

Figure B.7.: Comparison of the the all-sky data (black ■) and data (green ●) from background and signal region with standard CORSIKA proton simulations (purple △) and reweighted proton simulations (blue ▽). Reconstructed energy between $10^{18.25}$ eV and $10^{18.5}$ eV.

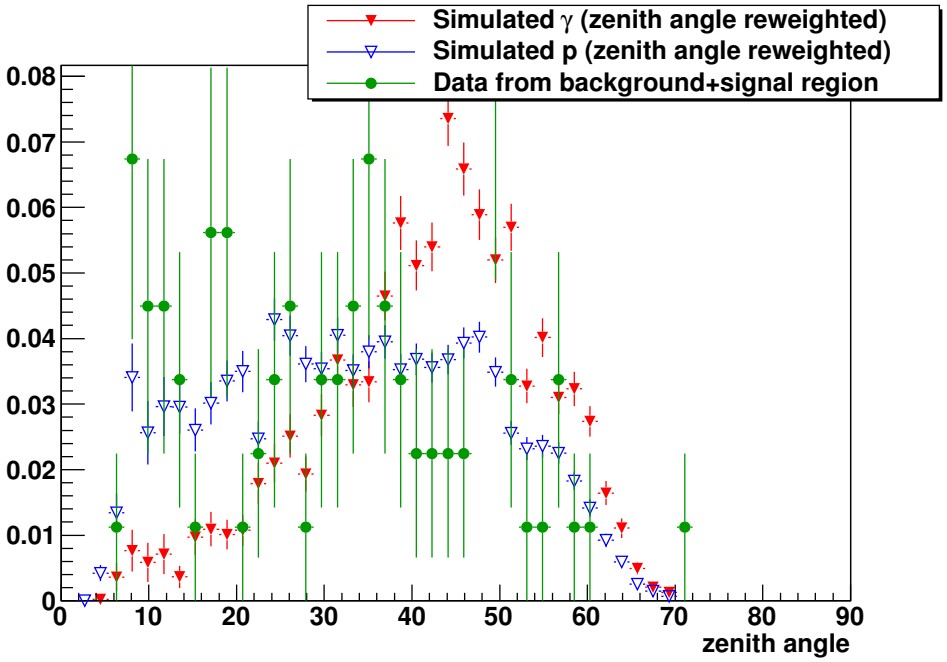

Figure B.8.: Comparison of the data (green ●) from background and signal region with reweighted proton- (blue ▽) and photon-simulations (red ▼). Reconstructed energy between $10^{18.25}$ eV and $10^{18.5}$ eV.

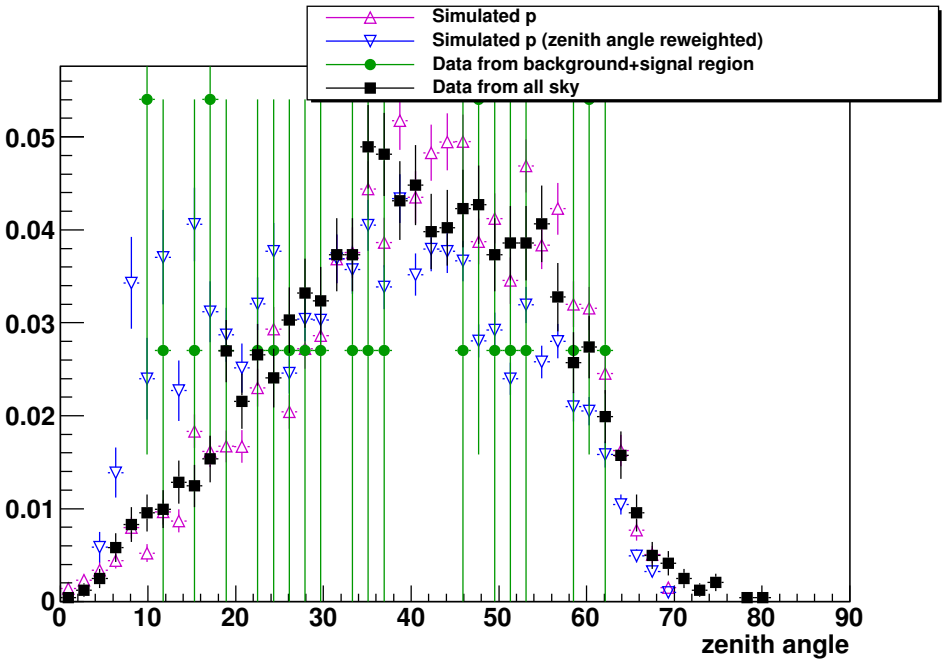

Figure B.9.: Comparison of the the all-sky data (black ■) and data (green ●) from background and signal region with standard CORSIKA proton simulations (purple △) and reweighted proton simulations (blue ▽). Reconstructed energy between $10^{18.5}$ eV and $10^{18.75}$ eV.

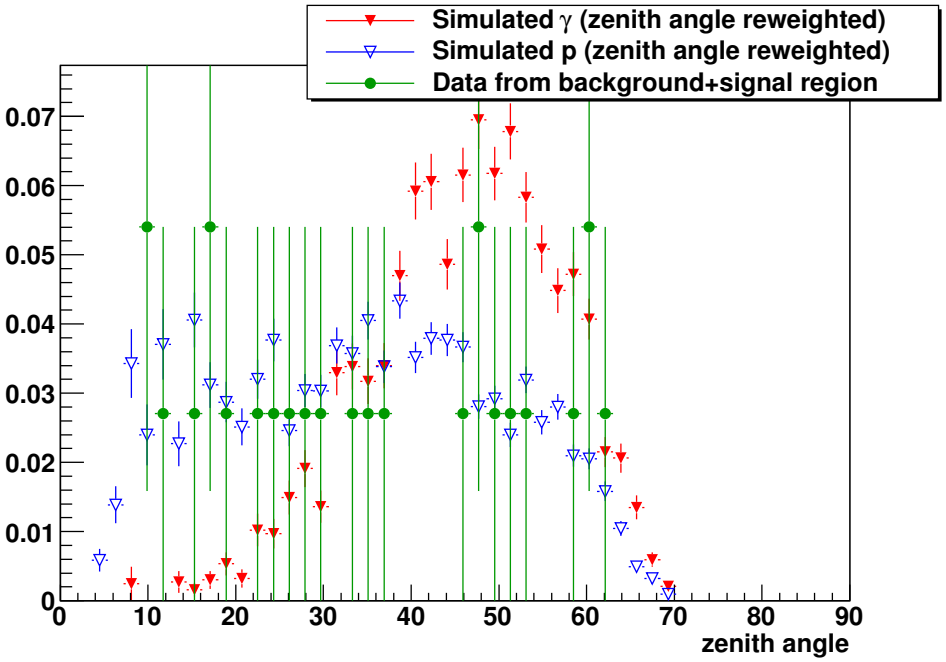

Figure B.10.: Comparison of the data (green ●) from background and signal region with reweighted proton- (blue ▽) and photon-simulations (red ▼). Reconstructed energy between $10^{18.5}$ eV and $10^{18.75}$ eV.

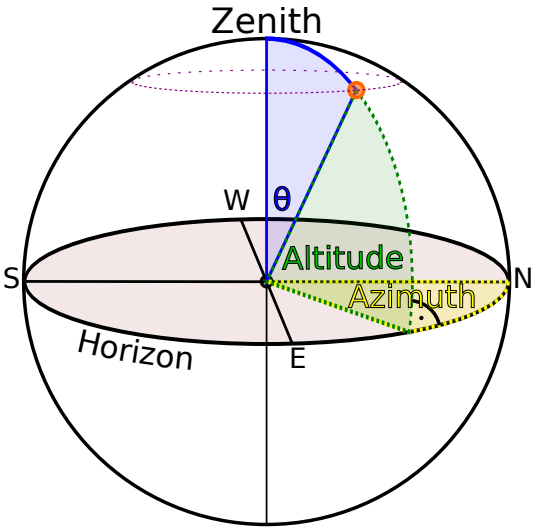

Figure B.11.: Horizon coordinate system. The altitude, azimuth and zenith angle coordinates of the orange point on the sky are shown. The local ground plane of the observer is shown in shaded pink. The pink dotted line shows points of constant altitudes. The curved parts of the dotted green and blue line show points of constant azimuth.

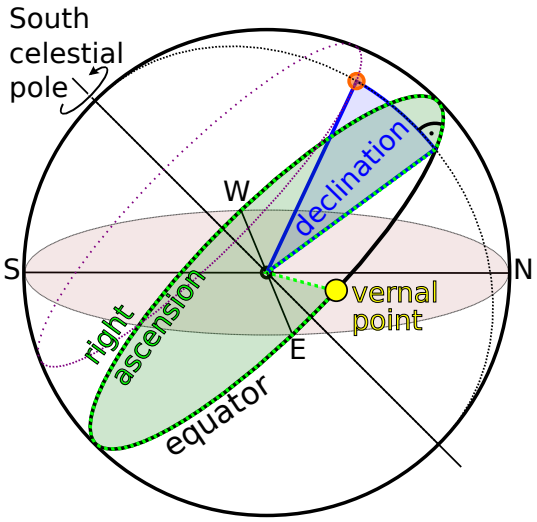

Figure B.12.: Equatorial coordinate system for an observer on the southern hemisphere. The right ascension and declination of the orange point of the sky are shown. In this example the declination is negative. The purple dotted line shows points of constant declination. The vernal point as the zero-point of the right ascension coordinate is shown in yellow.

B.3. Coordinate systems

There are two sets of celestial coordinate systems used for this analysis. The horizon coordinate system (azimuth and altitude or zenith) and the rotating equatorial coordinate system (right ascension and declination).

The horizon coordinate system is shown in figure B.11. A point of the sky is identified by the angular distance to the horizon (altitude) and the angle along the horizon (azimuth). There are different conventions for the direction and zero-point of the azimuth. This does not matter here, because the azimuth is not used for the shown analysis. The altitude, sometimes also called "elevation", can be converted directly to the zenith angle θ by subtracting it from 90°. A single point in the sky (e.g. a star) has different horizon coordinates for different times, because of the rotation of the earth, and for different places on earth.

The rotating equatorial coordinate system is a coordinate system where a single point on the sky has a fixed set of coordinates which are independent of the place on earth and time[1]. The ground plane is no longer defined by the local horizon but by the projection of the Earth's equator onto the sky, which is called the "celestial equator". The coordinate system is shown in figure B.12. The coordinates are the distance to the celestial equator (declination), which corresponds to the altitude in the horizon coordinate system, and the distance along the celestial equator (right ascension), which corresponds to the

[1]Small long-term changes caused by the proper motion of the object and the precession of the earth's axis are neglected here

azimuth in the horizon coordinate system. Positive declinations are on the northern celestial hemisphere, negative declinations are on the southern hemisphere. The right ascension is counted *against the direction* of the apparent rotation of the sky as seen from a fixed place on earth. The zero-point of the right ascension coordinate is the "vernal point" or "vernal equinox point". It is an abstract point, which is defined as one of the two intersections of the celestial equator with the ecliptic. The ecliptic is the plane of the earth's orbit around the sun, or the apparent track on which the sun moves in the course of the year, as seen from earth. The projected course of the sun crosses the equator at the "vernal equinox point" from south to north. The right ascension is often given in hours, minutes and seconds, where one hour corresponds to 15° (360° = 24 h). The minutes and seconds are then parts of hours, not of degrees.

During transformations of the coordinates from the horizon coordinate system to the rotating equatorial system, sometimes also an equatorial system that is fixed relative to earth is used. Here the right ascension is replaced by the "hour angle" which is counted *in direction* of the apparent rotation of the sky. The zero-point of the hour angle is at the intersection point of the south meridian (north meridian on the southern hemisphere) with the celestial equator.